

Inference for Dispersion and Curvature of Random Objects

Wookyeong Song* and Hans-Georg Müller*

*Department of Statistics, University of California, Davis

August 1, 2025

Abstract

There are many open questions pertaining to the statistical analysis of random objects, which are increasingly encountered. A major challenge is the absence of linear operations in such spaces. A basic statistical task is to quantify statistical dispersion or spread. For two measures of dispersion for data objects in geodesic metric spaces, Fréchet variance and metric variance, we derive a central limit theorem (CLT) for their joint distribution. This analysis reveals that the Alexandrov curvature of the geodesic space determines the relationship between these two dispersion measures. This suggests a novel test for inferring the curvature of a space based on the asymptotic distribution of the dispersion measures. We demonstrate how this test can be employed to detect the intrinsic curvature of an unknown underlying space, which emerges as a joint property of the space and the underlying probability measure that generates the random objects. We investigate the asymptotic properties of the test and its finite-sample behavior for various data types, including distributional data and point cloud data. We illustrate the proposed inference for intrinsic curvature of random objects using gait synchronization data represented as symmetric positive definite matrices and energy compositional data on the sphere.

Keywords: Alexandrov curvature; Metric statistics; Fréchet variance; Metric variance; Bures-Wasserstein geometry

1 Introduction

Complex random objects are increasingly prevalent in data analysis and may be viewed as data residing in a metric space. Examples of such object data include probability distributions with the Wasserstein geometry (Chen et al. 2023), covariance matrices with various metrics on the spaces of symmetric positive definite (SPD) matrices (Arsigny et al. 2007, Lin 2019), distributional data with the Fisher-Rao metric on the Hilbert sphere (Dai 2022), data on Riemannian symmetric spaces (Cornea et al. 2017), finite-dimensional Riemannian manifolds (Eltzner et al. 2018), phylogenetic trees (Billera et al. 2001) and functional data (Wang et al. 2016), among other data types (Marron & Dryden 2021, Huckemann & Eltzner 2021).

We consider here data that are situated in a separable geodesic metric space (\mathcal{M}, d) with a distance $d : \mathcal{M} \times \mathcal{M} \rightarrow \mathbb{R}$ and random objects X with a Borel probability measure \mathcal{P} on \mathcal{M} ; any elements in the space can be connected by a unique geodesic, which is a minimal length curve in the space. The absence of algebraic structure in a general metric space \mathcal{M} motivates a framework of metric statistics for the analysis of such data (Dubey et al. 2024, Wang et al. 2024), as well as new methodologies for statistical inference (Song & Chen 2022, Chu & Dai 2024, Jiang et al. 2024, Dubey & Zheng 2023). Specifically, alternative approaches are necessary for defining the expectation and dispersion for random objects $X \in \mathcal{M}$. The Fréchet mean (Fréchet 1948), a generalization of the notion of expected value for random objects, is a natural measure of location,

$$\mu_{\oplus} = \operatorname{argmin}_{\xi \in \mathcal{M}} \mathbb{E} d^2(\xi, X). \quad (1)$$

Note that here and in the following, expectations \mathbb{E} are with respect to the probability

measure \mathcal{P} of X .

An obvious measure of dispersion for random objects is then the Fréchet variance,

$$V_F = \mathbb{E}d^2(\mu_{\oplus}, X). \quad (2)$$

An empirical estimator of V_F was studied in [Dubey & Müller \(2019\)](#), who derived consistency and a central limit theorem (CLT) for this estimator under suitable assumptions, including the existence and uniqueness of the Fréchet mean μ_{\oplus} and entropy conditions; this CLT also led to a test for comparing k populations of metric space-valued data objects.

The metric variance V_M was introduced in [Dubey & Müller \(2020\)](#) as an alternative to quantify the dispersion of random objects,

$$V_M = \frac{1}{2}\mathbb{E}d^2(X, X'), \quad (3)$$

where X' represents an independent and identically distributed (i.i.d.) copy of X . Metric variance is well-defined under weak conditions, as it does not require the uniqueness of a Fréchet mean μ_{\oplus} in (1). In Euclidean spaces, one has $V_F = V_M$, which can be understood through the well-known identity $\frac{1}{n-1} \sum_{i=1}^n (X_i - \bar{X})^2 = \frac{1}{2n(n-1)} \sum_{i,j=1}^n (X_i - X_j)^2$. This identity holds even in infinite-dimensional Hilbert spaces. However, in general metric spaces, $V_F \neq V_M$, and it raises the question of what drives the difference and whether it can be exploited to learn features of the space or underlying probability measure.

Assume that the probability measure \mathcal{P} on the geodesic space (\mathcal{M}, d) that determines the distribution of X is strictly positive, i.e., for any $\delta > 0$ and any $\xi \in \mathcal{M}$, one has $\mathcal{P}(B_{\delta}(\xi)) > 0$, where $B_{\delta}(\xi)$ is an open ball of radius δ centered at ξ with respect to the metric d . Under this condition, we show that the sign of curvature (in the sense of

Alexandrov) of the geodesic space \mathcal{M} can be inferred by comparing the two dispersion measures V_F and V_M . Determining the curvature of the space is important because it has a bearing on the asymptotic properties of estimators, including convergence rates for empirical barycenters (Ahidar-Coutrix et al. 2020, Hundrieser et al. 2024, Pennec 2019).

The study of intrinsic curvature is particularly relevant when the probability measure \mathcal{P} of random objects X is not strictly positive but instead concentrates on a simply-connected subset $\mathcal{A} \subset \mathcal{M}$. This arises because, once the ambient geodesic space (\mathcal{M}, d) is determined, the Alexandrov curvature of (\mathcal{M}, d) can be mathematically derived by comparing geodesic triangles in \mathcal{M} with comparison triangles in the model space, as introduced in Section 3.1, and the underlying probability measure \mathcal{P} has no bearing. However, the intrinsic space \mathcal{A} , equipped with the intrinsic geodesic distance d_I , is derived from samples of random objects X_1, \dots, X_n , and is thus affected by both the space (\mathcal{M}, d) and the measure \mathcal{P} ; a rigorous definition of d_I is provided in Section 4.2. Then the geometric structure, including curvature, of the space where the random objects X actually reside corresponds to the intrinsic space (\mathcal{A}, d_I) that reflects the measure \mathcal{P} rather than the ambient space (\mathcal{M}, d) .

For instance, the space of multivariate distributional data equipped with the 2-Wasserstein distance, denoted as $\mathcal{W}_2(\mathbb{R}^p)$, $p \geq 2$, is known to exhibit positive Alexandrov curvature (Otto 2001). However, the intrinsic curvature of a subspace $\mathcal{D} \subset \mathcal{W}_2(\mathbb{R}^p)$ may exhibit flat geometry. We provide an explicit example for this in Section 5.1, Example 1.

To the best of our knowledge, there is currently no test available to determine the presence or nature of curvature. To arrive at such a test, our starting point is a CLT for the joint distribution of estimators for the metric and Fréchet variance. It turns out that the relationship between these two measures of variance depends on the presence and sign of underlying curvature. We then harness this relationship to obtain inference on

curvature for both the original space \mathcal{M} and also for the intrinsic curvature of a set \mathcal{A} on which the probability measure \mathcal{P} concentrates, i.e., on which the measure is positive with $\mathcal{P}(\mathcal{A}) = 1$. As a consequence of the joint CLT for the two variance measures, we also obtain a confidence region for the true curvature.

Our main contributions in this paper are as follows:

Joint inference for Fréchet variance and metric variance (Section 2). We derive a CLT for the joint distribution of estimates $(\hat{V}_M, \hat{V}_F)^T$ for metric variance V_M and Fréchet variance V_F in Theorem 1 and provide a consistent estimator of the asymptotic variance of the limiting distribution in Proposition 3. This leads to a joint confidence region for these two dispersion measures.

Impact of curvature on measures of dispersion (Section 3). In Theorems 2 and 3, we show that the curvature of a geodesic metric space determines the relationship between the Fréchet variance V_F and metric variance V_M .

Inference for curvature (Section 4.1). We propose a test statistic for detecting curvature of the original space (\mathcal{M}, d) based on the two dispersion measures and develop a consistent test for the null hypothesis that the space is flat, for contiguous alternatives that the curvature of the space is either strictly positive or negative.

Detecting intrinsic curvature (Section 4.2). Intrinsic curvature of a latent space \mathcal{A} on which the underlying probability measure \mathcal{P} concentrates can be inferred from observed samples by combining Dijkstra's algorithm (Dijkstra 1959) and the proposed curvature test. Simulation studies for bivariate distributional data with Wasserstein geometry and 3-dimensional point cloud data are presented in Sections 5.1 and 5.2, followed by data illustrations to detect intrinsic curvature for gait synchronization data and energy compositional data in Section 6 and discussion in Section 7.

2 Inference for dispersion measures of random objects

Consider a separable metric space (\mathcal{M}, d) endowed with a probability measure \mathcal{P} and random objects X , by which we mean random variables that take values in the metric space \mathcal{M} . We observe a sample of random objects X_1, \dots, X_n with the same distribution as X . The sample estimates for the Fréchet mean μ_{\oplus} in (1), which may be a set of minimizers, and for the Fréchet variance V_F in (2) are given by, respectively,

$$\hat{\mu}_{\oplus} = \operatorname{argmin}_{\xi \in \mathcal{M}} \frac{1}{n} \sum_{i=1}^n d^2(\xi, X_i), \quad \hat{V}_F = \frac{1}{n} \sum_{i=1}^n d^2(\hat{\mu}_{\oplus}, X_i). \quad (4)$$

The CLT for Fréchet variance follows from the theory of M-estimators (van der Vaart & Wellner 2023), under the following conditions (Dubey & Müller 2019):

- (F0) The space \mathcal{M} is totally bounded.
- (F1) For all $\epsilon > 0$, $\inf_{d(\xi, \mu_{\oplus}) > \epsilon} \mathbb{E}d^2(\xi, X) > \mathbb{E}d^2(\mu_{\oplus}, X)$.
- (F2) $\delta \int_0^1 [1 + \log N(\delta\epsilon/2, B_\delta(\xi), d)]^{\frac{1}{2}} d\epsilon \rightarrow 0$ as $\delta \rightarrow 0$, for all $\xi \in \mathcal{M}$, where $B_\delta(\xi)$ is an open ball of radius δ with the metric d centered at ξ , and $N(\zeta, \mathcal{S}, d)$ denotes the smallest cardinality among all ζ -covers for the set \mathcal{S} with the metric d .

Condition (F0) is needed for weak convergence and (F1) corresponds to the uniqueness of the population Fréchet mean μ_{\oplus} , which implies the consistency of any sample Fréchet mean $\hat{\mu}_{\oplus}$. Condition (F2) is an entropy condition that limits the complexity of the space (\mathcal{M}, d) . The sample estimate for the metric variance V_M in (3) is

$$\hat{V}_M = \frac{1}{n(n-1)} \sum_{1 \leq i < j \leq n} d^2(X_i, X_j). \quad (5)$$

To derive the CLT for metric variance, we require the following conditions.

(M0) $0 < \mathbb{E}d^2(X, X') < \infty$, for i.i.d. random objects $X, X' \in \mathcal{M}$.

(M1) $\mathbb{E}d^4(X, X') < \infty$, for i.i.d. random objects $X, X' \in \mathcal{M}$.

(M2) $\text{Var}_X [\mathbb{E}_{X'|X} \{d^2(X, X') | X\}] > 0$.

Here (M0) is needed for the metric variance to be well-defined, while (M1) is a weak requirement to bound the central moment of the metric variance estimates \hat{V}_M and (M2) ensures that the metric variance estimate \hat{V}_M is meaningful.

The metric variance estimate \hat{V}_M takes the form of a U-statistics, making it possible to leverage martingale properties (Hoeffding 1961, Berk 1966). While U-statistics are traditionally discussed in the context of Euclidean spaces (Serfling 2009, Lee 2019), the underlying concept can be extended to more general metric spaces \mathcal{M} (Alberink & Benktus 2001). The following Proposition is a consequence of these martingale properties. All proofs are in the Supplement.

Proposition 1. *Under (M0), $\hat{V}_M \rightarrow V_M$ almost surely. Furthermore, assume that conditions (M0) and (M1) hold. Then, $\mathbb{E}\|\hat{V}_M - V_M\|^2 = O(n^{-1})$.*

Considering the joint distribution of estimates of metric variance and Fréchet variance, their theoretical foundations differ substantially. While in the CLT for Fréchet variance Dubey & Müller (2019) primarily draw upon M-estimation theory, the uniqueness of the Fréchet mean μ_{\oplus} (F1) and the entropy condition (F2), the CLT for metric variance does not require either of these assumptions. Instead, one can more directly utilize properties of U-statistics (Hoeffding 1948) and (M0)-(M2). Note that total boundedness (F0) implies the moment condition (M1). We now present the following joint central limit theorem.

Theorem 1. *Under (F0), (F1), (F2), (M0) and (M2),*

$$\sqrt{n} \left((\hat{V}_M, \hat{V}_F)^T - (V_M, V_F)^T \right) \rightarrow N(\mathbf{0}, \Sigma) \quad \text{in distribution,}$$

where $\Sigma = \begin{pmatrix} \sigma_M^2 & \sigma_{FM} \\ \sigma_{FM} & \sigma_F^2 \end{pmatrix}$, $\sigma_M^2 = \text{var}_X [\mathbb{E}_{X'|X} \{d^2(X, X')|X\}]$, $\sigma_F^2 = \text{var}(d^2(\mu_{\oplus}, X))$, and $\sigma_{FM} = \text{cov}(\mathbb{E}_{X'|X} \{d^2(X, X')|X\}, d^2(\mu_{\oplus}, X))$.

The convergence rate towards the limiting distribution for the metric variance estimates \hat{V}_M is based on the Berry-Essen theorem for U-statistics (Alberink & Bentkus 2001), an extension of previous bounds of Callaert & Janssen (1978), van Zwet (1984), Friedrich (1989). The following additional finite moment assumption is needed.

(M3) $\mathbb{E}_X |\mathbb{E}_{X|X'} \{d^2(X, X')|X\}|^3 < \infty$, for i.i.d. random objects $X, X' \in \mathcal{M}$.

For a bounded metric space \mathcal{M} , $\mathbb{E}_X |\mathbb{E}_{X'|X} \{d^2(X, X')|X\}|^p$ is finite for all $p > 0$, so that (M3) automatically holds.

Proposition 2. Under (M0)-(M3), $\sup_x \left| \mathbb{P} \left(\sqrt{n}(\hat{V}_M - V_M)/\sigma_M \leq x \right) - \Phi(x) \right| = O(n^{-\frac{1}{2}})$

for $n \geq 2$, where $\Phi(x)$ is the distribution function of the standard normal distribution.

The proof relies on an application of the Essen lemma for the characteristic function of metric variance and involves decomposing \hat{V}_M into a projection and a residual part. The projection component is addressed similarly as in the standard proof for the Berry-Esseen theorem for i.i.d. summands, while the residual component is handled by utilizing a martingale structure. Simultaneous inference for two dispersion measures can be obtained from the asymptotic normality established in Theorem 1 by supplementing sample-based estimators for the asymptotic covariance matrix

$$\hat{\Sigma} = \begin{pmatrix} \hat{\sigma}_M^2 & \hat{\sigma}_{FM} \\ \hat{\sigma}_{FM} & \hat{\sigma}_F^2 \end{pmatrix}, \quad (6)$$

given by $\hat{\sigma}_M^2 = \frac{1}{n} \sum_{i=1}^n \left\{ \frac{1}{n-1} \sum_{j \neq i}^n d^2(X_i, X_j) \right\}^2 - \left\{ \frac{2}{n(n-1)} \sum_{1 \leq i < j \leq n} d^2(X_i, X_j) \right\}^2$,

$$\hat{\sigma}_{FM} = \frac{1}{n} \sum_{i=1}^n \frac{d^2(\hat{\mu}_\oplus, X_i)}{n-1} \left\{ \sum_{j \neq i}^n d^2(X_i, X_j) \right\} - \left\{ \frac{1}{n} \sum_{i=1}^n d^2(\hat{\mu}_\oplus, X_i) \right\} \left\{ \frac{2}{n(n-1)} \sum_{1 \leq i < j \leq n} d^2(X_i, X_j) \right\},$$

$$\text{and } \hat{\sigma}_F^2 = \frac{1}{n} \sum_{i=1}^n d^4(\hat{\mu}_\oplus, X_i) - \left\{ \frac{1}{n} \sum_{i=1}^n d^2(\hat{\mu}_\oplus, X_i) \right\}^2.$$

The following Proposition establishes the consistency of these estimates.

Proposition 3. *Assume that the conditions of Theorem 1 hold. Then*

$$\hat{\sigma}_{FM}^2 \rightarrow \sigma_{FM}^2, \hat{\sigma}_M^2 \rightarrow \sigma_M^2, \hat{\sigma}_F^2 \rightarrow \sigma_F^2 \text{ in probability.}$$

Setting $\hat{\eta} = (\hat{V}_M, \hat{V}_F)^T$, $\eta = (V_M, V_F)^T$, these results enable the construction of an asymptotic joint $100(1 - \alpha)\%$ confidence region for η given by

$$\mathcal{C}_n(1 - \alpha) := \left\{ \eta \in \mathbb{R}^2 \mid (\hat{\eta} - \eta)^T (\hat{\Sigma}/n)^{-1} (\hat{\eta} - \eta) \leq \chi_2^2(1 - \alpha) \right\}, \quad (7)$$

where $\chi_q^2(1 - \alpha)$ is the $(1 - \alpha)$ quantile of the chi-square distribution with q d.f.

3 Alexandrov curvature and dispersion measures V_M and V_F

3.1 Metric geometry

Consider random objects X taking values in the Hilbert space \mathcal{H} . In this case, the Fréchet mean μ_\oplus of X is equivalent to the expectation $\mathbb{E}X$. Using the inner product of the Hilbert space, it can be readily shown that the Fréchet variance V_F and metric variance V_M are identical, $V_F = V_M$; this identity does not hold in general metric spaces (Dubey & Müller 2020). We provide a brief overview of basic metric geometry. Further details can be found in Burago et al. (2001), Lang (2012), Lin & Müller (2021). For a metric space (\mathcal{M}, d) , a path $\gamma : [0, T] \rightarrow \mathcal{M}$ is a geodesic from $X \in \mathcal{M}$ to $Y \in \mathcal{M}$ if $\gamma(0) = X$, $\gamma(T) = Y$ and $d(\gamma(t), \gamma(t')) = |t - t'|$ for all $t, t' \in [0, T]$. The metric space (\mathcal{M}, d) is a geodesic space if any pair of points $X, Y \in \mathcal{M}$ can be connected by a geodesic. The metric space (\mathcal{M}, d) is a

unique geodesic space if geodesics are unique. Euclidean space is a unique geodesic space and geodesics are straight lines connecting any two points.

In contrast to Euclidean spaces, general metric spaces can exhibit *curvature*, which measures deviation from flatness. For a geodesic space \mathcal{M} , curvature is assessed by comparison triangles situated in model metric spaces $(\mathcal{M}_\kappa, d_\kappa)$, where κ is a curvature parameter.

For $\kappa > 0$, the model space is the sphere $\mathbb{S}^2 = \{(x, y, z) \mid x^2 + y^2 + z^2 = 1\}$ with the angular distance $d_\kappa(a, b) = \arccos(x_a x_b + y_a y_b + z_a z_b)/\sqrt{\kappa}$, where $a = (x_a, y_a, z_a)$ and $b = (x_b, y_b, z_b)$. For $\kappa < 0$, the model space is the hyperbolic space $\mathbb{H}^2 = \{(x, y, z) \mid x^2 + y^2 - z^2 = -1\}$ with the hyperbolic distance $d_\kappa(a, b) = \text{arccosh}(z_a z_b - x_a x_b - y_a y_b)/\sqrt{-\kappa}$. Finally, for $\kappa = 0$, the model space is the Euclidean plane \mathbb{R}^2 with the Euclidean distance. A *geodesic triangle* for vertices a, b, c on the space \mathcal{M} , denoted by $\triangle(a, b, c)$, consists of three geodesic edges γ_{ab}, γ_{bc} , and γ_{ca} , connecting the corresponding vertices. A *comparison triangle* $\tilde{\triangle}(\tilde{a}, \tilde{b}, \tilde{c})$ on the model space $(\mathcal{M}_\kappa, d_\kappa)$ is formed by reference vertices $\tilde{a}, \tilde{b}, \tilde{c}$ and geodesic edges $\tilde{\gamma}_{\tilde{a}\tilde{b}}, \tilde{\gamma}_{\tilde{b}\tilde{c}}$ and $\tilde{\gamma}_{\tilde{c}\tilde{a}}$ that have lengths identical to the lengths of γ_{ab}, γ_{bc} and γ_{ca} .

The formal definition of curvature involves comparing the comparison triangle $\tilde{\triangle}(\tilde{a}, \tilde{b}, \tilde{c})$ with the geodesic triangle $\triangle(a, b, c)$ of perimeter $< 2D_\kappa$, where $D_\kappa = \infty$ for $\kappa \leq 0$, and $D_\kappa = \frac{\pi}{\sqrt{\kappa}}$ for $\kappa > 0$. For any point x on segment γ_{bc} of $\triangle(a, b, c)$, a corresponding point \tilde{x} exists on segment $\tilde{\gamma}_{\tilde{b}\tilde{c}}$ of $\tilde{\triangle}(\tilde{a}, \tilde{b}, \tilde{c})$ such that $d(x, b) = d_\kappa(\tilde{x}, \tilde{b})$. If $d(x, a) \leq d_\kappa(\tilde{x}, \tilde{a})$ (or $d(x, a) \geq d_\kappa(\tilde{x}, \tilde{a})$, respectively) for all such x , as well as for x on γ_{ab} or γ_{ac} , then (\mathcal{M}, d) has curvature $\leq \kappa$ (or $\geq \kappa$, respectively). Figure 1 illustrates the shapes of comparison triangles $\tilde{\triangle}$ on model spaces $(\mathcal{M}_\kappa, d_\kappa)$, with $\kappa > 0$, $\kappa = 0$, and $\kappa < 0$.

3.2 Relationship between V_M and V_F reflects underlying curvature

Let X be random objects situated on a complete geodesic space (\mathcal{M}, d) , where the underlying probability measure \mathcal{P} satisfies the following assumption:

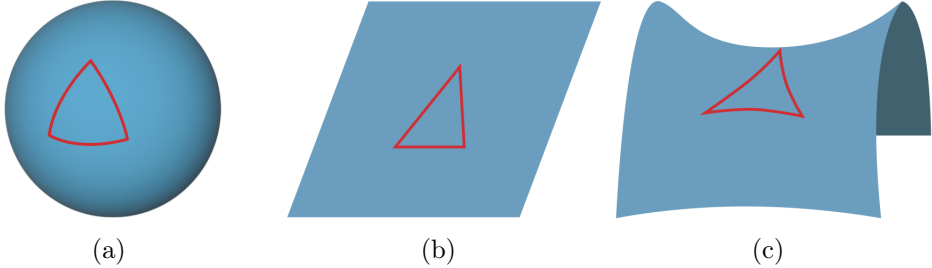


Figure 1: Model spaces \mathcal{M}_κ , with their comparison triangles $\tilde{\Delta}$. (a) Positive curvature parameter, $\kappa > 0$, (b) Flat, $\kappa = 0$, and (c) Negative, $\kappa < 0$.

(S1) For all $\delta > 0$ and $\xi \in \mathcal{M}$, $\mathcal{P}(X \in B_\delta(\xi)) > 0$, where $B_\delta(\xi)$ is an open ball of radius δ with the metric d centered at ξ .

Condition (S1) corresponds to the notion of a strictly positive measure (Kelley 1959) and is needed to prevent probability measures \mathcal{P} from being concentrated on any strict closed subspace $\mathcal{D} \subset \mathcal{M}$, as the curvature of \mathcal{D} might differ from that of the original space \mathcal{M} . A complete geodesic space (\mathcal{M}, d) featuring non-positive curvature is a *Hadamard space*, or complete CAT(0) space. Geodesic triangles in a Hadamard space are thinner or equal to triangles in a Euclidean space. For random objects X in Hadamard spaces, the function $F(\cdot) = \mathbb{E}d^2(\cdot, X)$ is strongly convex, ensuring a unique Fréchet mean μ_\oplus if $F(\xi) < \infty$ for some ξ (Sturm 2003). Examples of Hadamard spaces include flat spaces that are complete, such as Hilbert space, the space of univariate probability distributions $\mathcal{W}_2(\mathbb{R})$ with the 2-Wasserstein metric (Kantorovich 2006), or SPD matrices with the Frobenius, power and log-Frobenius, Cholesky and log Cholesky metrics (Dryden, Bai, Brignell & Shen 2009, Feragen et al. 2015, Pigoli et al. 2014, Lin 2019). Non-flat Hadamard spaces include the space of SPD matrices with the affine-invariant Riemannian metric (Bhatia 2009) and the phylogenetic tree space with the BHV metric (Billera et al. 2001).

Applying the law of cosines and properties of directional derivatives in Hadamard spaces, including Theorem 4.5.6 in Burago et al. (2001), we find that the following relationship

holds between V_M and V_F .

Theorem 2. *Suppose (\mathcal{M}, d) is a Hadamard space and random objects X on \mathcal{M} satisfy $\mathbb{E}d^2(\xi, X) < \infty$ for some $\xi \in \mathcal{M}$. Then $V_M \geq V_F$. Furthermore, if (\mathcal{M}, d) has strictly negative curvature and condition (S1) holds, then $V_M > V_F$.*

Next, we establish the relationship for the case of complete geodesic spaces (\mathcal{M}, d) with positive curvature. Examples include the space of SPD matrices with the Bures-Wasserstein metric (Dryden, Koloydenko & Zhou 2009, Han et al. 2021), finite-dimensional spheres \mathbb{S}^p , the Hilbert sphere \mathbb{S}^∞ with geodesic metric (Dai 2022) and the 2-Wasserstein space for distributions with Euclidean $\mathcal{W}_2(\mathbb{R}^p)$, $p \geq 2$ (Otto 2001).

Theorem 3. *Suppose (\mathcal{M}, d) is a complete unique geodesic space with non-negative curvature and condition (F1) (uniqueness of the Fréchet mean) holds. Then $V_M \leq V_F$. Furthermore, if (\mathcal{M}, d) has strictly positive curvature and condition (S1) holds, then $V_M < V_F$.*

In spaces with positive curvature, the assumption of a unique Fréchet mean μ_\oplus in Theorem 3 is not guaranteed to be satisfied. An example is a probability measure uniformly distributed over an entire sphere \mathbb{S}^p . Then every point on the sphere is a minimizer of the Fréchet function. However, random objects X on the sphere may still have a unique Fréchet mean under certain conditions. For example, if the support of a subset $\mathcal{M} \subset \mathbb{S}^p$ is contained within a geodesic ball $B_r(\xi)$ centered at some $\xi \in \mathbb{S}^p$ with radius $r < \frac{\pi}{2}$, then random objects X on \mathcal{M} have a unique Fréchet mean (Afsari 2011). Moreover, Dai (2022) demonstrated that a subset of the Hilbert sphere $\mathcal{M} \subset \mathbb{S}^\infty$ with $\sup_{x,y \in \mathcal{M}} d(x, y) \leq \frac{\pi}{2}$ satisfies this assumption. For random objects X in 2-Wasserstein space $\mathcal{W}_2(\mathbb{R}^p)$ with $p \geq 2$, which has a positive curvature, the uniqueness assumption is satisfied when X is absolutely continuous (Aguech & Carlier 2011). For a broader perspective, Ahidar-Coutrix et al. (2020) studied variance inequalities that guarantee the uniqueness of a population Fréchet mean.

Combining Theorems 2 and 3, we obtain the following result.

Corollary 1. *Suppose that the geodesic spaces (\mathcal{M}, d) is flat and complete, random objects X on \mathcal{M} satisfy $\mathbb{E}d^2(\xi, X) < \infty$ for some $\xi \in \mathcal{M}$, and condition (S1) holds. Then $V_M = V_F$.*

4 Inference for curvature

4.1 A test for metric curvature

Suppose that (\mathcal{M}, d) is complete and a totally bounded geodesic space. Consider population Fréchet variance V_F in (2) and metric variance V_M in (3). We define the *metric curvature* ρ of the space \mathcal{M} as

$$\rho = \frac{V_F}{V_M} - 1. \quad (8)$$

In the following we show that $\rho < 0$ when (\mathcal{M}, d) exhibits strictly negative curvature, as outlined in Theorem 2. Similarly, $\rho > 0$ when (\mathcal{M}, d) has strictly positive curvature (Theorem 3) and $\rho = 0$ when (\mathcal{M}, d) is a flat space (Corollary 1).

Proposition 4. *Under condition (S1), if (\mathcal{M}, d) has strictly negative curvature, then $\rho < 0$. If (\mathcal{M}, d) has strictly positive curvature and condition (F1) holds, then $\rho > 0$. Furthermore, if (\mathcal{M}, d) is a flat space, then $\rho = 0$.*

Consider random samples X_1, \dots, X_n with the same distribution as X , and the sample Fréchet variance \hat{V}_F in (4) and metric variance \hat{V}_M in (5). The sample estimator for ρ in (8) is given by

$$\hat{\rho} = \frac{\hat{V}_F}{\hat{V}_M} - 1. \quad (9)$$

Theorem 1 coupled with the continuous mapping theorem yields the asymptotic variance of $\hat{\rho}$, where $\sigma^2 = a^T \Sigma a$, with $a = \left(-\frac{V_F}{V_M^2}, \frac{1}{V_M}\right)^T$, and $\Sigma = \begin{pmatrix} \sigma_M^2 & \sigma_{FM} \\ \sigma_{FM} & \sigma_F^2 \end{pmatrix}$. Proposition 3

provides a consistent estimate of the asymptotic variance σ^2 , given by

$$\hat{\sigma}^2 = \hat{a}^T \hat{\Sigma} \hat{a}, \quad (10)$$

with $\hat{a} = \left(-\frac{\hat{V}_F}{\hat{V}_M^2}, \frac{1}{\hat{V}_M} \right)^T$, where the covariance matrix estimate $\hat{\Sigma}$ is as in (6).

The Fréchet variance estimate \hat{V}_F relies on the computation of the sample Fréchet mean $\hat{\mu}_\oplus$, which often requires case-specific approaches depending on the underlying metric space. For Hadamard space, $\hat{\mu}_\oplus$ can be computed using the proximal point algorithm (Bacák 2014). For Riemannian manifolds with positive curvature, such as the sphere \mathbb{S}^p , gradient-based optimization methods (Fletcher et al. 2004) can be employed. For multivariate distributions under the 2-Wasserstein metric $\mathcal{W}_2(\mathbb{R}^p)$, particularly when the space does not belong to the location-scatter family, $\hat{\mu}_\oplus$ can be estimated using the Sinkhorn approximation (Cuturi 2013) or gradient descent algorithm (Chewi et al. 2020).

Formally, consider the null hypothesis $H_0 : \mathcal{P} \in \Theta_0$ and the alternative hypothesis $H_1 : \mathcal{P} \in \Theta_1$. To determine whether the space \mathcal{M} is curved or not, we can formulate a two-sided test for $\Theta_0 = \{\rho \mid \rho = 0\}$ and $\Theta_1 = \{\rho \mid \rho \neq 0\}$.

The proposed test statistic T_n is then

$$T_n = \frac{\sqrt{n} \hat{\rho}}{\hat{\sigma}}. \quad (11)$$

Under the null hypothesis that \mathcal{M} is a flat space, Propositions 3 and 4 lead to the following key property of the test statistic.

Theorem 4. *Under (F0), (F1), (F2), (M0), (M2) and (S1), for the curvature ρ in (8), then $\sqrt{n}(\hat{\rho} - \rho)/\hat{\sigma} \rightarrow N(0, 1)$ in distribution. Thus, under $H_0 : \rho = 0$, $T_n \rightarrow N(0, 1)$ in distribution.*

For any level $\alpha \in (0, 1)$, define a test function with size α as $\Phi(X_1, \dots, X_n) = \mathbf{I}(R_{n,\alpha})$, where $\mathbf{I}(\cdot)$ is an indicator function and $R_{n,\alpha}$ is a rejection region. For a level α two-sided test, the rejection region is $R_{n,\alpha} = \{|T_n| > z_{\alpha/2}\}$, where z_η is the $(1 - \eta)^{th}$ quantile of the standard normal distribution. The $100(1 - \alpha)\%$ confidence interval for ρ is given by

$$\mathcal{I}_n(1 - \alpha) := \left\{ \rho \in \mathbb{R} \mid \hat{\rho} - z_{\alpha/2} \frac{\hat{\sigma}}{\sqrt{n}} \leq \rho \leq \hat{\rho} + z_{\alpha/2} \frac{\hat{\sigma}}{\sqrt{n}} \right\}. \quad (12)$$

For one-sided tests, where the alternative hypothesis is either $\Theta_1 = \{\rho \mid \rho > 0\}$ (positive curvature) or $\Theta_1 = \{\rho \mid \rho < 0\}$ (negative curvature), the corresponding rejection regions are $R_{n,\alpha} = \{T_n > z_\alpha\}$, or $R_{n,\alpha} = \{T_n < -z_\alpha\}$, respectively. Confidence regions $\mathcal{C}_n(1 - \alpha)$ for $\eta = (V_M, V_F)^T$ in (7) can equally be utilized to infer curvature. For a level α test, the rejection region is $R_{n,\alpha} = \{\eta \mid (\hat{\eta} - \eta)^T (\hat{\Sigma}/n)^{-1} (\hat{\eta} - \eta) > \chi_2^2(1 - \alpha)\}$.

To evaluate the power of the proposed test, we consider alternative hypotheses defined as $H_{1,\delta} : \rho = \rho_n$, where $\rho_n \rightarrow 0$ and $\sqrt{n}\rho_n \rightarrow \infty$ as $n \rightarrow \infty$. Here, ρ_n is the metric curvature parameter at sample size n . These alternatives $\{H_{1,\delta}\}$ are contiguous, shrinking toward H_0 as $n \rightarrow \infty$. The asymptotic normality of $\hat{\rho}$ in Theorem 4 implies that the asymptotic power of the level α test under $H_{1,\delta}$ is

$$\beta_{1,\delta} = \mathbb{P}(R_{n,\alpha}) = \mathbb{P}(|T_n| > z_{\alpha/2}) \rightarrow 1 \quad \text{as } n \rightarrow \infty,$$

demonstrating the consistency of the test.

4.2 Detecting intrinsic curvature

A practical problem of interest is to infer intrinsic curvature from data $X_1, \dots, X_n \in \mathcal{A} \subset \mathcal{M}$, where the underlying probability measure \mathcal{P} is not strictly positive on \mathcal{M} but is instead

concentrated on a simply-connected strict subset \mathcal{A} , on which it is strictly positive with $\mathcal{P}(\mathcal{A}) = 1$. Then a part of \mathcal{M} is devoid of positive probability and the subset \mathcal{A} may exhibit intrinsic curvature that differs from the overall curvature of the ambient space \mathcal{M} .

This motivates extending the proposed metric curvature test from Section 4.1 by incorporating the intrinsic geodesic distance $d_I(X, Y)$ defined on \mathcal{A} . Consider the set $\Gamma_{\mathcal{A}}$ of paths $\gamma : [0, T] \rightarrow \mathcal{A}$ that are entirely contained within the simply connected intrinsic space \mathcal{A} , i.e., $\gamma(t) \in \mathcal{A}$ for all $t \in [0, T]$. The intrinsic distance is defined as $d_I(X, Y) = \inf_{\gamma \in \Gamma_{\mathcal{A}}} \{l(\gamma) \mid \gamma(0) = X, \gamma(T) = Y\}$, where $l(\gamma) := \sup_{0=t_0 < t_1 < \dots < t_n = T, n \in \mathbb{N}} \sum_{i=1}^n d(\gamma(t_{i-1}), \gamma(t_i))$. A consequence of the constraint on paths routing through \mathcal{A} is that for all $x, y \in \mathcal{A}$, one has $d_I(x, y) \geq d(x, y)$, where $d_I(x, y)$ is the length of the shortest path on \mathcal{A} connecting the two points $x, y \in \mathcal{A}$.

Denote by $\mu_{I,\oplus}$, $V_{I,F}$, $V_{I,M}$, and ρ_I the intrinsic Fréchet mean, Fréchet variance, metric variance and curvature, respectively, obtained by replacing the ambient distance d in μ_{\oplus} , V_F , V_M , and ρ in (1), (2), (3) and (8) with the intrinsic distance d_I . For a random sample $\mathcal{X}_n := \{X_1, \dots, X_n\}$, we define the intrinsic sample Fréchet mean as $\hat{\mu}_{I,\oplus} = \operatorname{argmin}_{\xi \in \mathcal{X}_n} \frac{1}{n} \sum_{i=1}^n d_I^2(\xi, X_i)$. Similarly, we define the corresponding estimators $\hat{V}_{I,F}$, $\hat{V}_{I,M}$, $\hat{\rho}_I$ and $\hat{\sigma}_I$ by replacing the ambient distance d with the intrinsic distance d_I . To infer whether the intrinsic space \mathcal{A} is curved or not, we consider the test statistic

$$T_{I,n} = \frac{\sqrt{n} \hat{\rho}_I}{\hat{\sigma}_I}, \quad (13)$$

in analogy to (11) in Section 4.1.

To study the large sample behavior of the test statistic $T_{I,n}$ in (13), we require the following assumptions:

(A0) The measure \mathcal{P} of X is strictly positive on \mathcal{A} and $\mathcal{P}(\mathcal{A}) = 1$.

- (A1) The space (\mathcal{A}, d_I) is totally bounded.
- (A2) For all $\epsilon > 0$, $\inf_{d_I(\xi, \mu_{I,\oplus}) > \epsilon} \mathbb{E}d_I^2(\xi, X) > \mathbb{E}d_I^2(\mu_{I,\oplus}, X)$.
- (A3) For all $\xi \in \mathcal{A}$, $\delta \int_0^1 [1 + \log N(\delta\epsilon/2, B_\delta(\xi), d_I)]^{\frac{1}{2}} d\epsilon \rightarrow 0$ as $\delta \rightarrow 0$.
- (A4) $\mathbb{E}|d_I^2(X, X')| > 0$ and $\text{Var}_X [\mathbb{E}_{X'|X} \{d_I^2(X, X')|X\}] > 0$ for i.i.d. random objects $X, X' \in \mathcal{A}$.

Condition (A0) is commonly employed in manifold learning algorithms such as Laplacian eigenmaps (Belkin & Niyogi 2001) and UMAP (McInnes et al. 2018). Under (A0), the measure is concentrated on \mathcal{A} . Conditions (A1)-(A3) impose boundedness, uniqueness of the intrinsic Fréchet mean and an entropy condition for the intrinsic space \mathcal{A} , which are necessary for the application of empirical process theory. Condition (A4) is required to ensure the existence of ρ_I and prevent degeneration of the asymptotic distribution.

Theorem 5. *Suppose conditions (A0)-(A4) hold. Then, $\sqrt{n}(\hat{\rho}_I - \rho_I)/\hat{\sigma}_I \rightarrow N(0, 1)$ in distribution. Thus, under $H_0 : \rho_I = 0$, $T_{I,n} \rightarrow N(0, 1)$ in distribution.*

The intrinsic distance d_I needs to be estimated because in practice the subspace $\mathcal{A} \subset \mathcal{M}$ is usually unknown. One common approach to estimate the intrinsic distance between any two observations $X_i, X_j \in \mathcal{X}_n$ involves constructing a weighted graph based on nearest neighbors and computing the shortest paths using Dijkstra's algorithm (Dijkstra 1959), as detailed in Algorithm 1. For a discussion of the convergence of Dijkstra's algorithm we refer to Section S.3 of the Supplement.

Algorithm 1 Intrinsic distance estimation

Input: Observations \mathcal{X}_n , ambient distance d and neighbor ball size parameter r .

Output: Pairwise intrinsic distance estimate $d_I(X_i, X_j)$, for all $X_i, X_j \in \mathcal{X}_n$.

1. Construct a weighted graph for each pair $(X_i, X_j) \in \mathcal{X}_n$, connecting if $d(X_i, X_j) \leq r$.
2. Set $d_I(X_i, X_j)$ to be the length of the shortest path calculated by Dijkstra's algorithm (Dijkstra 1959).

Following the same argument as in Section 4.1, for a two-sided test at level α , the $(1-\alpha)$

confidence intervals for the intrinsic curvature ρ_I and for the intrinsic dispersion measures $\eta_I = (V_{I,M}, V_{I,F})^T$ are given by:

$$\mathcal{I}_{I,n}(1 - \alpha) = \left\{ \rho_I \in \mathbb{R} \mid \hat{\rho}_I - z_{\alpha/2} \frac{\hat{\sigma}_I}{\sqrt{n}} \leq \rho_I \leq \hat{\rho}_I + z_{\alpha/2} \frac{\hat{\sigma}_I}{\sqrt{n}} \right\}, \quad (14)$$

$$\mathcal{C}_{I,n}(1 - \alpha) = \left\{ \eta_I \in \mathbb{R}^2 \mid (\hat{\eta}_I - \eta_I)^T \left(\hat{\Sigma}_I/n \right)^{-1} (\hat{\eta}_I - \eta_I) \leq \chi_2^2(1 - \alpha) \right\}. \quad (15)$$

Here $\hat{\Sigma}_I$ is obtained by replacing d in $\hat{\Sigma}$ (6) with d_I and we plug in the estimates $\hat{\eta}_I = (\hat{V}_{I,M}, \hat{V}_{I,F})^T$.

Figure 2 depicts random objects X following a uniform distribution on the upper hemisphere $\mathbb{S}_+^2 := \{(x, y, z) \mid x^2 + y^2 + z^2 = 1, z \geq 0\}$, perturbed by truncated Gaussian noise $TN_{[-1.5, 1.5]^3}(\mathbf{0}, \sigma^2 \mathbf{I}_3)$, restricted to the domain $[-1.5, 1.5]^3 \subset \mathbb{R}^3$, where $\mathbf{0} = (0, 0, 0)^T$, and \mathbf{I}_3 is the identity matrix. As the noise variance σ^2 increases, the intrinsic space \mathcal{A} induced by the probability measure \mathcal{P} transitions from the positively curved space \mathbb{S}_+^2 for small σ to the flat ambient space \mathbb{R}^3 for larger σ . The rightmost panel illustrates the confidence interval $\mathcal{I}_{I,n}(1 - \alpha)$ in (14) for the intrinsic curvature ρ_I in dependence on σ for $\alpha = 0.05$. Notably, when σ is small, the interval indicates a positive intrinsic curvature for \mathcal{A} and does not include 0; as σ increases, the interval starts to include 0, so that the no curvature null hypothesis cannot be rejected anymore.

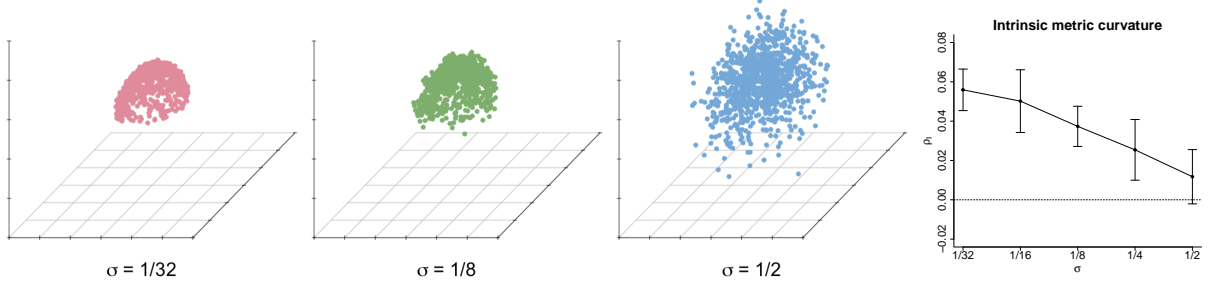


Figure 2: Random samples following a uniform distribution on \mathbb{S}_+^2 perturbed with truncated Gaussian error $TN_{[-1.5, 1.5]^3}(\mathbf{0}, \sigma^2 \mathbf{I}_3)$, where $\sigma = 1/32$ (leftmost panel), $\sigma = 1/8$, (left middle panel), and $\sigma = 1/2$ (right middle panel) and confidence intervals $\mathcal{I}_{I,n}(1 - \alpha)$ in (14) for the intrinsic curvature ρ_I with $\alpha = 0.05$, as a function of σ (rightmost panel).

5 Simulations

5.1 Example 1: Distributional data with 2-Wasserstein distance

Consider a measure \mathcal{P} on the bivariate Wasserstein space, $\mathcal{W}_2(\mathbb{R}^2)$, such that the measure is positive on bivariate normal distributions \mathcal{D} with $\mathcal{P}(\mathcal{D}) = 1$, for

$$\mathcal{D} = \{N(0, \Lambda(\theta)) \mid \Lambda(\theta) = R(\theta)\Lambda_0R(\theta)^T \in \mathbb{R}^{2 \times 2}, \theta \in [0, 1]\}, \quad (16)$$

with rotation matrix $R(\theta) = \begin{pmatrix} \cos(\frac{\pi}{2}\theta) & -\sin(\frac{\pi}{2}\theta) \\ \sin(\frac{\pi}{2}\theta) & \cos(\frac{\pi}{2}\theta) \end{pmatrix}$ and $\Lambda_0 = \text{diag}(\lambda_1, \lambda_2)$, with $\lambda_1 = 4$ and $\lambda_2 = 1$. The ambient Wasserstein space $\mathcal{W}_2(\mathbb{R}^2)$ is known to exhibit positive Alexandrov curvature. However, the intrinsic curvature of a subspace $\mathcal{D} \subset \mathcal{W}_2(\mathbb{R}^2)$ may exhibit flat geometry, as random samples only depend on the one-dimensional normalized rotation angle $\theta \in [0, 1]$.

To infer the intrinsic curvature of $\mathcal{D} \subset \mathcal{W}_2(\mathbb{R}^2)$, we generate $X_i = N(0, \Lambda(\theta_i)) \in \mathcal{D}$, where $\theta_i \sim \text{Beta}(2, 2)$, $i = 1, \dots, 100$. Figure 3(a) illustrates 95% density contour plots of random bivariate normal distributions, X_i $i = 1, \dots, 100$. We can infer the intrinsic curvature of \mathcal{D} , where the observed distributions are located, by comparing the intrinsic

Fréchet variance $\hat{V}_{I,F}$ and the metric variance $\hat{V}_{I,M}$. The confidence regions $\mathcal{C}_{I,n}(1 - \alpha)$ in (15) for $\eta_I = (\eta_{I,1}, \eta_{I,2}) := (V_{I,M}, V_{I,F})^T$ are shown in Figure 3(b). Since all confidence regions intersect with $\{\eta_I \mid \eta_{I,1} = \eta_{I,2}\}$, they are compatible with an intrinsic flat geometry (although they do not establish this fact).

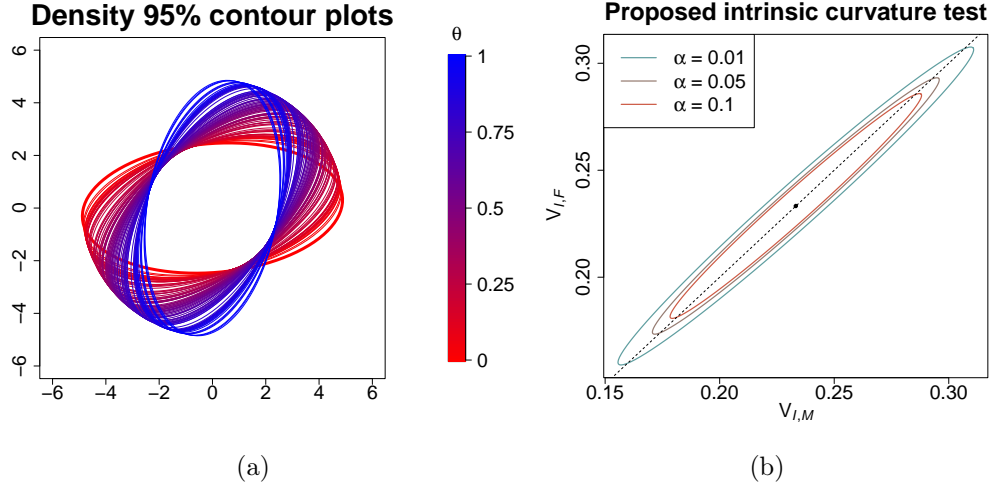


Figure 3: (a): The 95% density contour plots of random bivariate normal distributions, $X_i = N(0, \Lambda(\theta_i))$, where $\theta_i \sim \text{Beta}(2, 2)$, $i = 1, \dots, 100$, generated from the intrinsic space \mathcal{D} in (16). (b): The proposed intrinsic curvature test using the confidence regions $\mathcal{C}_{I,n}(1 - \alpha)$ in (15) with $\alpha = 0.01, 0.05, 0.1$, inferring flat intrinsic curvature of \mathcal{D} .

Thus, even though the ambient space with Wasserstein geometry is positively curved, the flat intrinsic space \mathcal{D} satisfies the assumptions of traditional manifold learning algorithms, such as ISOMAP (Tenenbaum et al. 2000), which require the space to be globally isometric to a convex subset of Euclidean space. To represent the intrinsic geodesic using ISOMAP, we follow the approach of Chen & Müller (2012).

Consider the intrinsic geodesic $\gamma(t) : [0, 1] \rightarrow \mathcal{D}$ between two observations $x, y \in \mathcal{D}$. We can then estimate the intrinsic geodesic as

$$\hat{\gamma}(t) := \hat{\psi}^{-1}(s(t)) = \hat{\psi}^{-1}((1 - t)\hat{\psi}(x) + t\hat{\psi}(y)), \quad t \in [0, 1], \quad (17)$$

where $\hat{\psi} : \mathcal{D} \rightarrow \mathbb{R}^q$ is the representation map of ISOMAP, $s(t) = (1 - t)\hat{\psi}(x) + t\hat{\psi}(y)$ is

the ISOMAP representation interpolation, and the inverse map $\hat{\psi}^{-1} : \mathbb{R}^q \rightarrow \mathcal{D}$ is estimated by the weighted barycenter of the distributional observations X_1, \dots, X_n . For $\zeta \in \mathbb{R}^q$, we estimate $\hat{\psi}^{-1}(\zeta) = \operatorname{argmin}_{\xi \in \mathcal{D}} \sum_{i=1}^n w_i(\zeta) d^2(X_i, \xi)$, where $w_i(\zeta) = \frac{\kappa(H^{-1}(\hat{\psi}(X_i) - \zeta))}{\sum_{i=1}^n \kappa(H^{-1}(\hat{\psi}(X_i) - \zeta))}$, and κ is a non-negative q -dimensional kernel, with $H = h\mathbf{I}_q$ for a suitably chosen bandwidth h . We note that this representation map requires the intrinsic space to be flat and its estimation could alternatively be implemented by Fréchet regression (Petersen & Müller 2019).

In our analysis, we use a Gaussian kernel with an intrinsic dimension of $k = 1$. We demonstrate the resulting geodesic to connect the distributions at $x = N(0, \Sigma(0))$ and $y = N(0, \Sigma(1)) \in \mathcal{D}$, illustrating the ISOMAP representation interpolation at $s(t)$, $t = 0, 0.25, 0.5, 0.75$, and 1 in Figure 4(a) and the intrinsic geodesic $\hat{\gamma}(t) = \hat{\psi}^{-1}(s(t))$ in Figure 4(b). Due to the flat intrinsic curvature $\rho_I = 0$ of \mathcal{D} , as ascertained with the proposed method, the ISOMAP-based intrinsic geodesics $\hat{\gamma}(t)$ in (17) successfully maintain the same ratio between the two eigenvalues of the covariance matrix along the entire geodesic from $t = 0$ to $t = 1$, corresponding to an interpretable and insightful rotation of the visualized contour ellipse.

As a comparison method, we consider the Wasserstein geodesic that is defined in the ambient (rather than intrinsic) geometry. For two bivariate normal distributions $N(0, U)$, and $N(0, V)$, the Wasserstein geodesic $\gamma_W(t)$ is

$$\gamma_W(t) = N(0, W(t)), \quad W(t) = \{(1-t)\mathbf{I}_2 + tT\} U \{(1-t)\mathbf{I}_2 + tT\}, \quad (18)$$

where $T = V^{\frac{1}{2}}(V^{\frac{1}{2}}UV^{\frac{1}{2}})^{-\frac{1}{2}}V^{\frac{1}{2}}$, for $t \in [0, 1]$ (Takatsu 2011). Figure 4(c) shows that the Wasserstein geodesic paths between $x = N(0, \Sigma(0))$, and $y = N(0, \Sigma(1))$ go through a spherical shape at the halfway point and thus leave the intrinsic space. Thus they are far less intuitive and lack interpretability (see Section 6.1 for a data example).

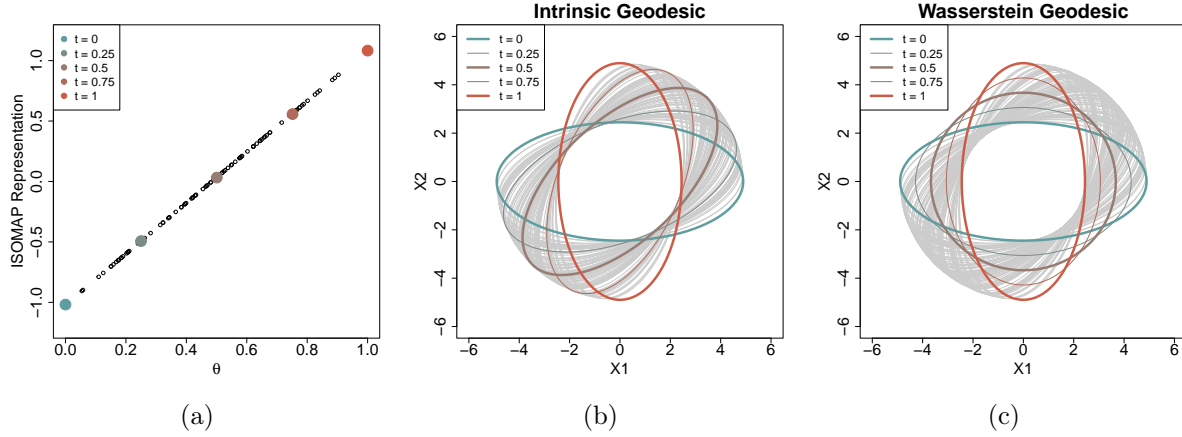


Figure 4: (a) ISOMAP representation interpolation $s(t)$ for random bivariate normal distributions, X_1, \dots, X_{100} , generated from the intrinsic space \mathcal{D} in (16) as a function of normalized rotation angle $0 \leq \theta \leq 1$. (b) Estimated intrinsic geodesic path $\hat{\gamma}(t)$ in (17) and (c) Wasserstein ambient geodesic path $\gamma_W(t)$ in (18) between blue ($t = 0$) and red ($t = 1$) ellipse, represented by 95% density contour plots.

5.2 Example 2: Point cloud data with intrinsic distance

Here we apply the proposed test to ascertain intrinsic curvature for point cloud data. Many problems in statistical machine learning involve data where each data point is drawn from an underlying probability density situated in an unknown intrinsic space (Lee et al. 2022, Chew et al. 2022). The data clouds delineate the spatial locations of objects within an ambient space, while the curvature of the intrinsic space is of interest but remains elusive. We consider a Euclidean ambient space \mathbb{R}^3 with strict subspaces $\mathcal{B}_1, \mathcal{B}_2, \mathcal{B}_3 \subset \mathbb{R}^3$ given by

$$\mathcal{B}_1 = \{(x, y, z) \in \mathbb{R}^3 \mid x^2 + y^2 + z^2 = 1, z \geq 0\},$$

$$\mathcal{B}_2 = \{(x, y, z) \in \mathbb{R}^3 \mid x^2 - y^2 - z^2 = -1, 0 \leq z \leq 4\},$$

$$\mathcal{B}_3 = \{(x, y, 0) \in \mathbb{R}^3 \mid 0 \leq x, y \leq 1\},$$

where \mathcal{B}_1 represents the open upper hemisphere, \mathcal{B}_2 is a hyperboloid obtained by rotating a hyperbolic graph around the z -axis and \mathcal{B}_3 is a plane. These spaces are positively curved, negatively curved and flat, respectively. We generate i.i.d. point cloud data for each of

these spaces as follows: For $i = 1, \dots, n$,

$$(x_{1i}, y_{1i}, z_{1i}) = (\cos \theta_i \sin \psi_i, \sin \theta_i \sin \psi_i, \cos \psi_i) \in \mathcal{B}_1, \quad \psi_i \sim U[0, \pi/2], \quad \theta_i \sim U[0, 2\pi];$$

$$(x_{2i}, y_{2i}, z_{2i}) = (v_i, \sqrt{1 + v_i^2} \cos \theta_i, \sqrt{1 + v_i^2} \sin \theta_i) \in \mathcal{B}_2, \quad v_i \sim TN_{[-r, r]}(0, 1), \quad \theta_i \sim U[0, \pi];$$

$$(x_{3i}, y_{3i}, z_{3i}) = (\mu_i, \nu_i, 0) \in \mathcal{B}_3, \quad \mu_i, \nu_i \sim U[0, 1].$$

Here $U[a, b]$ denotes a uniform distribution over the interval $[a, b]$, and $TN_{[-r, r]}(0, 1)$ is a one-dimensional truncated normal distribution with mean 0 and variance 1, restricted to the interval $[-r, r]$, where $r = \sqrt{15}$.

In real world settings, observations usually are not exactly on target, but are corrupted by errors; we reflect this by incorporating small perturbations $(\tilde{x}_{li}, \tilde{y}_{li}, \tilde{z}_{li}) = (x_{li}, y_{li}, z_{li}) + \epsilon_{li}$, $\epsilon_{li} \sim N(\mathbf{0}, \sigma^2 \mathbf{I}_3)$, where $\mathbf{0} = (0, 0, 0)^T$ and \mathbf{I}_3 is a 3×3 identity matrix, $l = 1, 2, 3, \quad i = 1, \dots, n$, where the sample size was $n = 1000$ and the noise level σ was set to $\frac{1}{10}$. The first row of Figure 5 displays the data clouds $\{(\tilde{x}_{li}, \tilde{y}_{li}, \tilde{z}_{li})\}_{i=1}^n$ for each space \mathcal{B}_l , $l = 1, 2, 3$.

The intrinsic geodesic distance $d_{\mathcal{B}_l}$, $l = 1, 2, 3$, can be obtained from the given Euclidean input distance using Algorithm 1. We emphasize that this approach relies solely on Euclidean distance to estimate intrinsic geodesic distances and does not utilize any information about the curvature of the latent spaces. For each space \mathcal{B}_l , we estimate the sample intrinsic Fréchet mean $\hat{\mu}_{I,\oplus}$, Fréchet variance $\hat{V}_{I,F}$ and metric variance $\hat{V}_{I,M}$, using error-perturbed samples $\{(\tilde{x}_{li}, \tilde{y}_{li}, \tilde{z}_{li})\}_{i=1}^n$ as input.

The second row of Figure 5 illustrates $100(1 - \alpha)\%$ confidence regions $\mathcal{C}_{I,n}(1 - \alpha)$ in (15) for $\eta_I = (\eta_{I,1}, \eta_{I,2}) := (V_{I,M}, V_{I,F})^T$ and $\alpha = 0.01, 0.05, 0.1$. The intrinsic space corresponding to data cloud $\{(\tilde{x}_{1i}, \tilde{y}_{1i}, \tilde{z}_{1i})\}_{i=1}^n$ in the first column is found to exhibit significant positive curvature, as the confidence regions $\mathcal{C}_{I,n}(1 - \alpha)$ are contained in the set $\{\eta_I \mid \eta_{I,1} < \eta_{I,2}\}$ for all three values of α . Analogously, the intrinsic space corresponding to the point cloud

$\{(\tilde{x}_{2i}, \tilde{y}_{2i}, \tilde{z}_{2i})\}_{i=1}^n$ in the second column is found to have significant negative curvature, while for the point cloud $\{(\tilde{x}_{3i}, \tilde{y}_{3i}, \tilde{z}_{3i})\}_{i=1}^n$ in the third column one cannot reject the null hypothesis that $H_0 : \mathcal{P} \in \Theta_0$, where $\Theta_0 : \{\eta_I \mid \eta_{I,1} = \eta_{I,2}\}$, which is compatible (but does not establish) no significant curvature. Thus the actual curvature is correctly assessed.

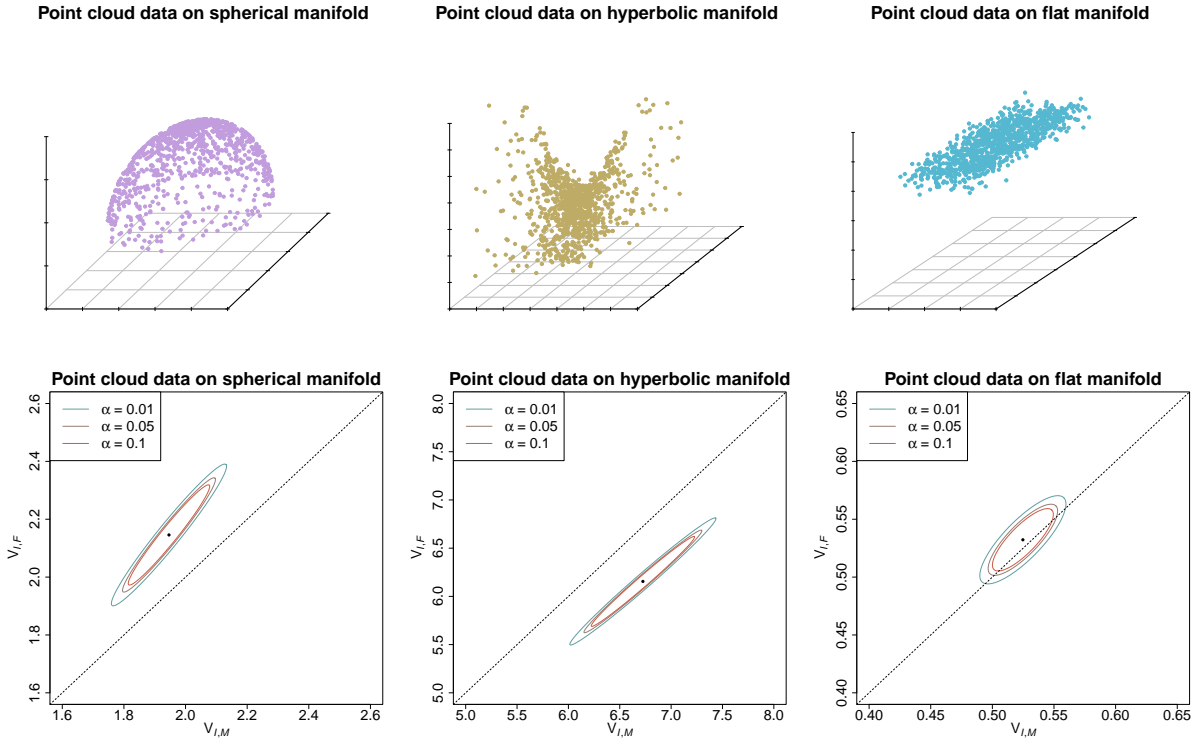


Figure 5: (First row) Simulated data clouds $\{(\tilde{x}_{li}, \tilde{y}_{li}, \tilde{z}_{li})\}_{i=1}^n$ located in the subspaces \mathcal{B}_l , $l = 1, 2, 3$ of \mathbb{R}^3 , with some noise added. (Second row) The proposed intrinsic curvature test utilizing confidence regions $\mathcal{C}_{I,n}(1 - \alpha)$ for η_I in (15) that are obtained with the respective data cloud in the same column as input, for levels $\alpha = 0.01, 0.05, 0.1$. This provides evidence for positive, negative and flat intrinsic curvature, respectively.

Table 1 shows confidence intervals $\mathcal{I}_{I,n}(1 - \alpha)$ in (14) for the intrinsic curvature ρ_I , corresponding to each data cloud $\{(\tilde{x}_{li}, \tilde{y}_{li}, \tilde{z}_{li})\}_{i=1}^n$ sampled from \mathcal{B}_l , $l = 1, 2, 3$ at confidence levels $\alpha = 0.01, 0.05$, and 0.1 , with intervals widening for smaller α and confirming that the proposed curvature measure correctly detects the intrinsic curvature of these spaces.

Table 1: Confidence intervals $\mathcal{I}_{I,n}(1 - \alpha)$ in (14) for the intrinsic curvatures ρ_I of point cloud data generated from the underlying manifolds \mathcal{B}_1 , \mathcal{B}_2 , and \mathcal{B}_3 .

	\mathcal{B}_1	\mathcal{B}_2	\mathcal{B}_3
$\alpha = 0.1$	(0.083, 0.122)	(-0.093, -0.077)	(-0.009, 0.038)
$\alpha = 0.05$	(0.080, 0.125)	(-0.095, -0.075)	(-0.014, 0.042)
$\alpha = 0.01$	(0.072, 0.132)	(-0.098, -0.072)	(-0.023, 0.051)

6 Data illustrations

6.1 Gait synchronization analysis

Human gait analysis is critical in medical research due to its potential to reveal the impact of various pathologies, such as Parkinson’s disease and arthritis, which can lead to reduced mobility and increased fall risk (Bachlin et al. 2009, Barrois et al. 2015). For this analysis, we use gait time series data collected between April 2014 and October 2015. For detailed information about the collection process and a comprehensive description of the data we refer to Truong et al. (2019). The data are available at <https://github.com/deepcharles/gait-data>.

We used measurements from Inertial Measurement Units (IMUs) attached on the foot of 52 participants in the healthy group with no known medical issues, and another 52 participants in the orthopedic disorders group, who had lower limb osteoarthritis or cruciate ligament injuries. We considered the \mathbb{R}^2 -valued time signal corresponding to the angular velocity (in deg/s) along the vertical axis perpendicular to the ground (referred to as the V-axis) and along the axis perpendicular to the sensor placed on a tilted dorsum of the foot for each participant (referred to as the Z-axis). Each recorded signal corresponds to a gait cycle in which participants stand for 6 seconds, walk 10 meters at their preferred walking speed on a level surface to a designated turn point, turn around, walk back to the

starting point, and finally stand for 2 seconds.

For each participant, we computed a 2×2 SPD sample covariance matrix to measure the degree of synchronization between the V- and Z- axes from the bivariate signal data vectors. Consider X_1, \dots, X_{n_1} , as the SPD matrices for $n_1 = 52$ participants in the healthy group and Y_1, \dots, Y_{n_2} , as the SPD matrices for $n_2 = 52$ participants in the orthopedic disorders group. We consider the SPD matrices of size 2×2 , denoted by $\mathcal{S}_{++}^2 = \{X \in \mathbb{R}^{2 \times 2} : X^T = X, X > 0\}$ with the Bures-Wasserstein metric in the ambient space of SPD matrices, $d_{BW}(U, V) = \left[\text{trace}(U) + \text{trace}(V) - 2\text{trace}(U^{\frac{1}{2}}VU^{\frac{1}{2}})^{\frac{1}{2}} \right]^{\frac{1}{2}}$. This metric is also known as the Bures distance in quantum information and is closely related to the Wasserstein metric for Gaussian distributions (Bhatia et al. 2019). We provide additional sensitivity analysis results on the choice of ambient metrics d for the space of SPD matrices in Section S.6 of the Supplement.

To infer the curvature of the underlying subset of \mathcal{S}_{++}^2 in which the observed gait synchronizations are located, we compare the intrinsic Fréchet variance $\hat{V}_{I,F}$ and metric variance $\hat{V}_{I,M}$. The confidence regions $\mathcal{C}_{I,n}(1-\alpha)$ in (15) for $\eta_I = (\eta_{I,1}, \eta_{I,2}) := (V_{I,M}, V_{I,F})^T$ and $\alpha = 0.1, 0.05, 0.01$ for healthy and orthopedic disorders group are illustrated in Figure 6(a) and 6(b). Specifically, for the healthy group (X_1, \dots, X_{n_1}) , the confidence regions all intersect with $\{\eta_I \mid \eta_{I,1} = \eta_{I,2}\}$ so that there is no evidence for the presence of curvature. For the participants of orthopedic group (Y_1, \dots, Y_{n_2}) , the confidence region is contained in the set $\{\eta_I \mid \eta_{I,1} \neq \eta_{I,2}\}$ at level $\alpha = 0.01$, indicating the presence of negative curvature. As the observed matrices for the healthy group are compatible with an intrinsic flat curvature, we estimate the intrinsic geodesic $\hat{\gamma}(t)$ defined in (17) with ISOMAP.

In Figure 6(c), the geodesic from $t = 0$ to $t = 1$ moves smoothly in a counter-clockwise direction at a constant speed for the healthy group. However, as shown in Figure 6(d),

for the group with orthopedic disorders, the negative curvature implies that the ISOMAP representation of the intrinsic geodesic works less well. For instance, from $t = 0$ to $t = 0.5$, the path expands at a constant speed while maintaining the same eigenvectors. However, at $t = 0.75$, the eigenvector deviates significantly from this trajectory, but subsequently returns to the original direction at $t = 1$. We also provide the confidence intervals $\mathcal{I}_{I,n}(1-\alpha)$ in (14) for ρ_I in Table 2.

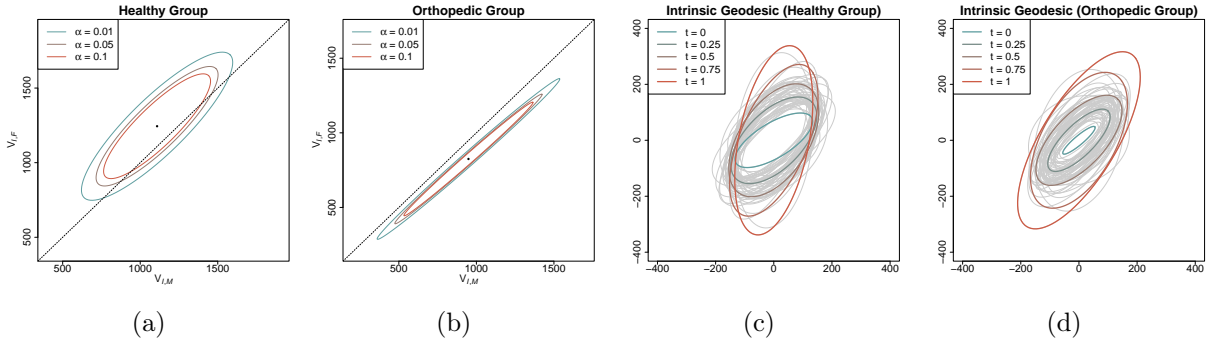


Figure 6: (a), (b): Confidence regions $\mathcal{C}_{I,n}(1 - \alpha)$ in (15) for η_I representing gait synchronization SPD matrices for healthy and orthopedic disorder groups, with $\alpha = 0.01, 0.05, 0.1$. (c): Intrinsic geodesic $\hat{\gamma}(t)$ in (17) from the blue observation ($t = 0$) to red ($t = 1$), for the healthy group. (d): Intrinsic geodesic $\hat{\gamma}(t)$ in (17) from the blue observation ($t = 0$) to red ($t = 1$), for the orthopedic disorder group.

6.2 Energy source data

Data on energy sources for electricity generation across the United States, expressed as fractions or percentages, are available at <https://www.eia.gov/electricity/data/state/> and represent compositional data (Zhu & Müller 2024). In our analysis, we consider three categories of energy sources: 1) U_1 : Proportion of Coal or Petroleum for electricity generation, 2) U_2 : Proportion of Natural Gas, and 3) U_3 : Proportion of other sources, including Nuclear, Geothermal, Hydroelectric and Solar Thermal.

Given the compositional nature of the data, we represent each data point as a point on the unit sphere S^2 by applying a square root transformation (Dai 2022, Scealy & Welsh

Table 2: Confidence intervals $\mathcal{I}_{I,n}(1 - \alpha)$ in (14) for the intrinsic curvature ρ_I for the gait synchronization data.

	Healthy Group	Orthopedic Disorders Group
$\alpha = 0.1$	(-0.014, 0.259)	(-0.167, -0.095)
$\alpha = 0.05$	(-0.040, 0.285)	(-0.174, -0.088)
$\alpha = 0.01$	(-0.092, 0.336)	(-0.187, -0.074)

2014). Specifically, denoting the monthly energy composition data from January 2012 to December 2021 by $X_i = (\sqrt{U_{i1}}, \sqrt{U_{i2}}, \sqrt{U_{i3}})$, where $U_{i1}, U_{i2}, U_{i3} \geq 0$ and $U_{i1} + U_{i2} + U_{i3} = 1$ for all $i = 1, \dots, 120$, we consider the positive quadrant of the sphere $X_i \in \mathbb{S}_+^2$, where $\mathbb{S}_+^2 = \{(x, y, z) \in \mathbb{R}^3 \mid x^2 + y^2 + z^2 = 1, x, y, z \geq 0\}$, with geodesic distance as the ambient space. If the intrinsic space of energy fractions samples corresponds to the entire ambient space \mathbb{S}_+^2 , the intrinsic curvature ρ_I should be positive, since the ambient space is the positively curved sphere.

Figure 7(a) demonstrates that the intrinsic curvature ρ_I is actually not that far from being flat, indicating that the curvature of the intrinsic space, where the observations are actually located, differs from that of the ambient space \mathbb{S}_+^2 . This then justifies to utilize the intrinsic geodesic $\hat{\gamma}(t)$ in (17) as obtained by ISOMAP, which a priori would not be possible for data located on the sphere. Figure 7(b) indicates that the estimated intrinsic geodesics $\hat{\gamma}(t)$ effectively capture the trajectories of these compositional data, and as per Figure 7(c) energy sourcing moves in a linear direction from past to present.

7 Discussion

The study of dispersion measures, specifically metric variance and Fréchet variance, is of general interest for the emerging field of random objects in general metric spaces. The CLT for the joint distribution of these dispersion estimates enables more detailed comparisons

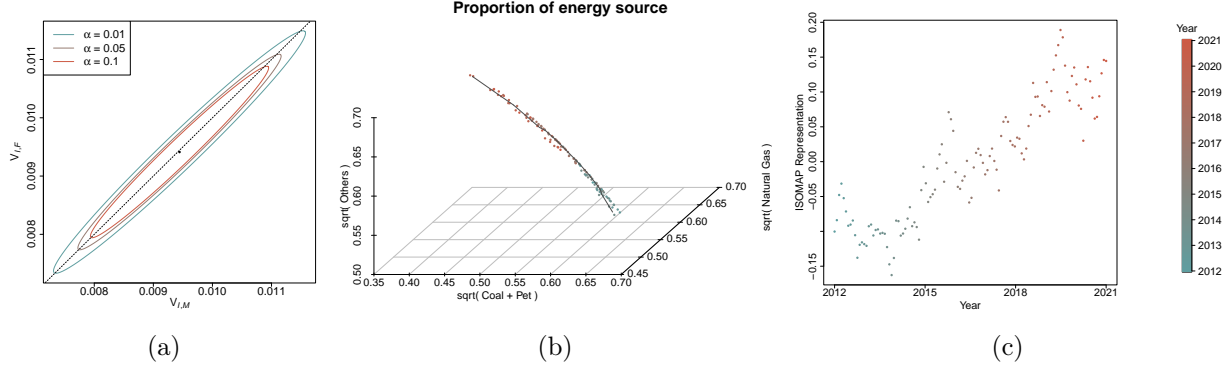


Figure 7: (a) Confidence regions $\mathcal{C}_{I,n}(1 - \alpha)$ in (15) for energy compositional data with $\alpha = 0.01, 0.05, 0.1$. (b) Energy proportional data trajectory from January 2012 (blue) to December 2021 (red) with its intrinsic geodesic $\hat{\gamma}(t)$ in (17) (black solid line). (c) Corresponding ISOMAP representation interpolation $s(t)$ as a function of year.

and we discovered that the relation between these two measures contains information about the curvature of the metric space. Tools from metric geometry and empirical processes make it possible to obtain theory-supported inference for the underlying curvature.

Another important application of these results is the inference of intrinsic curvature in a sample of random objects when the underlying probability measure is concentrated on a potentially curved subspace, such as a curved manifold embedded in an ambient metric space, which may itself be either flat or curved. Determining intrinsic curvature has high relevance for real data analysis as we demonstrate with SPD matrices corresponding to gait synchronization and energy compositional data located on the sphere. While we do not make use of the ISOMAP algorithm of [Tenenbaum et al. \(2000\)](#) for the proposed intrinsic curvature test, if it is discovered by applying the test that the curvature of \mathcal{A} is compatible with that of a flat space, one can confidently use ISOMAP to represent \mathcal{A} as the image of a map from \mathbb{R}^p to \mathcal{A} . So one application of the proposed test for curvature is to determine whether the assumptions of ISOMAP are satisfied.

Several avenues for future research present themselves. These include a rigorous convergence analysis of the estimated intrinsic distance for general subspaces $\mathcal{A} \subset \mathcal{M}$ and also

the choice of an appropriate metric d . Investigating the impact of the metric choice on statistical inference and geometric analysis remains an important open problem.

Supplementary Materials

The supplementary materials include all proofs, additional simulations for power analysis, further illustrations of curvature inference for the MNIST image and temperature distribution data, convergence analysis of intrinsic distance estimation, sensitivity analysis for the choice of input distance d and verification of required conditions for both simulations and real data analysis.

Funding

This research was supported in part by NSF grant DMS-2310450.

Supplement to ‘‘Inference for Dispersion and Curvature of Random Objects’’

Abstract

Section S.1 presents additional simulation results for spaces of symmetric positive definite (SPD) matrices using six different distance metrics, as well as for spherical data and high-dimensional Euclidean random objects with low intrinsic dimension. We also provide a power and Type I error analysis. Additional real data analyses can be found in Section S.2 for the MNIST image dataset and a temperature data set. Section S.3 discusses the convergence results of intrinsic distance estimation obtained by Algorithm 1 in Section 4.2. Section S.4 provides the proofs of the main results in the paper. Section S.5 verifies the conditions assumed in our theorems for both simulations and real data analyses in the main manuscript. Section S.6 conducts a sensitivity analysis for the choice of input distance d in our proposed intrinsic curvature test introduced in Section 4.2. Section S.7 examines the relationship between Alexandrov curvature and our proposed metric curvature.

S.1 Additional simulation results

This section provides simulations, illustrating estimation and inference for the curvature and also how curvature may vary within the same space when employing different metrics. Specifically, this section provides additional examples, including SPD matrices with 6 different distance metrics, spherical data with geodesic distance, and high-dimensional Euclidean random objects with low intrinsic dimension. We also provide a power and Type I error analysis.

S.1.1 Spaces of symmetric positive definite matrices

The study of SPD matrices is relevant for various machine learning domains, including medical imaging, natural language processing, computer vision, and modeling time-varying data. The space of SPD matrices of size $p \times p$, denoted by \mathcal{S}_{++}^p , form a smooth manifold and is defined as

$$\mathcal{S}_{++}^p = \{X \in \mathbb{R}^{p \times p} : X^T = X, X > 0\}.$$

We generated random SPD matrices $X = V\Lambda V^T$, where $V = (\vec{v}_1/\|\vec{v}_1\|, \dots, \vec{v}_p/\|\vec{v}_p\|)$, with \vec{v}_l sampled independently and identically distributed (i.i.d.) from the Gaussian distribution $N_p(0, I_p)$, and setting $\Lambda = \text{diag}(\lambda_1, \dots, \lambda_p)$, $\lambda_l \sim \nu \times \text{Beta}(\beta, \gamma)$, $l = 1, \dots, p$, with $\beta = 3$, $\gamma = 5$, $\nu = 100$, and $p = 3$. We studied six different metrics: (a) Frobenius (Frob), (b) log-Euclidean (log-E), (c) power Frobenius with power $\frac{1}{2}$ (p-Frob), (d) Cholesky (Chol), (e) Affine-Invariant Riemannian (AIR), and (f) Bures-Wasserstein (BW) metric.

Figure S.1(a) depicts the ratios of metric variance V_F over Fréchet variance V_M for samples each with $n = 100$ SPD matrices for these six metrics. It is known that the spaces of SPD matrices \mathcal{S}_{++}^p with the Cholesky and Frobenius metrics (including the log-Frobenius and

power Frobenius metrics) are flat, and accordingly the Fréchet variance V_F and the metric variance V_M are equal.

Figure S.1(a) aligns with established findings that the curvature of the Riemannian manifold with the affine-invariant metric is a non-positively curved space (Bhatia 2009), whereas the curvature of the SPD manifold with the BW metric has non-negative curvature (Han et al. 2021), as outlined in Section 3. Figure S.1(b)-S.1(c) illustrate the confidence regions $\mathcal{C}_n(1 - \alpha)$ in (7) for $\eta = (\eta_1, \eta_2)^T = (V_M, V_F)^T$, computed for the sample of SPD matrices using the AIR and BW metrics, with $\alpha = 0.01, 0.05$, and 0.1 . These confidence regions establish the significance of the negative and positive curvature as determined from the sample for the AIR and BW metric, respectively, as these confidence regions are contained within the sets $\{\eta \mid \eta_1 > \eta_2\}$, and $\{\eta \mid \eta_1 < \eta_2\}$, respectively. These results thus confirm Theorems 2 and 3.

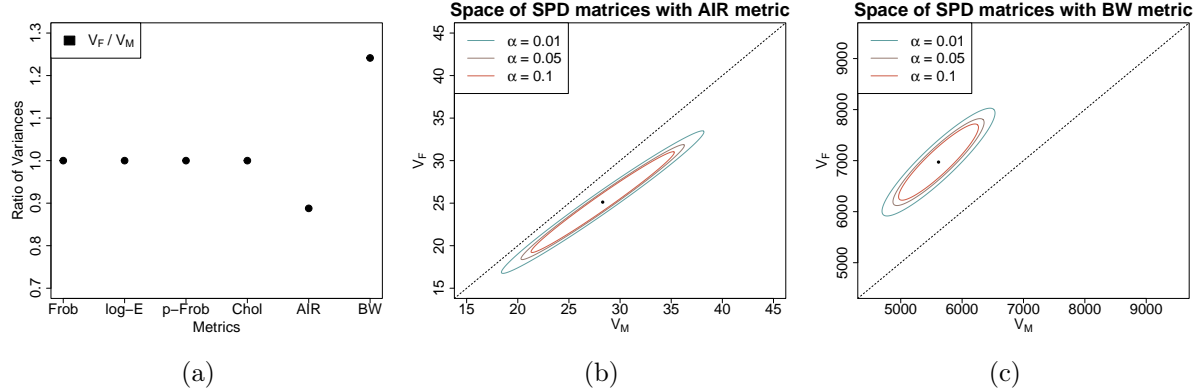


Figure S.1: (a) Ratio of the two dispersion measures $\eta = (V_M, V_F)^T$ for a sample of size 100 for random SPD matrices \mathcal{S}_{++}^p using 6 different metrics (Frob, log-E, p-Frob, Chol, AIR, and BW). (b), (c) Corresponding confidence regions $\mathcal{C}_n(1 - \alpha)$ in (7) for the SPD spaces with the AIR and BW metrics, with $\alpha = 0.01, 0.05$, and 0.1 , empirically inferring the underlying curvature of the space.

S.1.2 Spherical data with geodesic distance

This simulation is designed for comparing two dispersion measures and illustrating the confidence region $\mathcal{C}_n(1 - \alpha)$ in (7). Spherical data are common in applications, including geographical data on \mathbb{S}^2 (Zheng 2015) and distributional data on the Hilbert sphere \mathbb{S}^∞ (Dai 2022). In positively curved spaces such as the space of spherical data, quantifying the dispersion of data using the metric variance V_M is often preferable, as obtaining the Fréchet mean and the traditional Fréchet variance V_F can be numerically challenging.

We consider here random objects taking values on the upper hemisphere $\mathbb{S}_+^2 \subset \mathbb{S}^2$,

$$\mathbb{S}_+^2 = \{(x, y, z) \in \mathbb{R}^3 \mid x^2 + y^2 + z^2 = 1, z \geq 0\},$$

equipped with the geodesic distance. In this scenario, the Fréchet mean μ_\oplus of X is unique with $\mu_\oplus = (0, 0, 1)$. We generated $n = 50$ spherical data points, X_1, \dots, X_n from a uniform distribution on \mathbb{S}_+^2 and obtained estimates of the Fréchet variance V_F and the metric variance V_M .

Figure S.2 illustrates the $100(1 - \alpha)\%$ confidence region of the joint distribution for $\eta = (\eta_1, \eta_2) = (V_M, V_F)^T$, denoted as $\mathcal{C}_n(1 - \alpha)$ in (7), with $\alpha = 0.01, 0.05$, and 0.1 . We infer that the space \mathbb{S}_+^2 with geodesic distance exhibits positive curvature with a confidence level exceeding 99% as $\mathcal{C}_n(1 - \alpha) \subset \Theta_1$, where $\Theta_1 = \{\eta \mid \eta_1 < \eta_2\}$ under $H_1 : \mathcal{P} \in \Theta_1$.

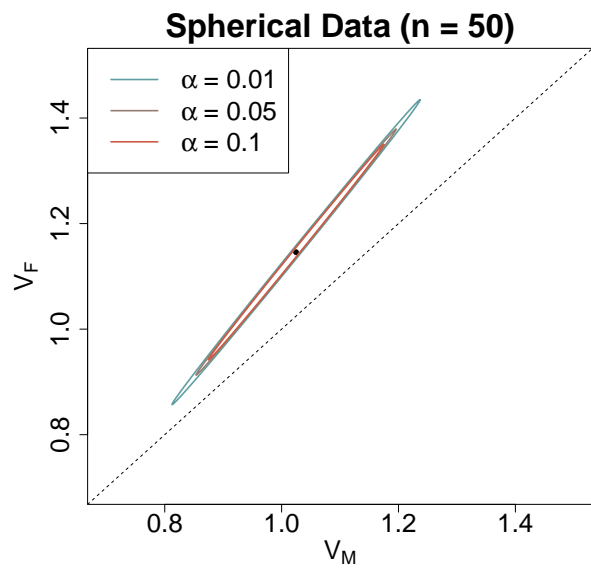


Figure S.2: Confidence regions $\mathcal{C}_n(1 - \alpha)$ for η in (7) using $n = 50$ uniform samples on the open half sphere of \mathbb{S}^2_+ with $\alpha = 0.01, 0.05, 0.1$, showing that the proposed curvature measure correctly detects the positive curvature.

S.1.3 Power and Type-I error analysis

To illustrate the finite-sample performance of the proposed intrinsic curvature test in Section 4.2, we conducted power and Type-I error analyses. Specifically, we consider the three-dimensional Euclidean space (\mathcal{M}, d) as the ambient space and define the intrinsic space \mathcal{D}_κ as

$$\mathcal{D}_\kappa = \left\{ (x, y, z) \in \mathbb{R}^3 \mid x^2 + y^2 + z^2 = \left(\frac{1}{\sqrt{\kappa}}\right)^2, \frac{1}{\sqrt{\kappa}} \cos\left(\frac{\pi\sqrt{\kappa}}{4}\right) \leq z \leq \frac{1}{\sqrt{\kappa}} \right\},$$

for $0 < \kappa \leq 1$. This space corresponds to a sphere of radius of $\frac{1}{\sqrt{\kappa}}$, which is known to have Alexandrov curvature κ . The constraint on the z -axis $\frac{1}{\sqrt{\kappa}} \cos\left(\frac{\pi\sqrt{\kappa}}{4}\right) \leq z \leq \frac{1}{\sqrt{\kappa}}$ ensures that the diameters of \mathcal{D}_κ are identical and equal to $\frac{\pi}{2}$ under the spherical geodesic distance for all $\kappa > 0$.

For the Type-I error analysis, we also consider the following flat null space:

$$\mathcal{D}_0 = \left\{ (x, y, 0) \in \mathbb{R}^3 \mid 0 \leq x, y \leq \frac{\pi}{2\sqrt{2}} \right\}.$$

In the first scenario, we generate random objects X_1, \dots, X_n of size $n = 200, 500, 1000$, following a uniform distribution on \mathcal{D}_κ , for all $\kappa \geq 0$. We performed 500 Monte Carlo simulations to construct empirical power functions, where the empirical power was assessed as the proportion of test rejections at a significance level of $\alpha = 0.05$ over the 500 runs.

Figure S.3 presents the results. When the curvature parameter is $\kappa = 0$, the power functions remain close to 0.05, indicating appropriate Type-I error control. For a fixed sample size n , the power increases as the curvature κ grows. Similarly, for a fixed curvature κ , the power increases as the sample size n increases.

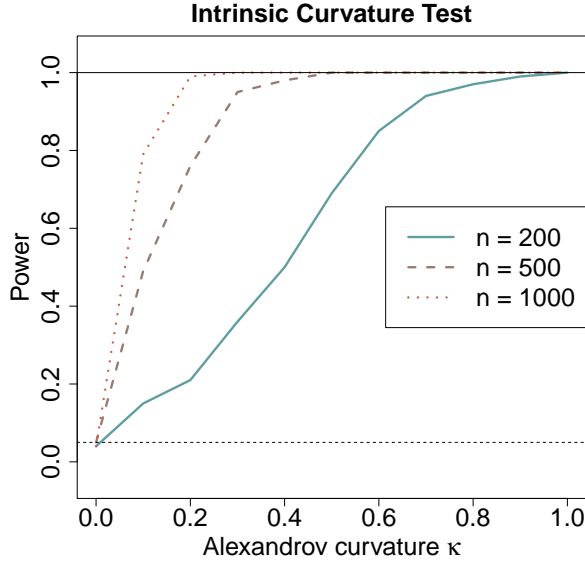


Figure S.3: Power and Type-I error analyses for increasing Alexandrov curvature κ , based on random objects X_1, \dots, X_n with sample sizes $n = 200, 500, 1000$. Each observation X_i is uniformly distributed on \mathcal{D}_κ , for $\kappa \geq 0$. The empirical power is computed as the proportion of test rejections at a significance level of $\alpha = 0.05$ over the 500 Monte Carlo simulations.

S.1.4 High-dimensional ambient Euclidean random objects with low intrinsic dimension

We consider a setting where the ambient dimensionality significantly exceeds the intrinsic dimension of the manifold. Specifically, we define the following sparse p -dimensional Euclidean space:

$$\mathcal{E}_p = \left\{ (x, y, z, 0, 0, \dots, 0) \in \mathbb{R}^p \mid x^2 + y^2 + z^2 = 1, 0 \leq z \leq 1 \right\},$$

which represents an intrinsically two-dimensional space with positive curvature, where we vary p from $p = 3$ to $p = 100$.

When the random objects lie exactly on the intrinsic manifold \mathcal{E}_p , (i.e., in the absence of noise contamination), our curvature test results remain unchanged regardless of the ambient space dimension \mathbb{R}^p . This invariance holds because, for any two points

$\xi_1 = (x_1, y_1, z_1, 0, \dots, 0)$, and $\xi_2 = (x_2, y_2, z_2, 0, \dots, 0)$, the input distance is given by $d(\xi_1, \xi_2) = (x_1 - x_2)^2 + (y_1 - y_2)^2 + (z_1 - z_2)^2$, which does not depend on the ambient dimension p .

In our second simulation, we consider an additive Gaussian noise model with noise level σ varying with the ambient dimension p . Figure S.4 illustrates the power analysis for increasing ambient space dimension p for the case of noise-contaminated random objects $\tilde{X}_1, \dots, \tilde{X}_n$, with sample sizes $n = 200, 500, 1000$. Each observation is modeled as $\tilde{X}_i = X_i + \epsilon_i$, where X_i is uniformly distributed on an intrinsically two-dimensional positively curved space \mathcal{E}_p and $\epsilon_i \sim N_p(\mathbf{0}, \sigma^2 \mathbf{I}_p)$ represents additive Gaussian noise, with $\mathbf{0} = (0, \dots, 0)^T \in \mathbb{R}^p$ and $p \times p$ identity matrix \mathbf{I}_p . The noise level σ is considered under four settings: fixed noise levels $\sigma = 0.05$ (low), 0.1 (middle), 0.2 (high), and a fixed signal-to-noise ratio of $\frac{3}{10\sqrt{p}}$.

For the low and moderate noise settings $\sigma = 0.05, 0.1$, as the ambient dimension p increases, statistical power generally decreases. This decline occurs because the signal from \mathcal{E}_p , which has intrinsic positive curvature, is increasingly overshadowed by the additive Gaussian noise, which follows a flat Euclidean structure. In the high noise case $\sigma = 0.2$, the ambient dimension p has a relatively minor effect on power. This is because even for the low-dimensional case $p = 3$, the strong noise component dominates, weakening the signal from the positively curved intrinsic space \mathcal{E}_p . Under the fixed signal-to-noise ratio setting, increasing the ambient dimension p reduces the contribution of noise in each coordinate, proportional to $1/\sqrt{p}$. This results in an increase in statistical power as p grows. Overall, our proposed tests exhibit robustness to additive ambient noise, particularly when the ambient dimension substantially exceeds the intrinsic dimension of the underlying space.

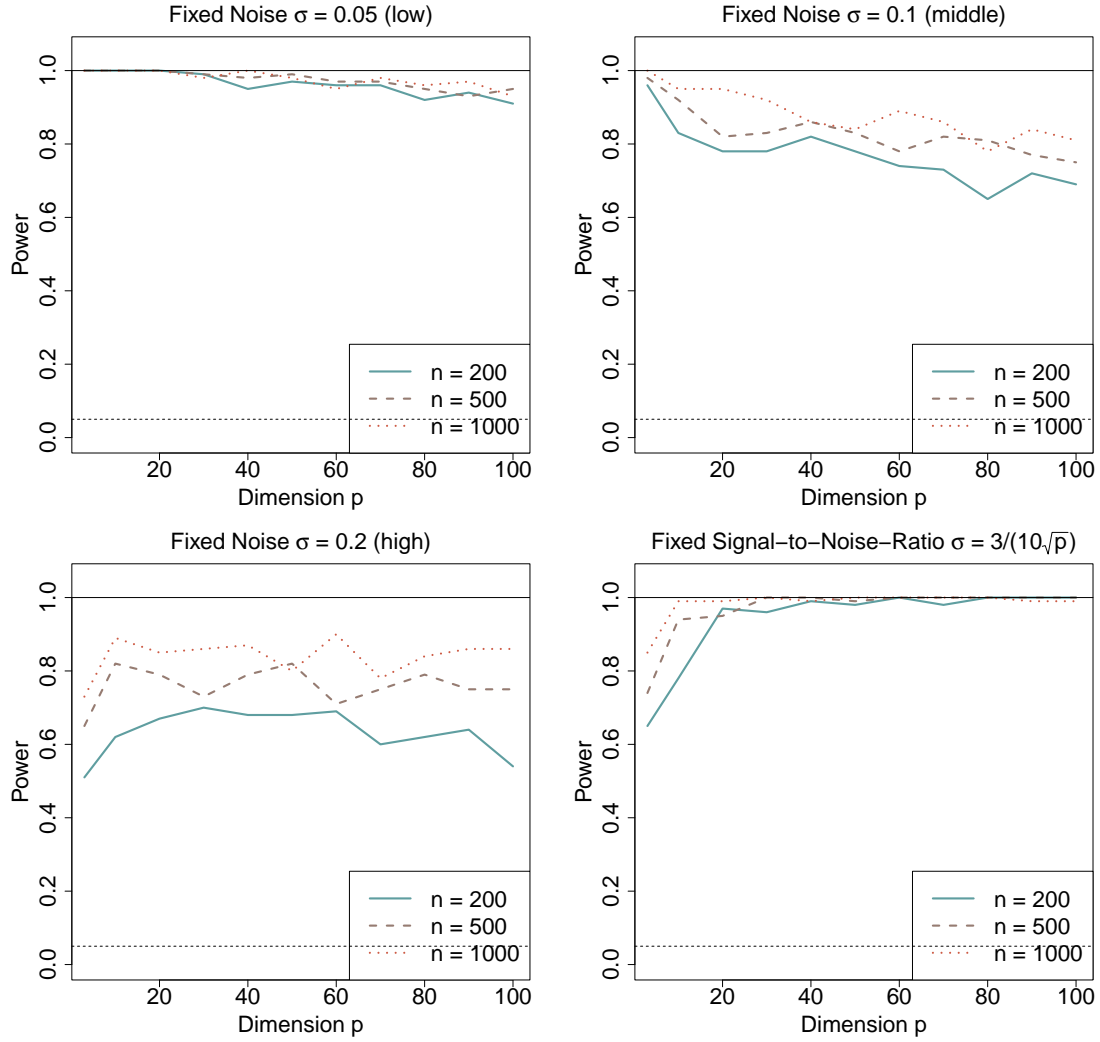


Figure S.4: Power analysis for increasing ambient space dimension p and noise-contaminated random objects $\tilde{X}_1, \dots, \tilde{X}_n$, with sample sizes $n = 200, 500, 1000$. Each observation is modeled as $\tilde{X}_i = X_i + \epsilon_i$, where X_i is uniformly distributed on an intrinsically two-dimensional positively curved space \mathcal{E}_p , and $\epsilon_i \sim N_p(\mathbf{0}, \sigma^2 \mathbf{I}_p)$ represents additive Gaussian noise. The noise level σ is considered under four settings: fixed noise levels $\sigma = 0.05$ (low), 0.1 (middle), 0.2 (high) and a fixed signal-to-noise ratio of $\frac{3}{10\sqrt{p}}$.

S.2 Additional real data analysis

S.2.1 MNIST Digits

The MNIST dataset is a widely used collection of handwritten digits, freely available for training various image processing systems. It comprises 70,000 images, each sized at 28×28 pixels, belonging to ten categories, with 60,000 images in the training set and 10,000 in the testing set. The dataset has a correct class label from a set of ten possible digits $\{0, \dots, 9\}$.

The intrinsic dimension of each digit image space might be significantly lower than the ambient space dimension of 784 (since each image is 28×28 pixels), as images of the same digits often share similar patterns. While nonlinear dimension reduction methods, including locally linear embedding, ISOMAP and Laplacian eigenmaps, have been successfully applied to image data in recent years, the intrinsic curvature of the space has not been explored yet, as far as we know. In this section, we therefore use the 60,000 images from the MNIST training set to investigate the intrinsic curvature of each digit image space.

We utilize the Euclidean distance as an ambient distance by flattening these 2D images into 1D vectors, and estimate the intrinsic curvature ρ_I in Section 4.2. Table S.1 shows the intrinsic Confidence intervals $\mathcal{I}_{I,n}(1 - \alpha)$ of each digit image space, at level $\alpha = 0.05$. We conclude that all digits are concentrated on a lower-dimensional set with positive curvature, where the curvature is most expressed for the digit 2, followed by 5 and 9, and is least expressed for the digit 8, followed by 1 and 6.

S.2.2 US airport weather station temperature distributions

The need to measure local volatility in temperatures, particularly during seasons with extreme temperatures, has long been acknowledged; see, e.g. [Donadelli et al. \(2021\)](#). We

Table S.1: Confidence intervals $\mathcal{I}_{I,n}(1 - \alpha)$ in (15) for ρ_I for the MNIST digit data.

	0	1	2	3	4	5	6	7	8	9
Num samples	5923	6742	5958	6131	5842	5421	5918	6265	5851	5949
Lower bound 95% C.I. $\mathcal{I}_{I,n}$	0.09	0.04	0.15	0.13	0.11	0.12	0.05	0.10	0.003	0.12
Upper bound 95% C.I. $\mathcal{I}_{I,n}$	0.11	0.05	0.16	0.15	0.13	0.14	0.06	0.12	0.015	0.13
Curvature	+	+	+	+	+	+	+	+	+	+

utilize daily temperature data recorded at U.S. airport weather stations, which can be obtained from <https://www.ncdc.noaa.gov/cdo-web/search?datasetid=GHCND>. Specifically, we focus on daily maximum temperatures (in Fahrenheit) during the summer period (June 21 - Sep 20) and daily minimum temperatures during the winter period (Dec 22 - Mar 21) from 39 major airports spanning 63 years (1960.06 to 2023.03).

For each station, we construct the distribution of maximum temperatures in summer and minimum temperatures in winter for every year, resulting in 63 distributions for each season, respectively. For these distributions we adopt the 2-Wasserstein metric that is frequently used for spaces of one-dimensional distributions as we consider here (Bolstad et al. 2003, Kantorovich 2006). For the i^{th} airport, we acquire the distributions for summer maximum temperatures $S_j^{(i)}$ and winter minimum temperatures $W_j^{(i)}$, for the j^{th} year, respectively, where $i = 1, \dots, 39$, $j = 1, \dots, 63$. Subsequently, the metric variances are computed for each airport to quantify the variation of the temperature distributions across all 63 years.

The estimated metric variances and 95% confidence intervals for the annual temperature distributions at selected airports are displayed in Figure S.5, where the airports with highest and lowest annual temperature volatility in summer and winter are highlighted. The Boise airport has the highest and the Palm Beach airport the lowest summer temperature

variation. Generally, airports located near the coastline have lower variation. Regarding winter temperatures, Anchorage has the highest and Los Angeles the lowest variation.

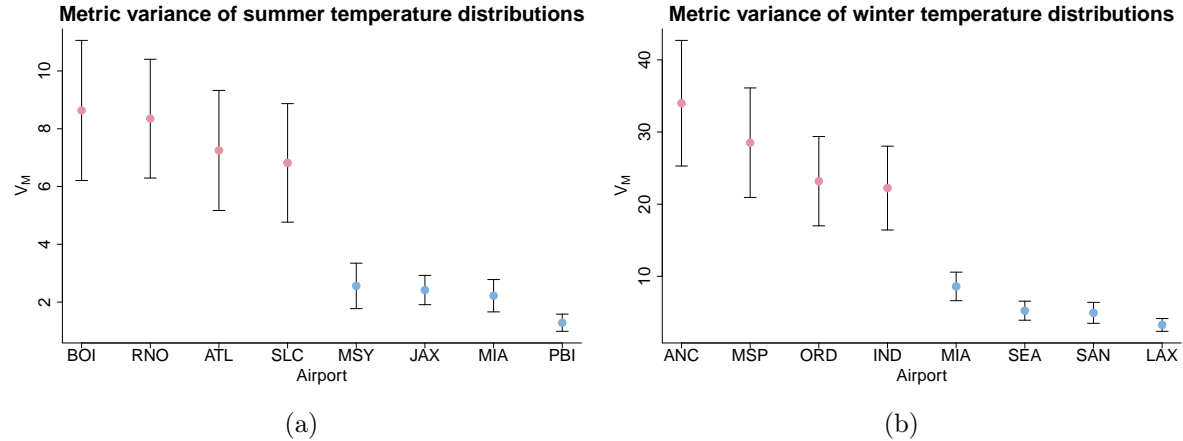


Figure S.5: The four airports with respectively highest (red) and lowest (blue) metric variances \hat{V}_M in (5) with 95% confidence intervals for summer maximum temperature probability distributions (left panel) and winter minimum temperature probability distributions (right panel), among 39 airports (BOI = Boise, RNO = Reno, ATL = Atlanta, SLC = Salt Lake City, MSY = New Orleans, JAX = Jacksonville, MIA = Miami, PBI, West Palm Beach, ANC = Anchorage, MSP = Minneapolis-Saint Paul, ORD = Chicago, IND = Indianapolis, MIA = Miami, SEA = Seattle, SAN = San Diego, LAX = Los Angeles).

S.3 Convergence of intrinsic distance estimation

Let $\mathcal{A} \subset \mathcal{M}$ be a compact set, where the ambient space (\mathcal{M}, d) is a p -dimensional Euclidean space with Euclidean distance d , and with intrinsic dimension $k < p$. The intrinsic space \mathcal{A} is said to be *K-geodesically smooth* for some positive $K > 0$, if for all $(x, y) \in \mathcal{A} \times \mathcal{A}$,

- 1) there exists a geodesic $\gamma : [0, T] \rightarrow \mathcal{A}$ from x to y , which is C^1 -smooth, i.e., it has a continuous first derivatives,
- 2) there exists a real function β such that $\lim_{t \rightarrow 0} \beta(t) = 0$ and $l(\gamma) \leq \beta(d(x, y))$, where $l(\cdot)$ is the length of the geodesic, and
- 3) the first derivative $\dot{\gamma}$ is K -Lipschitz continuous.

A probability measure \mathcal{P} supported on \mathcal{A} is said to be *ϵ -standard with respect to a measure μ* for $\epsilon > 0$, if there exists $\Delta > 0$ such that $\mathcal{P}(\mathcal{B}_\delta(x)) \geq \epsilon \mu(\mathcal{B}_\delta(x))$ for all $x \in \mathcal{A}$ and $\delta \in [0, \Delta]$.

To provide the rate of convergence for the intrinsic distance estimation, we consider the following assumptions (Aaron & Bodart 2018):

- (B1) \mathcal{A} is a k -dimensional compact manifold that is K -geodesically smooth for $K > 0$.
- (B2) The probability measure \mathcal{P} supported on \mathcal{A} is ϵ -standard with respect to the Lebesgue measure in the ambient space \mathcal{M} .

A compact manifold that is twice continuously differentiable with no boundaries satisfies assumption (B1), and if the probability distribution \mathcal{P} on \mathcal{A} has a continuous density that is bounded below by a positive constant c_0 assumption (B2) (Aaron & Bodart 2018) is satisfied. All proofs are provided in Section S.4. Let $\tilde{\rho}_{I,n}$ denote the intrinsic metric curvature obtained by replacing the intrinsic distance d_I with its estimated version \hat{d}_I .

Theorem S.1. *Suppose conditions (B1)-(B2) hold and that the weighted graph in Algorithm*

1 is constructed with ball sizes $r = r_n$ that satisfy

$$\left(A_0 \frac{\log n}{n} \right)^{2/3k} \leq r_n \leq \left(A_1 \frac{\log n}{n} \right)^{2/3k}$$

for some $A_0, A_1 > 0$. Then

$$\max_{i,j} \left| \hat{d}_I(X_i, X_j) - d_I(X_i, X_j) \right| = O \left(\left(\frac{\log n}{n} \right)^{2/3k} \right)$$

and

$$|\tilde{\rho}_{I,n} - \rho_{I,n}| = O \left(\max \left\{ \left(\frac{\log n}{n} \right)^{2/3k}, \left(\frac{1}{n} \right)^{1/2} \right\} \right) \quad a.s.$$

To explicitly build a convenience data-based sequence of ball parameters r_n only from samples for spaces that satisfy the additional assumption (B1)-(B2), the following corollary may be helpful.

Corollary S.1. *Suppose \mathcal{A} is a compact manifold that is twice differentiable with no boundaries and the probability measure \mathcal{P} is concentrated on \mathcal{A} and has a continuous density that is bounded below by a positive constant c_0 . If the weighted graph in Algorithm 1 is constructed using ball size $r = r_n = c(\max_{x \in \mathcal{X}_n} (\min_{y \neq x, y \in \mathcal{X}_n} d(x, y))^{2/3}$ for some constant $c > 0$, then*

$$\max_{i,j} \left| \hat{d}_I(X_i, X_j) - d_I(X_i, X_j) \right| = O \left(\left(\frac{\log n}{n} \right)^{2/3k} \right)$$

and

$$|\tilde{\rho}_{I,n} - \rho_{I,n}| = O \left(\max \left\{ \left(\frac{\log n}{n} \right)^{2/3k}, \left(\frac{1}{n} \right)^{1/2} \right\} \right) \quad a.s.$$

The convergence of the intrinsic distance estimation for more general subspaces $\mathcal{A} \subset \mathcal{M}$ remains an open problem. Currently, error bounds for intrinsic geodesic distances are available only under specific settings, where the ambient space (\mathcal{M}, d) is a Euclidean space

\mathbb{R}^p for some $p > 1$ and \mathcal{A} is a k -dimensional compact manifold that is C^q -smooth with a dense subset. Corollary S.1 shows that the intrinsic distance estimator \hat{d}_I , obtained from Algorithm 1 in the main paper, has an error rate bound of

$$\max_{i,j} \left| \hat{d}_I(X_i, X_j) - d_I(X_i, X_j) \right| = O \left(\left(\frac{\log n}{n} \right)^{2/3k} \right).$$

Under the further assumption that \mathcal{A} is isometric to a convex domain, this convergence rate can be improved to $O \left(\left(\frac{\log n}{n} \right)^{1/k} \right)$ (Arias-Castro et al. 2020). Aamari et al. (2023) established a new error bound of the order $O \left(\left(\frac{\log n}{n} \right)^{2/k} \right)$ by estimating the intrinsic distance using an updated algorithm with mesh construction via tangential Delaunay complexes (Boissonnat & Ghosh 2014).

S.4 Proofs and technical results

Proof of Proposition 1

Consider independent and identically distributed (i.i.d.) random objects, i.e., metric-space valued r.v.s X_1, \dots, X_n . The sample metric variance can be expressed as

$$\hat{V}_M = \binom{n}{2}^{-1} \sum_{1 \leq i < j \leq n} \psi(X_i, X_j),$$

which is the U-statistic with kernel function $\psi : \mathcal{M} \times \mathcal{M} \rightarrow \mathbb{R}$,

$$\psi(x, y) = \frac{1}{2} d^2(x, y). \quad (\text{S.19})$$

Define kernels

$$\begin{aligned} h^{(1)}(X_i) &= \mathbb{E}_{X' \mid X_i} \{ \psi(X_i, X') \mid X_i \} - V_M, \\ h^{(2)}(X_i, X_j) &= \psi(X_i, X_j) - h^{(1)}(X_i) - h^{(1)}(X_j) - V_M, \end{aligned} \quad (\text{S.20})$$

where X' is an i.i.d. copy of X_1, \dots, X_n . Then

$$\begin{aligned} \hat{V}_M &= \frac{1}{\binom{n}{2}} \sum_{1 \leq i < j \leq n} \psi(X_i, X_j) \\ &= \frac{1}{\binom{n}{2}} \sum_{1 \leq i < j \leq n} [V_M + h^{(1)}(X_i) + h^{(1)}(X_j) + h^{(2)}(X_i, X_j)] \\ &= V_M + 2 \binom{n}{1}^{-1} \sum_{i=1}^n h^{(1)}(X_i) + \binom{n}{2}^{-1} \sum_{1 \leq i < j \leq n} h^{(2)}(X_i, X_j) \\ &= V_M + 2H_n^{(1)} + H_n^{(2)}, \end{aligned} \quad (\text{S.21})$$

where

$$H_n^{(1)} = \binom{n}{1}^{-1} \sum_{i=1}^n h^{(1)}(X_i) \text{ and } H_n^{(2)} = \binom{n}{2}^{-1} \sum_{1 \leq i < j \leq n} h^{(2)}(X_i, X_j) \quad (\text{S.22})$$

are uncorrelated. This is the H-decomposition of U-statistics (Hoeffding 1961).

1) Proof of $\hat{V}_M \rightarrow V_M$ almost surely

We adopt the proofs from Section 3.4 in Lee (2019). Let \hat{V}_M^k be a sample metric variance using k random samples X_1, \dots, X_k . Then $\{\hat{V}_M^n\}_{n=1}^\infty$ is a reverse martingale adapted to the σ -fields $\{\mathcal{F}_n\}_{n=1}^\infty$, where $\mathcal{F}_n = \sigma(\hat{V}_M^n, \hat{V}_M^{n+1}, \dots)$ and $\mathcal{F}_\infty = \cap_n \mathcal{F}_n$. This is because

- (a) $\{\mathcal{F}_n\}$ are decreasing sequences, i.e., $\mathcal{F}_1 \supseteq \mathcal{F}_2 \supseteq \dots \supseteq \mathcal{F}_\infty$.
- (b) \hat{V}_M^n is \mathcal{F}_n -measurable, for all $n \geq 1$.
- (c) $\mathbb{E}|\hat{V}_M^n| < \infty$, for all $n \geq 1$, under (M0).
- (d) $\mathbb{E}\{\hat{V}_M^m | \mathcal{F}_n\} = \mathbb{E}\{\mathbb{E}(\frac{1}{2}d^2(X_1, X_2) | \mathcal{F}_m) | \mathcal{F}_n\} = \mathbb{E}\{\frac{1}{2}d^2(X_1, X_2) | \mathcal{F}_n\} = \hat{V}_M^n$, for all $1 \leq m \leq n$, provided that $\hat{V}_M^n = \mathbb{E}\{\hat{V}_M^n | \mathcal{F}_n\} = \mathbb{E}\{\frac{1}{2}d^2(X_1, X_2) | \mathcal{F}_n\}$ and $\mathcal{F}_n \subseteq \mathcal{F}_m$.

Then a property of reverse martingales implies that \hat{V}_M^n converges to $\mathbb{E}\{\frac{1}{2}d^2(X_1, X_2) | \mathcal{F}_\infty\}$ almost surely (Shorack & Wellner 2009). Hence

$$\mathbb{E}\left\{\lim_{n \rightarrow \infty} \hat{V}_M^n\right\} = \mathbb{E}\left\{\mathbb{E}\left(\frac{1}{2}d^2(X_1, X_2) \middle| \mathcal{F}_\infty\right)\right\} = \mathbb{E}\left\{\frac{1}{2}d^2(X_1, X_2)\right\} = V_M.$$

Let $\mathcal{G}_n = \sigma(X_n, X_{n+1}, \dots)$ and $\mathcal{G}_\infty = \cap_n \mathcal{G}_n$, which is a tail σ -field. The Kolmogorov Zero-One law implies that \mathcal{G}_∞ -measurable functions are almost surely constant. Therefore, to establish almost surely convergence, it suffices to demonstrate that $\lim_{n \rightarrow \infty} \hat{V}_M^n$ is

\mathcal{G}_∞ -measurable, which implies that it must equal its expectation V_M . It is sufficient to show that $\lim_{n \rightarrow \infty} \hat{V}_M^n$ is \mathcal{G}_m -measurable, for arbitrary $m > 2$.

For any $n > m$, let $\mathcal{A} = \{(i, j) \mid m \leq i < j \leq n\}$, $\mathcal{B} = \{(i, j) \mid 1 \leq i < j < m\}$, and $\mathcal{C} = \{(i, j) \mid 1 \leq i < m \leq j\}$. Then

$$\hat{V}_M^n = \binom{n}{2}^{-1} A_n + \binom{n}{2}^{-1} B_n + \binom{n}{2}^{-1} C_n,$$

where $A_n = \sum_{(i,j) \in \mathcal{A}} \frac{1}{2} d^2(X_i, X_j)$, $B_n = \sum_{(i,j) \in \mathcal{B}} \frac{1}{2} d^2(X_i, X_j)$, and $C_n = \sum_{(i,j) \in \mathcal{C}} \frac{1}{2} d^2(X_i, X_j)$.

The first term $\binom{n}{2}^{-1} A_n$ is \mathcal{G}_m -measurable for all $n \geq m$, and thus $\lim_n \binom{n}{2}^{-1} A_n$ is \mathcal{G}_m -measurable. For the second term, $\lim_n \binom{n}{2}^{-1} B_n = 0$, which is \mathcal{G}_m -measurable, as B_n is constant for all $n \geq m$. Under (M0), for the third term $\binom{n}{2}^{-1} C_n = O(n^{-1})$, because

$$\begin{aligned} \binom{n}{2}^{-1} C_n &= \binom{n}{2}^{-1} \sum_{i=1}^{m-1} \sum_{j=m}^n \frac{1}{2} d^2(X_i, X_j) \\ &= \binom{n}{2}^{-1} (n - m + 1) \sum_{i=1}^{m-1} \frac{1}{n - m + 1} \sum_{j=m}^n \frac{1}{2} d^2(X_i, X_j), \end{aligned}$$

and $\frac{1}{n - m + 1} \sum_{j=m}^n \frac{1}{2} d^2(X_i, X_j) = O(1)$, given (M0). Then $\lim_n \binom{n}{2}^{-1} C_n = 0$, which is \mathcal{G}_m -measurable.

Therefore $\lim_{n \rightarrow \infty} \hat{V}_M^n$ is \mathcal{G}_∞ -measurable and by the Kolmogorov Zero-One law, \hat{V}_M^n is constant V_M with probability 1. \square

2) Proof of $\mathbb{E}|\hat{V}_M - V_M|^2 = O(n^{-1})$

By the H-decomposition in (S.21), $\hat{V}_M - V_M = 2H_n^{(1)} + H_n^{(2)}$. Therefore it is enough to show that $\mathbb{E}|H_n^{(1)}|^2$ and $\mathbb{E}|H_n^{(2)}|^2$ are of order $O(n^{-1})$, then applying the Minkowski inequality. Both $\left\{ \binom{n}{1} H_n^{(1)} \right\}_{n=1}^\infty$ and $\left\{ \binom{n}{2} H_n^{(2)} \right\}_{n=2}^\infty$ are forward martingales adapted to the σ -fields $\{\mathcal{F}_n\}_{n=1}^\infty$, where $\mathcal{F}_n = \sigma(X_1, \dots, X_n)$ and $\mathcal{F}_\infty = \bigcup_n \mathcal{F}_n$ (Lee 2019). This is because

- (a) $\{\mathcal{F}_n\}$ are increasing sequences, i.e., $\mathcal{F}_1 \subseteq \mathcal{F}_2 \subseteq \dots \subseteq \mathcal{F}_\infty$.
- (b) $\binom{n}{c} H_n^{(c)}$ is \mathcal{F}_n -measurable, for all $n \geq 1$, $c = 1, 2$.
- (c) $\mathbb{E}|\binom{n}{c} H_n^{(c)}| < \infty$, for all $n \geq 1$, $c = 1, 2$, under (M0).
- (d) Let $\mathcal{C}_1(n) = \{i : 1 \leq i \leq n\}$, and $\mathcal{C}_2(n) = \{(i, j) : 1 \leq i < j \leq n\}$. For $c = 1, 2$,

$$\mathbb{E} \left\{ \binom{n+1}{c} H_{n+1}^{(c)} \middle| \mathcal{F}_n \right\} = \sum_{\mathcal{C}_c(n+1)} \mathbb{E} \{h^{(c)}(X_{i_1}, \dots, X_{i_c}) | \mathcal{F}_n\},$$

and $\mathbb{E}\{h^{(c)}(X_{i_1}, \dots, X_{i_c}) | \mathcal{F}_n\}$ is zero if any $i_j = n+1$, and

$h^{(c)}(X_{i_1}, \dots, X_{i_c})$ otherwise. Hence

$$\mathbb{E} \left\{ \binom{n+1}{c} H_{n+1}^{(c)} \middle| \mathcal{F}_n \right\} = \sum_{\mathcal{C}_c(n)} h^{(c)}(X_{i_1}, \dots, X_{i_c}) = \binom{n}{c} H_n^{(c)}.$$

Step 1: Bound for $\mathbb{E}|H_n^{(1)}|^2$.

By Jensen's inequality,

$$\mathbb{E}|h^{(1)}(X_1)|^2 = \mathbb{E}|\mathbb{E}_{X_2|X_1}\{\psi(X_1, X_2) - V_M|X_1\}|^2 \leq \mathbb{E}|\psi(X_1, X_2) - V_M|^2 = \alpha < \infty, \quad (\text{S.23})$$

where $\alpha = \mathbb{E}|\psi(X_1, X_2) - V_M|^2$ is finite under (M1).

The martingale inequality in Dharmadhikari et al. (1968) shows that if $\{\Xi_n\}$ is a forward martingale with $\Xi_0 = 0$, then

$$\mathbb{E}|\Xi_n|^2 \leq C\beta_n n, \quad (\text{S.24})$$

where C is a constant and $\beta_n = \frac{1}{n} \sum_{j=1}^n \mathbb{E}|\Xi_j - \Xi_{j-1}|^2$.

By setting $\Xi_n = nH_n^{(1)} = \sum_{i=1}^n h^{(1)}(X_i)$ in (S.24), there exists a constant $C_1 > 0$ with

$$\mathbb{E}|nH_n^{(1)}|^2 \leq C_1 \mathbb{E}|h^{(1)}(X_1)|^2 n \leq C_1 \alpha n,$$

whence

$$\mathbb{E}|H_n^{(1)}|^2 \leq C_1 \alpha n^{-1}. \quad (\text{S.25})$$

Step 2: Bound for $\mathbb{E}|H_n^{(2)}|^2$

Since

$$\binom{n}{2} H_n^{(2)} = \sum_{j=2}^n \sum_{i=1}^{j-1} h^{(2)}(X_i, X_j) = \sum_{j=2}^n S_j,$$

where $S_j = \sum_{i=1}^{j-1} h^{(2)}(X_i, X_j)$, $j = 2, \dots, n$, applying the martingale inequality in (S.24) to $\left\{ \binom{n}{2} H_n^{(2)} \right\}_{n=2}^{\infty}$ implies that there exists a $C_2 > 0$ such that

$$\mathbb{E} \left| \binom{n}{2} H_n^{(2)} \right|^2 \leq C_2 \left(\max_{2 \leq j \leq n} \mathbb{E}|S_j|^2 \right) n. \quad (\text{S.26})$$

For a fixed $j \geq 2$, and $k = 1, \dots, j-1$, we introduce $T_{kj} = \sum_{i=1}^k h^{(2)}(X_i, X_j)$, which is a martingale adapted to $\sigma(X_1, \dots, X_k, X_j)$. By applying the martingale inequality in (S.24) to $\{T_{kj}\}$, there exists a global constant $C_3 > 0$ such that for $1 \leq j \leq n$,

$$\mathbb{E}|S_j|^2 = \mathbb{E}|T_{j-1,j}|^2 \leq C_3 \frac{1}{j-1} \sum_{k=1}^{j-1} \mathbb{E}|h^{(2)}(X_k, X_j)|^2 j = C_3 \mathbb{E}|h^{(2)}(X_1, X_2)|^2 j,$$

whence

$$\max_{2 \leq j \leq n} \mathbb{E}|S_j|^2 \leq C_3 \mathbb{E}|h^{(2)}(X_1, X_2)|^2 n, \quad (\text{S.27})$$

and by the Minkowski inequality and (S.23) there exists a constant $C_4 > 0$ such that

$$\begin{aligned} \mathbb{E}|h^{(2)}(X_1, X_2)|^2 &= \mathbb{E}|\psi(X_1, X_2) - V_M - h^{(1)}(X_1) - h^{(1)}(X_2)|^2 \\ &\leq C_4 (\mathbb{E}|\psi(X_1, X_2) - V_M|^2 + \mathbb{E}|h^{(1)}(X_1)|^2 + \mathbb{E}|h^{(1)}(X_2)|^2) \\ &\leq C_4(3\alpha). \end{aligned} \quad (\text{S.28})$$

Combining (S.26), (S.27) and (S.28), there exist a $C_5 > 0$ satisfying

$$\mathbb{E}|H_n^{(2)}|^2 \leq C_5 \alpha n^{-2}. \quad (\text{S.29})$$

By (S.25) and (S.29), we have $\mathbb{E}|H_n^{(1)}|^2 = O(n^{-1})$ and $\mathbb{E}|H_n^{(2)}|^2 = O(n^{-2})$. By applying Minkowski inequality, $\mathbb{E}|\hat{V}_M - V_M|^2 \leq \mathbb{E}|2H_n^{(1)}|^2 + \mathbb{E}|H_n^{(2)}|^2$. Thus,

$$\mathbb{E}|\hat{V}_M - V_M|^2 = O(n^{-1}).$$

□

Proof of Theorem 1

We employ the same notation for the kernel functions $\psi : \mathcal{M} \times \mathcal{M} \rightarrow \mathbb{R}$, $h^{(1)} : \mathcal{M} \rightarrow \mathbb{R}$, and $h^{(2)} : \mathcal{M} \times \mathcal{M} \rightarrow \mathbb{R}$ as defined in (S.19), (S.20) and for the H-decomposition terms $H_n^{(1)}$ and $H_n^{(2)}$ in (S.22).

Step 1: Sample metric variance \hat{V}_M

Using the decomposition in (S.21),

$$\sqrt{n}(\hat{V}_M - V_M) = \sqrt{n}(2H_n^{(1)} + H_n^{(2)}) = \frac{2}{\sqrt{n}} \sum_{i=1}^n h^{(1)}(X_i) + \sqrt{n}H_n^{(2)}.$$

The inequality (S.29) in the proof of Proposition 1 implies

$$\text{Var}(\sqrt{n}H_n^{(2)}) = O(n^{-1}). \quad (\text{S.30})$$

Since $E(\sqrt{n}H_n^{(2)}) = 0$ according to Step 3 of the proof of Proposition 1, it follows that

$$\sqrt{n}H_n^{(2)} = o_P(1).$$

Thus,

$$\sqrt{n}(\hat{V}_M - V_M) = \sqrt{n} \left(\frac{1}{n} \sum_{i=1}^n 2h^{(1)}(X_i) \right) + o_p(1).$$

Note that $\mathbb{E}(2h^{(1)}(X_1)) = 0$. Applying the CLT for i.i.d. random variables and Slutsky's Theorem leads to

$$\sqrt{n}(\hat{V}_M - V_M) \rightarrow N(0, \sigma_M^2) \quad \text{in distribution,} \quad (\text{S.31})$$

where $\sigma_M^2 = \text{var}(2h^{(1)}(X)) = \text{var}_X [\mathbb{E}_{X'|X} \{d^2(X, X')|X\}]$.

Step 2: Sample Fréchet variance \hat{V}_F

Following the proof of Theorem 1 in [Dubey & Müller \(2019\)](#),

$$\begin{aligned}\sqrt{n}(\hat{V}_F - V_F) &= \sqrt{n} \left[\frac{1}{n} \sum_{i=1}^n \{d^2(\hat{\mu}_\oplus, X_i) - d^2(\mu_\oplus, X_i)\} \right] \\ &\quad + \sqrt{n} \left[\frac{1}{n} \sum_{i=1}^n \{d^2(\mu_\oplus, X_i) - \mathbb{E}d^2(\mu_\oplus, X)\} \right].\end{aligned}$$

Under (F0)-(F2), Proposition 1 in [Dubey & Müller \(2019\)](#) shows that

$$\sqrt{n} \frac{1}{n} \sum_{i=1}^n \{d^2(\hat{\mu}_\oplus, X_i) - d^2(\mu_\oplus, X_i)\} = o_p(1).$$

Thus,

$$\sqrt{n}(\hat{V}_F - V_F) = \sqrt{n} \left[\frac{1}{n} \sum_{i=1}^n \{d^2(\mu_\oplus, X_i) - \mathbb{E}d^2(\mu_\oplus, X)\} \right] + o_p(1). \quad (\text{S.32})$$

Since $\mathbb{E}\{d^2(\mu_\oplus, X_1) - \mathbb{E}d^2(\mu_\oplus, X)\} = 0$, applying the CLT for i.i.d. random variables and Slutsky's Theorem leads to

$$\sqrt{n}(\hat{V}_F - V_F) \rightarrow N(0, \sigma_F^2) \quad \text{in distribution,} \quad (\text{S.33})$$

where $\sigma_F^2 = \text{var}(d^2(\mu_\oplus, X))$.

Step 3: Joint distribution of sample metric variance \hat{V}_M and Fréchet variance \hat{V}_F

Following [\(S.31\)](#) in *Step 1* and [\(S.33\)](#) in *Step 2*, we aim at

$$\sqrt{n} \left(\begin{pmatrix} \hat{V}_M \\ \hat{V}_F \end{pmatrix} - \begin{pmatrix} V_M \\ V_F \end{pmatrix} \right) \rightarrow N(\mathbf{0}, \Sigma) \quad \text{in distribution,}$$

where $\Sigma = \begin{pmatrix} \sigma_M^2 & \sigma_{FM} \\ \sigma_{FM} & \sigma_F^2 \end{pmatrix}$, and $\sigma_{FM} = \text{cov}(\mathbb{E}_{X'|X} \{d^2(X, X')|X\}, d^2(\mu_{\oplus}, X))$.

Applying the Cramér-Wold device, it is enough to show that for all $\mathbf{t} = (t_1, t_2)^T \in \mathbb{R}^2$,

$$\sqrt{n} \left\{ t_1 \left(\hat{V}_M - V_M \right) + t_2 \left(\hat{V}_F - V_F \right) \right\} \rightarrow N(\mathbf{0}, \mathbf{t}^T \Sigma \mathbf{t}) \quad \text{in distribution.}$$

For all $(t_1, t_2)^T \in \mathbb{R}^2$, $t_1^2 + t_2^2 > 0$,

$$\begin{aligned} & \sqrt{n} \left\{ t_1 \left(\hat{V}_M - V_M \right) + t_2 \left(\hat{V}_F - V_F \right) \right\} \\ &= \frac{1}{n} \sum_{i=1}^n [t_1 \{2h^{(1)}(X_i)\} + t_2 \{d^2(\mu_{\oplus}, X_i) - \mathbb{E}d^2(\mu_{\oplus}, X)\}] + o_p(1). \end{aligned}$$

By the CLT for i.i.d. random variables and Slutsky's Theorem,

$$\sqrt{n} \left\{ t_1 \left(\hat{V}_M - V_M \right) + t_2 \left(\hat{V}_F - V_F \right) \right\} \rightarrow N(0, \lambda^2),$$

where

$$\lambda^2 = \text{var}(t_1 \{2h^{(1)}(X_i)\} + t_2 d^2(\mu_{\oplus}, X_i)) = t_1^2 \sigma_M^2 + t_2^2 \sigma_F^2 + 2t_1 t_2 \sigma_{FM} = \mathbf{t}^T \Sigma \mathbf{t}.$$

Proof of Proposition 2

We employ the same notation for the kernel functions $\psi : \mathcal{M} \times \mathcal{M} \rightarrow \mathbb{R}$, $h^{(1)} : \mathcal{M} \rightarrow \mathbb{R}$, and $h^{(2)} : \mathcal{M} \times \mathcal{M} \rightarrow \mathbb{R}$ as defined in (S.19), (S.20) and for the H-decomposition terms $H_n^{(1)}$ and $H_n^{(2)}$ in (S.22).

Using the decomposition in (S.21),

$$\sqrt{n}(\hat{V}_M - V_M)/\sigma_M = 2\sqrt{n}H_n^{(1)}/\sigma_M + \sqrt{n}H_n^{(2)}/\sigma_M := \mathcal{H}^{(1)} + \mathcal{H}^{(2)},$$

where $\mathcal{H}^{(1)} = 2\sqrt{n}H_n^{(1)}/\sigma_M$ and $\mathcal{H}^{(2)} = \sqrt{n}H_n^{(2)}/\sigma_M$.

Under (M0)-(M3), Theorem 1 of Section 3.3.2. in Lee (2019) leads to

$$\begin{aligned} & \sup_x |\mathbb{P}(\sqrt{n}(\hat{V}_M - V_M)/\sigma_M \leq x) - \Phi(x)| \\ & \leq \left(C_1 \frac{\mathbb{E}|h^{(1)}(X_1)|^3}{\sigma_M^3} + C_2 \frac{\mathbb{E}|h^{(2)}(X_1, X_2)|^{\frac{5}{3}}}{\sigma_M^{5/3}} + C_3 \frac{\left(\mathbb{E}|h^{(1)}(X_1)|^3 \mathbb{E}|h^{(2)}(X_1, X_2)|^{\frac{3}{2}}\right)^{\frac{2}{3}}}{\sigma_M^3} \right) n^{-\frac{1}{2}}, \end{aligned}$$

for some positive constants C_1, C_2 , and C_3 . Under (M0)-(M3), the terms $\mathbb{E}|h^{(1)}(X_1)|^3$, $\mathbb{E}|h^{(2)}(X_1, X_2)|^{\frac{5}{3}}$ and $\mathbb{E}|h^{(2)}(X_1, X_2)|^{\frac{3}{2}}$ are finite. Thus,

$$\sup_x |\mathbb{P}(\sqrt{n}(\hat{V}_M - V_M)/\sigma_M \leq x) - \Phi(x)| = O(n^{-\frac{1}{2}}).$$

□

Proof of Proposition 3

1) Proof of $\hat{\sigma}_M^2 \rightarrow \sigma_M^2$ in probability

Note that

$$\hat{\sigma}_M^2 = \frac{1}{n} \sum_{i=1}^n \left\{ \frac{1}{n-1} \sum_{j \neq i}^n d^2(X_i, X_j) \right\}^2 - \left\{ \frac{2}{n(n-1)} \sum_{1 \leq i < j \leq n} d^2(X_i, X_j) \right\}^2,$$

and

$$\sigma_M^2 = \mathbb{E} [\mathbb{E}_{X'|X} \{d^2(X, X')|X\}]^2 - (\mathbb{E} d^2(X, X'))^2.$$

According to Theorem 1 and the continuous mapping theorem, the second term on the r.h.s. of $\hat{\sigma}_M^2$ converges to the second term on the r.h.s. of σ_M^2 , given by

$$\left\{ \frac{2}{n(n-1)} \sum_{1 \leq i < j \leq n} d^2(X_i, X_j) \right\}^2 = (2\hat{V}_M)^2 \rightarrow (2V_M)^2 = (\mathbb{E} d^2(X, X'))^2 \quad \text{in probability.}$$

Thus it remains to show the convergence of the first terms,

$$\frac{1}{n} \sum_{i=1}^n \left\{ \frac{1}{n-1} \sum_{j \neq i}^n d^2(X_i, X_j) \right\}^2 \rightarrow \mathbb{E}_X [\mathbb{E}_{X'|X} \{d^2(X, X')|X\}]^2 \quad \text{in probability.}$$

We decompose

$$\frac{1}{n} \sum_{i=1}^n \left(\frac{1}{n-1} \sum_{j \neq i}^n d^2(X_i, X_j) \right)^2 - \mathbb{E}_X [\mathbb{E}_{X'|X} \{d^2(X, X')|X\}]^2 = A_n + B_n, \quad (\text{S.34})$$

where $A_n = \left[\frac{1}{n} \sum_{i=1}^n \left(\frac{1}{n-1} \sum_{j \neq i}^n d^2(X_i, X_j) \right)^2 - \frac{1}{n} \sum_{i=1}^n (\mathbb{E}_{X'|X_i} \{d^2(X_i, X')|X_i\})^2 \right]$ and $B_n = \left[\frac{1}{n} \sum_{i=1}^n (\mathbb{E}_{X'|X_i} \{d^2(X_i, X')|X_i\})^2 - \mathbb{E}_X [\mathbb{E}_{X'|X} \{d^2(X, X')|X\}]^2 \right]$. Here X' is an i.i.d. copy of the X_1, \dots, X_n .

Observe that the A_n in (S.34) is

$$\begin{aligned} A_n &= \frac{1}{n} \sum_{i=1}^n \left(\frac{1}{n-1} \sum_{j \neq i}^n d^2(X_i, X_j) \right)^2 - \frac{1}{n} \sum_{i=1}^n (\mathbb{E}_{X'|X_i} \{d^2(X_i, X')|X_i\})^2 \\ &= \binom{n}{3}^{-1} \sum_{1 \leq i < j < k \leq n} d^2(X_i, X_j) d^2(X_i, X_k) \\ &\quad - \frac{1}{n} \sum_{i=1}^n \mathbb{E}_{X', X''|X_i} \{d^2(X_i, X') d^2(X_i, X'')|X_i\} + a_n, \end{aligned} \quad (\text{S.35})$$

where $a_n = \frac{1}{n(n-1)^2} \sum_{i=1}^n \sum_{j \neq i} d^4(X_i, X_j) - \binom{n}{3}^{-1} \sum_{1 \leq i < j < k \leq n} d^2(X_i, X_j) d^2(X_i, X_k)$.

By the consistency of U-statistics and the WLLN one has

$$\begin{aligned}
& \binom{n}{3}^{-1} \sum_{1 \leq i < j < k \leq n} d^2(X_i, X_j) d^2(X_i, X_k) - \frac{1}{n} \sum_{i=1}^n \mathbb{E}_{X', X'' | X_i} \{ d^2(X_i, X') d^2(X_i, X'') | X_i \} \\
&= \left[\binom{n}{3}^{-1} \sum_{1 \leq i < j < k \leq n} d^2(X_i, X_j) d^2(X_i, X_k) - \mathbb{E} (d^2(X, X') d^2(X, X'')) \right] \\
&+ \left[\mathbb{E} (d^2(X, X') d^2(X, X'')) - \frac{1}{n} \sum_{i=1}^n \mathbb{E}_{X', X'' | X_i} \{ d^2(X_i, X') d^2(X_i, X'') | X_i \} \right] = o_p(1).
\end{aligned}$$

Also, under $(M0)$,

$$\begin{aligned}
a_n &= \frac{1}{n(n-1)^2} \sum_{i=1}^n \sum_{j \neq i} d^4(X_i, X_j) \\
&- \frac{1}{(n-1)} \binom{n}{3}^{-1} \sum_{1 \leq i < j < k \leq n} d^2(X_i, X_j) d^2(X_i, X_k) = O(n^{-1}) = o_p(1).
\end{aligned}$$

Then $(S.35)$ becomes

$$A_n = \left[\frac{1}{n} \sum_{i=1}^n \left(\frac{1}{n-1} \sum_{j \neq i}^n d^2(X_i, X_j) \right)^2 - \frac{1}{n} \sum_{i=1}^n \left(\mathbb{E}_{X' | X_i} \{ d^2(X_i, X') | X_i \} \right)^2 \right] = o_p(1)$$

Applying the weak law of large number (WLLN) gives for the B_n in $(S.34)$

$$B_n = \left[\frac{1}{n} \sum_{i=1}^n \left(\mathbb{E}_{X' | X_i} \{ d^2(X_i, X') | X_i \} \right)^2 - \mathbb{E}_X \left[\mathbb{E}_{X' | X} \{ d^2(X, X') | X \} \right]^2 \right] = o_p(1). \quad (S.36)$$

Combining $(S.35)$ and $(S.36)$, $(S.34)$ becomes

$$\frac{1}{n} \sum_{i=1}^n \left\{ \frac{1}{n-1} \sum_{j \neq i}^n d^2(X_i, X_j) \right\}^2 - \mathbb{E} \left[\mathbb{E}_{X' | X} \{ d^2(X, X') | X \} \right]^2 = A_n + B_n = o_p(1).$$

Thus, $\hat{\sigma}_M^2 \rightarrow \sigma_M^2$ in probability. \square

2) Proof of $\hat{\sigma}_F^2 \rightarrow \sigma_F^2$ in probability

The consistency of $\hat{\sigma}_F^2$ was established in Proposition 2 of Dubey & Müller (2019). \square

3) Proof of $\hat{\sigma}_{FM} \rightarrow \sigma_{FM}$ in probability

Note that

$$\begin{aligned}\hat{\sigma}_{FM} &= \frac{1}{n} \sum_{i=1}^n \left[\frac{d^2(\hat{\mu}_\oplus, X_i)}{n-1} \left\{ \sum_{j \neq i}^n d^2(X_i, X_j) \right\} \right] \\ &\quad - \left\{ \frac{1}{n} \sum_{i=1}^n d^2(\hat{\mu}_\oplus, X_i) \right\} \left\{ \frac{2}{n(n-1)} \sum_{1 \leq i < j \leq n} d^2(X_i, X_j) \right\}\end{aligned}$$

and

$$\sigma_{FM} = \mathbb{E}\{d^2(\mu_\oplus, X)d^2(X, X')\} - \mathbb{E}d^2(\mu_\oplus, X)\mathbb{E}d^2(X, X').$$

By the consistency of \hat{V}_F and \hat{V}_M , the second terms converge in probability,

$$\left\{ \frac{1}{n} \sum_{i=1}^n d^2(\hat{\mu}_\oplus, X_i) \right\} \left\{ \frac{2}{n(n-1)} \sum_{1 \leq i < j \leq n} d^2(X_i, X_j) \right\} - \mathbb{E}d^2(\mu_\oplus, X)\mathbb{E}d^2(X, X') = o_p(1). \quad (\text{S.37})$$

Thus, it remains to show the convergence in probability of the first terms, given by

$$\begin{aligned} & \frac{1}{n} \sum_{i=1}^n \left[\frac{d^2(\hat{\mu}_\oplus, X_i)}{n-1} \left\{ \sum_{j \neq i}^n d^2(X_i, X_j) \right\} \right] - \mathbb{E}\{d^2(\mu_\oplus, X) d^2(X, X')\} \\ &= C_n + D_n = o_p(1), \end{aligned} \quad (\text{S.38})$$

where $C_n = \frac{1}{n} \sum_{i=1}^n \left[\frac{d^2(\hat{\mu}_\oplus, X_i)}{n-1} \left\{ \sum_{j \neq i}^n d^2(X_i, X_j) \right\} \right] - \frac{1}{n} \sum_{i=1}^n \left[\frac{d^2(\mu_\oplus, X_i)}{n-1} \left\{ \sum_{j \neq i}^n d^2(X_i, X_j) \right\} \right]$, and $D_n = \frac{1}{n} \sum_{i=1}^n \left[\frac{d^2(\mu_\oplus, X_i)}{n-1} \left\{ \sum_{j \neq i}^n d^2(X_i, X_j) \right\} \right] - \mathbb{E}\{d^2(\mu_\oplus, X) d^2(X, X')\}$.

Under (F1), Theorem 1 of Petersen & Müller (2019) leads to $d(\hat{\mu}_\oplus, \mu_\oplus) = o_p(1)$, whence

$$\begin{aligned} |C_n| &= \left| \frac{1}{n} \sum_{i=1}^n \left[\frac{d^2(\hat{\mu}_\oplus, X_i)}{n-1} \left\{ \sum_{j \neq i}^n d^2(X_i, X_j) \right\} \right] - \frac{1}{n} \sum_{i=1}^n \left[\frac{d^2(\mu_\oplus, X_i)}{n-1} \left\{ \sum_{j \neq i}^n d^2(X_i, X_j) \right\} \right] \right| \\ &= \left| \frac{1}{n} \sum_{i=1}^n \left[\frac{d^2(\hat{\mu}_\oplus, X_i) - d^2(\mu_\oplus, X_i)}{n-1} \left\{ \sum_{j \neq i}^n d^2(X_i, X_j) \right\} \right] \right| \\ &\leq 2\text{diam}(\mathcal{M}) \frac{d(\hat{\mu}_\oplus, \mu_\oplus)}{n(n-1)} \sum_{i=1}^n \sum_{j \neq i}^n d^2(X_i, X_j) = o_p(1), \end{aligned}$$

because $\frac{1}{n(n-1)} \sum_{i=1}^n \sum_{j \neq i}^n d^2(X_i, X_j) = O(1)$ under (F0). Also, the first term of D_n in (S.38) is represented as

$$\begin{aligned} & \frac{1}{n} \sum_{i=1}^n \left[\frac{d^2(\mu_\oplus, X_i)}{n-1} \left\{ \sum_{j \neq i}^n d^2(X_i, X_j) \right\} \right] \\ &= \frac{1}{n(n-1)} \sum_{i=1}^n \sum_{j \neq i}^n \left[\left\{ \frac{d^2(\mu_\oplus, X_i) + d^2(\mu_\oplus, X_j)}{2} \right\} d^2(X_i, X_j) \right], \end{aligned}$$

which is the U-statistic with the kernel $\phi(x, y) = \left\{ \frac{d^2(\mu_\oplus, x) + d^2(\mu_\oplus, y)}{2} \right\} d^2(x, y)$. The mean of this U-statistic is

$$\mathbb{E} \left\{ \frac{d^2(\mu_\oplus, X)}{2} d^2(X, X') \right\} + \mathbb{E} \left\{ \frac{d^2(\mu_\oplus, X')}{2} d^2(X, X') \right\} = \mathbb{E}\{d^2(\mu_\oplus, X) d^2(X, X')\}.$$

Then by the consistency of U-statistics,

$$D_n = \frac{1}{n} \sum_{i=1}^n \left[\frac{d^2(\mu_{\oplus}, X_i)}{n-1} \left\{ \sum_{j \neq i}^n d^2(X_i, X_j) \right\} \right] - \mathbb{E}\{d^2(X, X') d^2(\mu_{\oplus}, X)\} = o_p(1).$$

Thus, by combining (S.37) and (S.38), $\hat{\sigma}_{FM}^2 \rightarrow \sigma_{FM}^2$ in probability. \square

Lemma 1 (Aleksandrov 1951) *Let κ be a real number. For all vertices a, b, c on the space (\mathcal{M}, d) , satisfying $d(a, b) + d(a, c) + d(b, c) < 2D_{\kappa}$, where $D_{\kappa} = \infty$ for $\kappa \leq 0$, and $D_{\kappa} = \frac{\pi}{\sqrt{\kappa}}$ for $\kappa > 0$, there exists points \tilde{a}, \tilde{b} , and \tilde{c} on model space $(\mathcal{M}_{\kappa}, d_{\kappa})$ such that $d(a, b) = d_{\kappa}(\tilde{a}, \tilde{b})$, $d(b, c) = d_{\kappa}(\tilde{b}, \tilde{c})$, and $d(a, c) = d_{\kappa}(\tilde{a}, \tilde{c})$.*

For a more detailed explanation, see Lemma 2.14 in Chapter I.2 of Bridson & Haefliger (2013).

Proof of Theorem 2

We first define an (Alexandrov) angle between two geodesics γ_1 and γ_2 emanating from a in a geodesic space (\mathcal{M}, d) as

$$\angle_a(\gamma_1, \gamma_2) = \limsup_{s, t \rightarrow 0} \bar{\angle}_a(\gamma_1(s), \gamma_2(t)),$$

where the comparison angle between b and c at a is $\bar{\angle}_a(b, c) = \arccos \frac{d^2(a, b) + d^2(a, c) - d^2(b, c)}{2d(a, b)d(a, c)}$.

For a uniquely geodesic space (\mathcal{M}, d) , $\angle_a(\gamma_1, \gamma_2)$ does not depend on the lengths of γ_1 or γ_2 . For $a, b, c \in \mathcal{M}$, we can define the angle $\angle_a(b, c) = \angle_a(\gamma_{ab}, \gamma_{ac})$.

By Lemma 1 and properties of bounded curvature spaces (see, e.g., Proposition 1.7 in Chapter II.1 of Bridson & Haefliger (2013) or Section 2 in Lin & Müller (2021)), if the

curvature of (\mathcal{M}, d) is upper (lower, respectively) bounded by κ , for vertices $a, b, c \in (\mathcal{M}, d)$ satisfying $d(a, b) + d(a, c) + d(b, c) < 2D_\kappa$, there exist points $\tilde{a}, \tilde{b}, \tilde{c} \in (\mathcal{M}_\kappa, d_\kappa)$ such that $d(a, b) = d_\kappa(\tilde{a}, \tilde{b})$, $d(a, c) = d_\kappa(\tilde{a}, \tilde{c})$, and $\angle_a(b, c) = \angle_{\tilde{a}}(\tilde{b}, \tilde{c})$, and $d(b, c) \geq d_\kappa(\tilde{b}, \tilde{c})$ ($d(b, c) \leq d_\kappa(\tilde{b}, \tilde{c})$, respectively). Also, under the conditions of Theorem 2, the metric space \mathcal{M} is a unique geodesic space (Sturm 2003) and has curvature upper bounded by 0.

Then for $a = \mu_\oplus$, $b = X$, and $c = X'$, we have

$$d(X, X') \geq d_0(\tilde{X}, \tilde{X}'),$$

where $\tilde{\mu}_\oplus, \tilde{X}, \tilde{X}' \in (\mathcal{M}_0, d_0)$, form a comparison triangle on the Euclidean space such that $d(\mu_\oplus, X) = d_0(\tilde{\mu}_\oplus, \tilde{X})$, $d(\mu_\oplus, X') = d_0(\tilde{\mu}_\oplus, \tilde{X}')$, and $\angle_{\mu_\oplus}(X, X') = \angle_{\tilde{\mu}_\oplus}(\tilde{X}, \tilde{X}')$. When \mathcal{M} is a curved space, one may have $\mathbb{E}\tilde{X} \neq \tilde{\mu}_\oplus$.

By the law of cosines on the Euclidean space,

$$\begin{aligned} d^2(X, X') &\geq d_0^2(\tilde{X}, \tilde{X}') \\ &= d_0^2(\tilde{\mu}_\oplus, \tilde{X}) + d_0^2(\tilde{\mu}_\oplus, \tilde{X}') - 2d_0(\tilde{\mu}_\oplus, \tilde{X})d_0(\tilde{\mu}_\oplus, \tilde{X}') \cos \angle_{\tilde{\mu}_\oplus}(\tilde{X}, \tilde{X}') \quad (\text{S.39}) \\ &= d^2(\mu_\oplus, X) + d^2(\mu_\oplus, X') - 2d(\mu_\oplus, X)d(\mu_\oplus, X') \cos \angle_{\mu_\oplus}(X, X'). \end{aligned}$$

The expectation of the cross-product term in (S.39) is given by

$$\begin{aligned} \mathbb{E} [d(\mu_\oplus, X)d(\mu_\oplus, X') \cos \angle_{\mu_\oplus}(X, X')] \\ = \mathbb{E}_{X'} [d(\mu_\oplus, X') \mathbb{E}_{X|X'} \{d(\mu_\oplus, X) \cos \angle_{\mu_\oplus}(X, X')\}] \quad (\text{S.40}) \end{aligned}$$

By Lemma S.7. in Lin & Müller (2021),

$$\mathbb{E} \{d(\mu_\oplus, X) \cos \angle_{\mu_\oplus}(X, \xi)\} \leq 0$$

for $\xi \in \mathcal{M}$. Then since $d(\cdot, \cdot) \geq 0$, for the term in (S.40)

$$\mathbb{E} [d(\mu_{\oplus}, X)d(\mu_{\oplus}, X') \cos_{\mu_{\oplus}}(X, X')] \leq 0. \quad (\text{S.41})$$

Taking expectations in (S.39),

$$\begin{aligned} 2V_M &= \mathbb{E}d^2(X, X') \\ &\geq \mathbb{E}d^2(\mu_{\oplus}, X) + \mathbb{E}d^2(\mu_{\oplus}, X') - 2\mathbb{E}d(\mu_{\oplus}, X)d(\mu_{\oplus}, X') \cos \angle_{\mu_{\oplus}}(X, X') \\ &= 2V_F - 2\mathbb{E}d(\mu_{\oplus}, X)d(\mu_{\oplus}, X') \cos \angle_{\mu_{\oplus}}(X, X') \\ &\geq 2V_F. \end{aligned}$$

The last inequality is implied by (S.41). Thus, $V_M \geq V_F$.

If (\mathcal{M}, d) is a space with *strictly negative curvature* satisfying the conditions of Theorem 2, we can find $\delta < 0$ such that (\mathcal{M}, d) is upper bounded by δ . Then for $a = \mu_{\oplus}$, $b = X$ and $c = X'$,

$$d(X, X') \geq d_{\delta}(\check{X}, \check{X}') > d_0(\tilde{X}, \tilde{X}'),$$

where $\check{\mu}_{\oplus}, \check{X}, \check{X}' \in (\mathcal{M}_{\delta}, d_{\delta})$ and $\tilde{\mu}_{\oplus}, \tilde{X}, \tilde{X}' \in (\mathcal{M}_0, d_0)$ such that $d(\mu_{\oplus}, X) = d_{\delta}(\check{\mu}_{\oplus}, \check{X}) = d_0(\tilde{\mu}_{\oplus}, \tilde{X})$, $d(\mu_{\oplus}, X') = d_{\delta}(\check{\mu}_{\oplus}, \check{X}') = d_0(\tilde{\mu}_{\oplus}, \tilde{X}')$ and $\angle_{\mu_{\oplus}}(X, X') = \angle_{\check{\mu}_{\oplus}}(\check{X}, \check{X}') = \angle_{\tilde{\mu}_{\oplus}}(\tilde{X}, \tilde{X}')$. Following the same argument as above,

$$d^2(X, X') > d^2(\mu_{\oplus}, X) + d^2(\mu_{\oplus}, X') - 2d(\mu_{\oplus}, X)d(\mu_{\oplus}, X') \cos \angle_{\mu_{\oplus}}(X, X').$$

Finally, under the condition (S1),

$$2V_M > 2V_F - 2\mathbb{E}_{X'} [d(\mu_{\oplus}, X')\mathbb{E}_{X|X'} \{d(\mu_{\oplus}, X) \cos \angle_{\mu_{\oplus}}(X, X')\}] \geq 2V_F.$$

Thus, $V_M > V_F$. □

Proof of Theorem 3

We follow the proof of Theorem 2. Under the conditions of Theorem 3, the unique geodesic metric space \mathcal{M} has curvature lower bounded by 0. Then by Lemma 1 and properties of bounded curvature space (e.g., Proposition 1.7 in Chapter II.1 of [Bridson & Haefliger \(2013\)](#) or Section 2 in [Lin & Müller \(2021\)](#)), for $a = \mu_{\oplus}$, $b = X$ and $c = X'$,

$$d(X, X') \leq d_0(\tilde{X}, \tilde{X}'),$$

where $\tilde{\mu}_{\oplus}, \tilde{X}, \tilde{X}' \in (\mathcal{M}_0, d_0)$, form a comparison triangle on the Euclidean space such that $d(\mu_{\oplus}, X) = d_0(\tilde{\mu}_{\oplus}, \tilde{X})$, $d(\mu_{\oplus}, X') = d_0(\tilde{\mu}_{\oplus}, \tilde{X}')$, and $\angle_{\mu_{\oplus}}(X, X') = \angle_{\tilde{\mu}_{\oplus}}(\tilde{X}, \tilde{X}')$.

By the law of cosines on the Euclidean space,

$$\begin{aligned} d^2(X, X') &\leq d_0^2(\tilde{X}, \tilde{X}') \\ &= d_0^2(\tilde{\mu}_{\oplus}, \tilde{X}) + d_0^2(\tilde{\mu}_{\oplus}, \tilde{X}') - 2d_0(\tilde{\mu}_{\oplus}, \tilde{X})d_0(\tilde{\mu}_{\oplus}, \tilde{X}') \cos \angle_{\tilde{\mu}_{\oplus}}(\tilde{X}, \tilde{X}') \quad (\text{S.42}) \\ &= d^2(\mu_{\oplus}, X) + d^2(\mu_{\oplus}, X') - 2d(\mu_{\oplus}, X)d(\mu_{\oplus}, X') \cos \angle_{\mu_{\oplus}}(X, X'). \end{aligned}$$

The expectation of the cross-product term in (S.42) is given by

$$\begin{aligned}
& \mathbb{E} [d(\mu_{\oplus}, X) d(\mu_{\oplus}, X') \cos_{\mu_{\oplus}}(X, X')] \\
&= \mathbb{E} \left[d_0(\tilde{\mu}_{\oplus}, \tilde{X}) d_0(\tilde{\mu}_{\oplus}, \tilde{X}') \cos \angle_{\tilde{\mu}_{\oplus}}(\tilde{X}, \tilde{X}') \right] = \mathbb{E} \langle \tilde{X} - \tilde{\mu}_{\oplus}, \tilde{X}' - \tilde{\mu}_{\oplus} \rangle \\
&= \mathbb{E} \langle (\tilde{X} - \mathbb{E} \tilde{X}) + (\mathbb{E} \tilde{X} - \tilde{\mu}_{\oplus}), (\tilde{X}' - \mathbb{E} \tilde{X}') + (\mathbb{E} \tilde{X}' - \tilde{\mu}_{\oplus}) \rangle \\
&= (\mathbb{E} \tilde{X} - \tilde{\mu}_{\oplus})^2 \geq 0,
\end{aligned} \tag{S.43}$$

where $\langle \cdot, \cdot \rangle$ is the inner product in Euclidean space (\mathcal{M}_0, d_0) . Taking expectations in (S.42),

$$\begin{aligned}
2V_M &= \mathbb{E} d^2(X, X') \\
&\leq \mathbb{E} d^2(\mu_{\oplus}, X) + \mathbb{E} d^2(\mu_{\oplus}, X') - 2\mathbb{E} d(\mu_{\oplus}, X) d(\mu_{\oplus}, X') \cos \angle_{\mu_{\oplus}}(X, X') \\
&= 2V_F - 2\mathbb{E} d(\mu_{\oplus}, X) d(\mu_{\oplus}, X') \cos \angle_{\mu_{\oplus}}(X, X') \\
&\leq 2V_F.
\end{aligned}$$

The last inequality is implied by (S.43). Thus, $V_M \leq V_F$.

If (\mathcal{M}, d) is a *strictly positive curvature* space satisfying the conditions of Theorem 3, we can find $\epsilon > 0$ such that (\mathcal{M}, d) is lower bounded by ϵ . Then for $a = \mu_{\oplus}$, $b = X$ and $c = X'$,

$$d(X, X') \leq d_{\epsilon}(\check{X}, \check{X}') < d_0(\tilde{X}, \tilde{X}'),$$

where $\check{\mu}_{\oplus}, \check{X}, \check{X}' \in (\mathcal{M}_{\epsilon}, d_{\epsilon})$ and $\tilde{\mu}_{\oplus}, \tilde{X}, \tilde{X}' \in (\mathcal{M}_0, d_0)$ such that $d(\mu_{\oplus}, X) = d_{\epsilon}(\check{\mu}_{\oplus}, \check{X}) = d_0(\tilde{\mu}_{\oplus}, \tilde{X})$, $d(\mu_{\oplus}, X') = d_{\epsilon}(\check{\mu}_{\oplus}, \check{X}') = d_0(\tilde{\mu}_{\oplus}, \tilde{X}')$ and $\angle_{\mu_{\oplus}}(X, X') = \angle_{\check{\mu}_{\oplus}}(\check{X}, \check{X}') = \angle_{\tilde{\mu}_{\oplus}}(\tilde{X}, \tilde{X}')$. Following the same argument above,

$$d^2(X, X') < d^2(\mu_{\oplus}, X) + d^2(\mu_{\oplus}, X') - 2d(\mu_{\oplus}, X) d(\mu_{\oplus}, X') \cos \angle_{\mu_{\oplus}}(X, X').$$

Finally, under the condition (S1),

$$2V_M < 2V_F - 2\mathbb{E}_{X'} [d(\mu_{\oplus}, X')\mathbb{E}_{X|X'} \{d(\mu_{\oplus}, X) \cos \angle_{\mu_{\oplus}}(X, X')\}] \leq 2V_F.$$

Thus, $V_M < V_F$. □

Proof of Theorem 4

Observing

$$\hat{\rho} = g(\hat{V}_M, \hat{V}_F),$$

where $g(x_1, x_2) = \frac{x_2}{x_1} - 1$ is a differentiable function with gradient function $\nabla g = (-\frac{x_2}{x_1^2}, \frac{1}{x_1})^T$, a simple application of the δ -method establishes the asymptotic normality of $\hat{\rho}$, given by

$$\sqrt{n}(\hat{\rho} - \rho) \rightarrow N(0, \sigma^2) \quad \text{in distribution,}$$

where the asymptotic variance is $\sigma^2 = a^T \Sigma a$ and a is the gradient function ∇g evaluated at (V_M, V_F) .

Proposition 3 leads to a consistent estimator for σ^2 , given by

$$\hat{\sigma}^2 = \hat{a}^T \hat{\Sigma} \hat{a},$$

where $\hat{a} = \left(-\frac{\hat{V}_F}{\hat{V}_M^2}, \frac{1}{\hat{V}_M}\right)^T$ and the estimated asymptotic covariance matrix is

$$\hat{\Sigma} = \begin{pmatrix} \hat{\sigma}_M^2 & \hat{\sigma}_{MF} \\ \hat{\sigma}_{FM} & \hat{\sigma}_F^2 \end{pmatrix}.$$

By consistency of asymptotic variance $\hat{\sigma}^2$, we obtain the asymptotic normality

$$\sqrt{n}(\hat{\rho} - \rho)/\hat{\sigma} \rightarrow N(0, 1) \quad \text{in distribution.}$$

Thus, under $H_0 : \rho = 0$, $T_n \rightarrow N(0, 1)$ in distribution. \square

Proof of Theorem 5

Following the same argument in case of the sample Fréchet mean $\hat{\mu}_\oplus$, under the conditions (A0)-(A4), the sample intrinsic Fréchet mean $\hat{\mu}_{I,\oplus}$ is consistent for the population intrinsic Fréchet mean $\mu_{I,\oplus}$ (Theorem 1 of Petersen & Müller (2019)). Under conditions (A0)-(A4), Theorem 1 leads to

$$\sqrt{n} \left((\hat{V}_{I,M}, \hat{V}_{I,F})^T - (V_{I,M}, V_{I,F})^T \right) \rightarrow N(\mathbf{0}, \Sigma_I) \quad \text{in distribution,}$$

where $\Sigma_I = \begin{pmatrix} \sigma_{I,M}^2 & \sigma_{I,FM} \\ \sigma_{I,FM} & \sigma_{I,F}^2 \end{pmatrix}$. Theorem 4 can then be directly applied under conditions (A0)-(A4), we have

$$\sqrt{n}(\hat{\rho}_I - \rho_I)/\hat{\sigma}_I \rightarrow N(0, 1) \quad \text{in distribution.}$$

Thus, under $H_0 : \rho_I = 0$, $T_{I,n} \rightarrow N(0, 1)$ in distribution. \square

Proof of Theorem S.1

Following Corollary 2.1 of Aaron & Bodart (2018), under conditions (B1)-(B2), if the weighted graph in Algorithm 1 is constructed using a ball size $r = r_n$ such that

$$\left(A_0 \frac{\log n}{n} \right)^{2/3k} \leq r_n \leq \left(A_1 \frac{\log n}{n} \right)^{2/3k},$$

for some $A_0, A_1 > 0$, it holds that

$$\max_{i,j} \left| \hat{d}_I(X_i, X_j) - d_I(X_i, X_j) \right| = O \left(\left(\frac{\log n}{n} \right)^{2/3k} \right). \quad (\text{S.44})$$

By definition,

$$\rho_I = \frac{V_{I,F}}{V_{I,M}} - 1, \quad \hat{\rho}_I = \frac{\hat{V}_{I,F}}{\hat{V}_{I,M}} - 1, \quad \text{and} \quad \tilde{\rho}_{I,n} = \frac{\tilde{V}_{I,F}}{\tilde{V}_{I,M}} - 1,$$

where $V_{I,F} = \mathbb{E} d_I^2(\mu_{I,\oplus}, X)$, $\hat{V}_{I,F} = \frac{1}{n} \sum_{i=1}^n d_I^2(\hat{\mu}_{I,\oplus}, X_i)$, $\tilde{V}_{I,F} = \frac{1}{n} \sum_{i=1}^n \hat{d}_I^2(\hat{\mu}_{I,\oplus}, X_i)$, $V_{I,M} = \frac{1}{2} \mathbb{E} d_I^2(X, X')$, $\hat{V}_{I,M} = \frac{1}{n(n-1)} \sum_{1 \leq i < j \leq n} d_I^2(X_i, X_j)$ and $\tilde{V}_{I,M} = \frac{1}{n(n-1)} \sum_{1 \leq i < j \leq n} \hat{d}_I^2(X_i, X_j)$.

In the following, the notation \lesssim refers to an inequality modulo a multiplicative constant.

We observe

$$\begin{aligned} |\tilde{V}_{I,F} - \hat{V}_{I,F}| &\leq \frac{1}{n} \sum_{i=1}^n |\hat{d}_I(\hat{\mu}_{I,\oplus}, X_i) - d_I(\hat{\mu}_{I,\oplus}, X_i)| |\hat{d}_I(\hat{\mu}_{I,\oplus}, X_i) + d_I(\hat{\mu}_{I,\oplus}, X_i)| \\ &\lesssim \frac{1}{n} \sum_{i=1}^n |\hat{d}_I(\hat{\mu}_{I,\oplus}, X_i) - d_I(\hat{\mu}_{I,\oplus}, X_i)| = O \left(\left(\frac{\log n}{n} \right)^{2/3k} \right), \end{aligned}$$

where the second \lesssim follows from the boundedness of \mathcal{A} , the uniform convergence of

$\max_{i,j} \left| \hat{d}_I(X_i, X_j) - d_I(X_i, X_j) \right|$ and the fact that $\hat{\mu}_{\oplus} \in \mathcal{X}_n := \{X_1, \dots, X_n\}$. The last equality is a consequence of (S.44). Similarly,

$$\begin{aligned} |\tilde{V}_{I,M} - \hat{V}_{I,M}| &\leq \frac{1}{n(n-1)} \sum_{1 \leq i < j \leq n} |\hat{d}_I(X_i, X_j) - d_I(X_i, X_j)| |\hat{d}_I(X_i, X_j) + d_I(X_i, X_j)| \\ &\lesssim \frac{1}{n(n-1)} \sum_{1 \leq i < j \leq n} |\hat{d}_I(X_i, X_j) - d_I(X_i, X_j)| = O \left(\left(\frac{\log n}{n} \right)^{2/3k} \right). \end{aligned}$$

Additionally,

$$\hat{V}_{I,F} = O(1) \quad \text{a.s.} \quad \text{and} \quad \hat{V}_{I,M} = O(1) \quad \text{a.s.}$$

Next,

$$|\tilde{\rho}_{I,n} - \rho_{I,n}| \leq |\tilde{\rho}_{I,n} - \hat{\rho}_{I,n}| + |\hat{\rho}_{I,n} - \rho_{I,n}|.$$

For the first term $\tilde{\rho}_{I,n} - \hat{\rho}_{I,n}$, we have

$$\begin{aligned} |\tilde{\rho}_{I,n} - \hat{\rho}_{I,n}| &= \left| \frac{\tilde{V}_{I,F}}{\tilde{V}_{I,M}} - \frac{\hat{V}_{I,F}}{\hat{V}_{I,M}} \right| \\ &= \left| \frac{(\tilde{V}_{I,F} - \hat{V}_{I,F})\hat{V}_{I,M} - (\tilde{V}_{I,M} - \hat{V}_{I,M})\hat{V}_{I,F}}{(\tilde{V}_{I,M} - \hat{V}_{I,M})\hat{V}_{I,M} + \hat{V}_{I,M}^2} \right| \\ &\lesssim |(\tilde{V}_{I,F} - \hat{V}_{I,F})\hat{V}_{I,M} - (\tilde{V}_{I,M} - \hat{V}_{I,M})\hat{V}_{I,F}| \\ &\leq |(\tilde{V}_{I,F} - \hat{V}_{I,F})\hat{V}_{I,M}| + |(\tilde{V}_{I,M} - \hat{V}_{I,M})\hat{V}_{I,F}| \\ &= O\left(\left(\frac{\log n}{n}\right)^{2/3k}\right). \end{aligned}$$

By Theorem 5, we can obtain the convergence rate of the second term

$$|\hat{\rho}_{I,n} - \rho_{I,n}| = O(n^{-1/2}) \quad \text{a.s.}$$

and thus

$$|\tilde{\rho}_{I,n} - \rho_{I,n}| \leq |\tilde{\rho}_{I,n} - \hat{\rho}_{I,n}| + |\hat{\rho}_{I,n} - \rho_{I,n}| = O\left(\max\left\{\left(\frac{\log n}{n}\right)^{2/3k}, \left(\frac{1}{n}\right)^{1/2}\right\}\right) \quad \text{a.s.}$$

Proof of Corollary S.1

The result is a direct consequence of Corollary 2.2 of Aaron & Bodart (2018) and Theorem S.1.

S.5 Verification of conditions for simulations and real data analysis

1. **Example 1 (Section 5.1):** We consider a subset of the bivariate Wasserstein space, $\mathcal{D} \subset \mathcal{W}_2(\mathbb{R}^2)$, for

$$\mathcal{D} = \left\{ N(0, \Lambda(\theta)) \mid \Lambda(\theta) = R(\theta) \Lambda_0 R(\theta)^T \in \mathbb{R}^{2 \times 2}, \theta \in [0, 1] \right\},$$

with a rotation matrix $R(\theta) = \begin{pmatrix} \cos(\frac{\pi}{2}\theta) & -\sin(\frac{\pi}{2}\theta) \\ \sin(\frac{\pi}{2}\theta) & \cos(\frac{\pi}{2}\theta) \end{pmatrix}$ and $\Lambda_0 = \text{diag}(\lambda_1, \lambda_2)$, where $\lambda_1 = 4$ and $\lambda_2 = 1$. Specifically, the space \mathcal{D} forms a location-scatter family, as defined by [Ahidar-Coutrix et al. \(2020\)](#). This follows from the fact that \mathcal{D} is a subset of the multivariate mean zero Gaussian distribution space with covariance matrices constrained by bounded eigenvalues. Formally,

$$\mathcal{D} \subset \left\{ N_p(0, \Lambda) \mid \lambda_1 I_p \leq \Lambda \leq \lambda_2 I_p \right\},$$

where $\lambda_1 = 1$, $\lambda_2 = 4$, and $p = 2$.

We first show condition (F2). Example 2.4 in [Ahidar-Coutrix et al. \(2020\)](#) implies that $N\left(\frac{\delta\epsilon}{2}, B_\delta(\xi), d\right) \leq (\frac{C}{\epsilon})^D$, for a constant $C >$, and $D = p + p(p + 1)/2$, where $p = 2$ in the bivariate case we consider here. Then

$$\begin{aligned} \int_0^1 \sqrt{1 + \log N(\delta\epsilon/2, B_\delta(\xi), d)} d\epsilon &\leq \int_0^1 \sqrt{1 + D \log C - D \log \epsilon} d\epsilon \\ &\leq 1 + D \log C + \sqrt{D} \int_0^1 \sqrt{-\log \epsilon} d\epsilon \\ &\leq 1 + D \log C + \sqrt{D} \int_1^\infty \sqrt{y} \exp(-y) dy < \infty. \end{aligned}$$

The second inequality comes from $\sqrt{a+x} \leq a + \sqrt{x}$, for $a \geq 1$, and $x > 0$. The third inequality is obtained by substituting $y = -\log \epsilon$. Then

$$\delta \int_0^1 \sqrt{1 + \log N(\delta\epsilon/2, B_\delta(\xi), d)} d\epsilon \rightarrow 0 \text{ as } \delta \rightarrow 0.$$

The total boundedness condition *(F0)* holds because \mathcal{D} is closed and bounded with respect to the metric, and it is a subset of a D -dimensional Euclidean space (Ahidar-Coutrix et al. 2020). By the Heine-Borel theorem, \mathcal{D} is compact, hence totally bounded. The uniqueness of the population Fréchet mean *(F1)* is established by Le Gouic & Loubes (2017).

For assumptions *(M0)*-*(M3)*, we consider a continuous distribution over \mathcal{D} that has no atoms. The left hand inequalities in *(M0)* and *(M2)* correspond to

$$\mathbb{E}d^2(X, X') > 0, \text{ and } \text{Var}_X [\mathbb{E}_{X'|X} \{d^2(X, X')|X\}] > 0.$$

Additionally, the total boundedness in *(F0)* ensures boundedness, which guarantees the right hand inequality in *(M0)*, i.e., $\mathbb{E}d^2(X, X') < \infty$, as well as the inequalities in *(M1)* and *(M3)*, $\mathbb{E}d^4(X, X') < \infty$ and $\mathbb{E}_X |\mathbb{E}_{X|X'} \{d^2(X, X')|X\}|^3 < \infty$, for i.i.d. random objects $X, X' \in \mathcal{M}$.

The intrinsic space (\mathcal{D}, d_I) here is a one-dimensional compact manifold that is smooth with boundary, such as a closed interval $[m, M] \in \mathbb{R}$. This is because the space depends only on the one-dimensional normalized rotation angle $\theta \in [0, 1]$. Figure S.6 provides empirical evidence, showing that the representation of random distributions X_1, \dots, X_{100} aligns with a one-dimensional structure proportional to the angle θ . This one-dimensional compact manifold with boundary satisfies assumptions *(A0)* through *(A4)*.

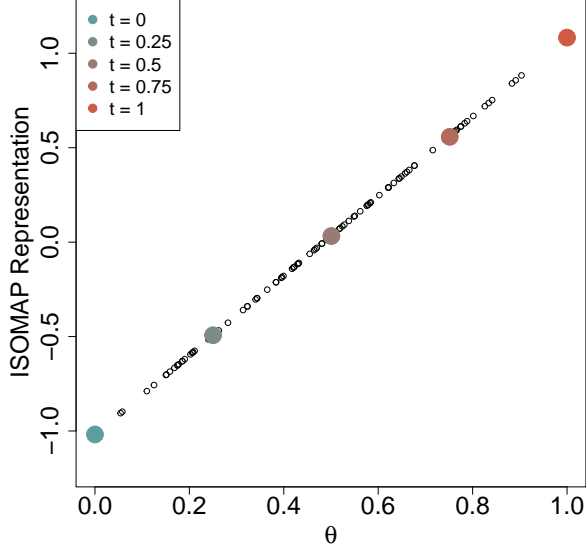


Figure S.6: ISOMAP representation interpolation $s(t) = (1 - t)\hat{\psi}(x) + t\hat{\psi}(y)$, where $\hat{\psi} : \mathcal{D} \rightarrow \mathbb{R}^k$ is the representation map of ISOMAP, obtained by random bivariate normal distributions, X_1, \dots, X_{100} (black dots), generated from the intrinsic space \mathcal{D} as a function of the normalized rotation angle $0 \leq \theta \leq 1$.

2. Gait Synchronization Analysis (Section 6.1): In this real data analysis, the gait synchronization data are represented as a sample of 2×2 symmetric positive definite (SPD) matrices, equipped with the Bures-Wasserstein metric, which defines the ambient metric space. Under the assumption of bounded eigenvalues of the SPD space, this space has the same geometric structure as the space of mean-zero bivariate Gaussian distributions equipped with the 2-Wasserstein metric (Bhatia et al. 2019). Accordingly, the same arguments as in the previous subsection can be applied to verify assumptions $(F0) - (F2)$, $(M0) - (M3)$, and $(A0) - (A4)$.

3. Example 2 (Section 5.2):

Based on the generation of random samples in each space \mathcal{B}_1 , \mathcal{B}_2 \mathcal{B}_3 , the assumptions of strictly positiveness $(A0)$, non-zero metric variance V_M , and non-degenerate asymptotic variance $(A4)$ hold. For $(A1)$, the space \mathcal{B}_1 is a closed upper hemisphere of radius 1, making

it a compact Euclidean rectangle with uniform distribution, which is also totally bounded.

While hyperbolic spaces are not generally bounded, imposing the constraint $0 \leq z \leq 4$ ensures boundedness. This is because for any $X_a = (x_a, y_a, z_a)$ and $X_b = (x_b, y_b, z_b)$ in \mathcal{B}_3 , defining $X_0 = (0, 0, 1)$, the hyperbolic geodesic distance satisfies:

$$\begin{aligned} d_{\text{hyper}}(X_a, X_b) &\leq d_{\text{hyper}}(X_a, X_0) + d_{\text{hyper}}(X_b, X_0) \\ &= \text{arccosh}(z_a) + \text{arccosh}(z_b) \\ &\leq 2 \log(4 + \sqrt{15}) < \infty. \end{aligned}$$

The space \mathcal{B}_3 is closed and forms a subset of the 3-dimensional Euclidean space. By the Heine-Borel theorem, it is compact, which implies total boundedness.

For (A2), it is easy to see that the Fréchet mean of \mathcal{B}_1 and of \mathcal{B}_2 is $(0, 0, 1)$ and the Fréchet mean of \mathcal{B}_3 is $(1/2, 1/2, 0)$. Then (A3) is satisfied based on Proposition 3 in the supplementary materials of [Petersen & Müller \(2019\)](#), which shows that a bounded Riemannian manifold of finite dimension r equipped with the geodesic distance satisfies the entropy condition

$$\int_0^1 \sqrt{1 + \log N(\delta\epsilon/2, B_\delta(\xi), d)} d\epsilon = O(1)$$

as $\delta \rightarrow 0$.

In real-world scenarios, data can often be contaminated with noise, which may cause certain assumptions to be violated depending on the noise structure. We consider error-contaminated settings with relatively small noise to assess the robustness of our test, and our simulation results show that our method can still detect the intrinsic positive, flat, and negative curvature even in the presence of noise.

4. **Energy data (Section 6.2):** The second real data analysis, which uses energy data, considers random objects on the positive quadrant of the intrinsic spherical space \mathbb{S}_+^2 , equipped with the geodesic distance. The ambient space is the 3-dimensional Euclidean space. This setting aligns with \mathcal{B}_1 in Example 2, as discussed in the previous paragraph, and the same arguments apply to verify the assumptions.

S.6 Sensitivity analysis for the choice of input distance d

The selection of an appropriate metric d is an important and open research question that has received limited attention. Recent discussion on this topic can be found in Section 8 of [Dubey et al. \(2024\)](#). In cases where data lie on Riemannian manifolds embedded in Euclidean ambient spaces, such as spheres or hyperbolic spaces, the Euclidean distance is commonly used as the ambient metric. Therefore in our point cloud simulation (Section 5.2) and energy data analysis (Section 6.2) we have adopted the Euclidean distance as the ambient metric.

For our distributional data simulation (Section 5.1), we use the Wasserstein distance as the metric d . This choice is motivated by the fact that key Riemannian manifold concepts, such as the tangent space, exponential map, and logarithm map, can be naturally extended to Wasserstein space ([Ambrosio et al. 2008](#), [Panaretos & Zemel 2019](#)). An alternative choice for distributional data is the Fisher-Rao metric ([Dai 2022](#)), which, while not as directly connected to optimal transport theory as the Wasserstein metric ([Villani 2003](#)), has computational advantages. Specifically, it serves as the geodesic distance for the square root of probability densities,

$$d_{FR}(\xi_1, \xi_2) = \arccos \left(\int \sqrt{f_{\xi_1}(x) f_{\xi_2}(x)} dx \right),$$

where $\xi_1, \xi_2 \in \mathcal{W}_2(\mathbb{R}^p)$ with densities $f_{\xi_1}(x), f_{\xi_2}(x)$.

For the gait synchronization data analysis (Section 6.1), we employ the Bures-Wasserstein metric to measure distances between SPD matrices. This metric is equivalent to the Wasserstein metric for the space of non-degenerate Gaussian distributions ([Bhatia et al. 2019](#)). In the space of SPD matrices, feature preservation along geodesics is often desirable, as

the choice of metric determines the paths connecting data objects. The classical Frobenius distance, while commonly used, suffers from the swelling effect, which can distort statistical interpretations. This issue can be mitigated using the Cholesky distance (Dryden, Koloydenko & Zhou 2009, Lin 2019), which provides a more stable representation.

For the gait synchronization data analysis (Section 6.1), we compare our curvature test results using three different input metrics d : 1) the Bures-Wasserstein metric, 2) Frobenius metric, and 3) Cholesky metric. To infer the intrinsic curvature of the space of gait synchronization SPD matrices we compare the intrinsic Fréchet variance $\hat{V}_{I,F}$ and metric variance $\hat{V}_{I,M}$. The confidence regions $\mathcal{C}_{I,n}(1 - \alpha)$ in (16) for $(V_{I,M}, V_{I,F})^T$ are illustrated in Figure S.7 for the healthy and orthopedic disorder groups, with significance levels $\alpha = 0.01, 0.05, 0.1$. Specifically, the first row corresponds to the Bures-Wasserstein input metric, the second row to the Cholesky input metric, and the third row to the Frobenius input metric. For the healthy group, regardless of the choice of input distance, all confidence regions intersect with the set $\{(V_{I,M}, V_{I,F}) \mid V_{I,M} = V_{I,F}\}$, but with $\hat{V}_{I,F}$ consistently greater than $\hat{V}_{I,M}$, which may indicate a slight positive curvature. In contrast, for the orthopedic disorder group, the confidence regions are consistently contained in the set $\{(V_{I,M}, V_{I,F}) \mid V_{I,M} > V_{I,F}\}$ at level $\alpha = 0.01$, indicating the presence of negative curvature.

For the distributional simulation scenario in Section 5.1, we compare our curvature test results using two different input metrics d : 1) the 2-Wasserstein metric and 2) the Fisher-Rao metric.

In Figure S.8, we compare the intrinsic Fréchet variance $\hat{V}_{I,F}$ and the metric variance $\hat{V}_{I,M}$. The confidence regions $\mathcal{C}_{I,n}(1 - \alpha)$ in (16) for $(V_{I,M}, V_{I,F})^T$ are displayed. Regardless of whether the Wasserstein or Fisher-Rao metric is used, all confidence regions intersect with

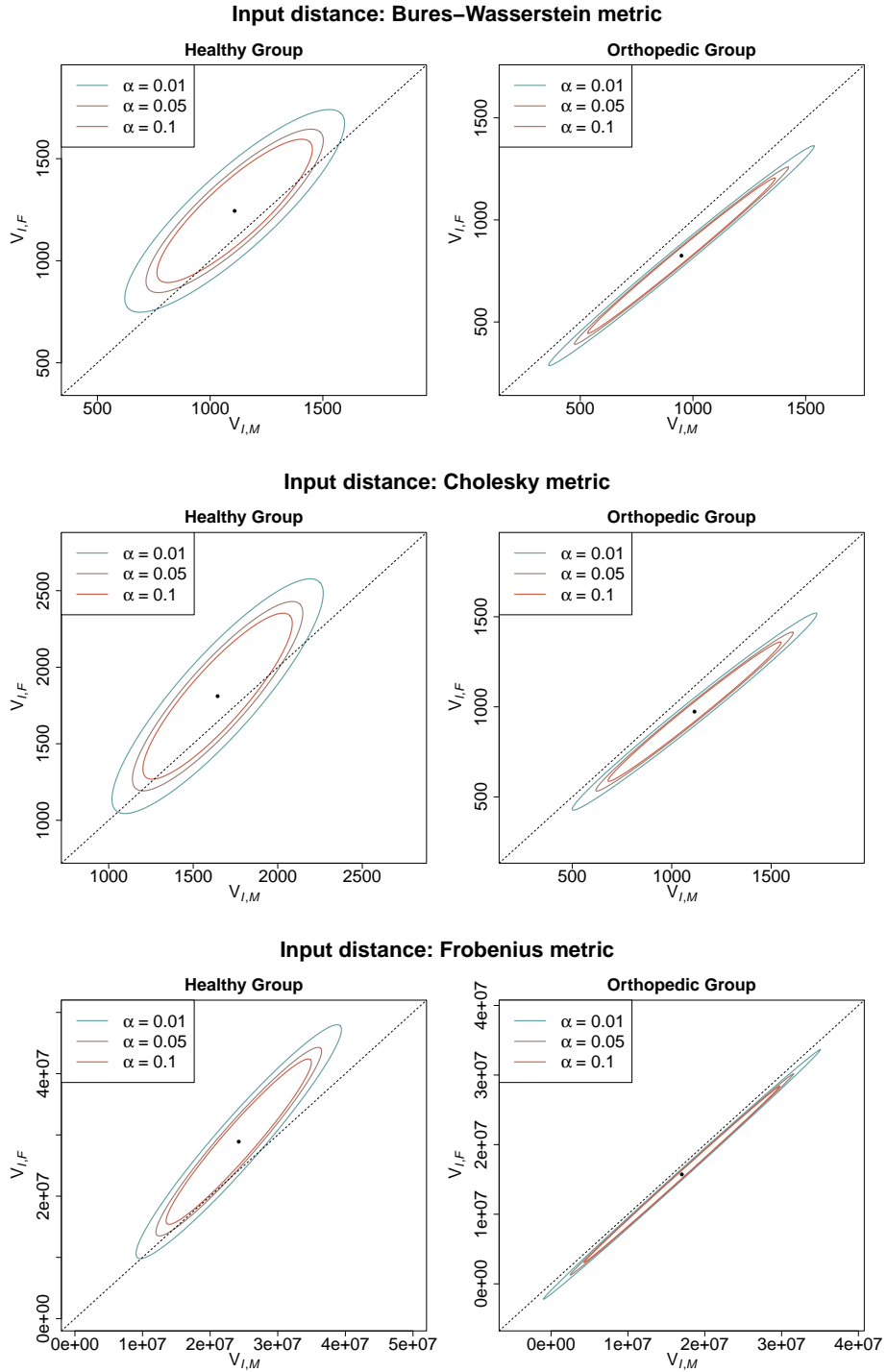


Figure S.7: Comparison of confidence regions $\mathcal{C}_{I,n}(1-\alpha)$ in (16) for $(V_{I,M}, V_{I,F})$ representing gait synchronization SPD matrices for healthy and orthopedic disorder groups, with $\alpha = 0.01, 0.05, 0.1$. The first row corresponds to the Bures–Wasserstein input metric, the second row to the Cholesky input metric, and the third row to the Frobenius input metric, all yielding consistent curvature test results.

Distributional Data Simulation

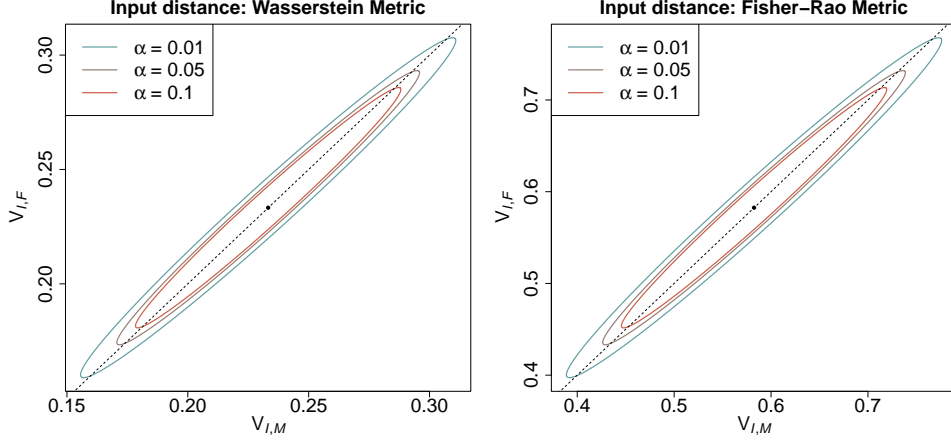


Figure S.8: The proposed intrinsic curvature test results using the confidence regions $\mathcal{C}_{I,n}(1 - \alpha)$ in (16) for $(V_{I,M}, V_{I,F})$ with $\alpha = 0.01, 0.05, 0.1$. The first column corresponds to the 2-Wasserstein input metric, and the second row to the Fisher-Rao metric, both indicating a consistent result of intrinsic flat curvature.

the set $\{(V_{I,M}, V_{I,F}) \mid V_{I,M} = V_{I,F}\}$ both indicating a consistent result that a flat intrinsic curvature is compatible with the data.

In conclusion, our experiment shows that at least for the scenario considered, the choice of input distance d does not significantly affect the results, indicating a degree of robustness. However, in general, the selection of an appropriate input distance requires further research, as briefly discussed in Section 7.

S.7 Relation between metric curvature and Alexandrov curvature

By definition, the metric curvature ρ is determined by the ratio of the *expectation* of $d^2(\mu_{\oplus}, X)$ and $\frac{1}{2}d^2(X, X')$,

$$\rho = \frac{V_F}{V_M} - 1 = \frac{2\mathbb{E}d^2(\mu_{\oplus}, X)}{\mathbb{E}d^2(X, X')} - 1,$$

where X' represents an i.i.d. copy of X . Thus, the actual value of ρ depends on the probability measure \mathcal{P} of the random objects X . As a consequence, for a fixed model space $(\mathcal{M}_\kappa, d_\kappa)$ with the curvature parameter κ , while the sign of κ determines the sign of ρ (as stated in Proposition 4), the actual value of ρ can vary depending on the probability measure \mathcal{P} .

In some special cases, we can establish a somewhat stronger relationship. We consider flat, positively curved, and negatively curved model spaces, i.e., \mathcal{M}_κ , for $\kappa = 0$, $\kappa > 0$, and $\kappa < 0$.

- For $\kappa = 0$, the model space is the Euclidean plane $\mathcal{M}_\kappa = \mathbb{R}^2$ with the Euclidean distance. Then irrespective of the probability measure \mathcal{P} of X , as long as it is positive, Proposition 4 implies that $\rho = \kappa = 0$.
- For $\kappa > 0$, the model space is the sphere

$$\mathcal{M}_\kappa = \mathbb{S}^2 = \{(x, y, z) \mid x^2 + y^2 + z^2 = 1\},$$

with the angular distance $d_\kappa(a, b) = \arccos(x_a x_b + y_a y_b + z_a z_b)/\sqrt{\kappa}$, where $a = (x_a, y_a, z_a)$ and $b = (x_b, y_b, z_b)$. Consider a positive probability measure \mathcal{P} that gener-

ates X . The metric curvature associated with \mathcal{M}_κ is

$$\rho_\kappa = \frac{2\mathbb{E}d_\kappa^2(\mu_\oplus, X)}{\mathbb{E}d_\kappa^2(X, X')} - 1,$$

where $X = (x_1, y_1, z_1)$, $X' = (x_2, y_2, z_2)$, and $\mu_\oplus = (x_\oplus, y_\oplus, z_\oplus)$. We assume that the unique Fréchet mean remains the same for all $\kappa > 0$, i.e.,

$$\mu_\oplus = \operatorname{argmin}_{\xi \in \mathcal{M}_\kappa} \mathbb{E}d_\kappa^2(\xi, X).$$

If we consider a measure \mathcal{P} that has a symmetric density with respect to the north pole $(0, 0, 1) \in \mathbb{S}^2$, the Fréchet mean can be fixed as $\mu_\oplus = (0, 0, 1)$ regardless of d_κ .

Then we obtain

$$\begin{aligned} \rho_\kappa &= \frac{2\mathbb{E}\{\arccos^2(x_1 x_\oplus + y_1 y_\oplus + z_1 z_\oplus)\}/\kappa}{\mathbb{E}\{\arccos^2(x_1 x_2 + y_1 y_2 + z_1 z_2)\}/\kappa} - 1 \\ &= \rho_1 = C_1 > 0, \end{aligned}$$

for all $\kappa > 0$ and some constant C_1 that does not depend on κ . The second equality follows from the cancellation of $1/\kappa$, and $C_1 > 0$ according to Proposition 4.

- For $\kappa < 0$, the model space is the hyperbolic space

$$\mathcal{M}_\kappa = \mathbb{H}^2 = \{(x, y, z) \mid x^2 + y^2 - z^2 = -1\},$$

with the hyperbolic distance $d_\kappa(a, b) = \operatorname{arccosh}(z_a z_b - x_a x_b - y_a y_b)/\sqrt{-\kappa}$ for $\kappa < 0$.

Similarly, under the assumption that the Fréchet mean does not depend on κ , for all $\kappa < 0$, we can obtain $\rho_\kappa = \rho_{-1} = C_2 < 0$, for some constant C_2 that does not depend

on κ .

For these special cases, the dependence of the metric curvature ρ is a monotone increasing step function of the Alexandrov curvature κ , as illustrated in Figure S.9.

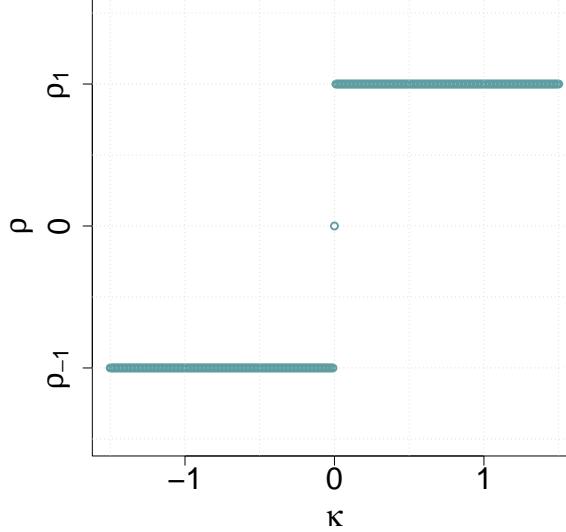


Figure S.9: Relationship between the metric curvature ρ and the Alexandrov curvature κ for the special case where the probability measure \mathcal{P} is fixed and the Fréchet mean is independent of κ .

If one desires a linear relationship, one may instead consider an alternative measure ρ' , defined as

$$\rho' = \frac{1}{V_M} - \frac{1}{V_F}.$$

By leveraging the relationship between Fréchet variance V_F and metric variance V_M in Theorem 2, Theorem 3, and Corollary 1 in Section 3.2, this alternative measure ρ' still satisfies Proposition 4, i.e., if (\mathcal{M}, d) has strictly negative curvature, then $\rho' < 0$, if (\mathcal{M}, d) has strictly positive curvature and condition (F1) holds, then $\rho' > 0$, and if (\mathcal{M}, d) is a flat space, then $\rho' = 0$. Again invoking the above assumptions that the positive probability measure \mathcal{P} is fixed and the unique Fréchet mean is independent of κ for $\kappa > 0$, one can derive the relationship of ρ' and κ in spaces \mathcal{M}_κ . Denoting the dependency of ρ' on κ by

ρ'_κ , it emerges that

$$\begin{aligned}
\rho'_\kappa &= \frac{2}{\mathbb{E}d_\kappa^2(X, X')} - \frac{1}{\mathbb{E}d_\kappa^2(\mu_\oplus, X)} \\
&= \kappa \left(\frac{2}{\mathbb{E}\{\arccos^2(x_1x_2 + y_1y_2 + z_1z_2)\}} - \frac{1}{\mathbb{E}\{\arccos^2(x_1x_2 + y_1y_2 + z_1z_2)\}} \right) \\
&= \kappa\rho'_1 = \kappa C_3 > 0,
\end{aligned}$$

for some constant C_3 . Similarly, it holds that $\rho'_{-\kappa} = (-\kappa)\rho'_{-1} = \kappa C_4 < 0$ for $\kappa < 0$ and some constant $C_4 = (-\rho'_{-1}) > 0$.

Figure S.10 illustrates the relationship between ρ' and the Alexandrov curvature κ under these additional assumptions. Furthermore, estimation of ρ' and the asymptotic normality of estimates is completely analogous to the corresponding results for ρ .

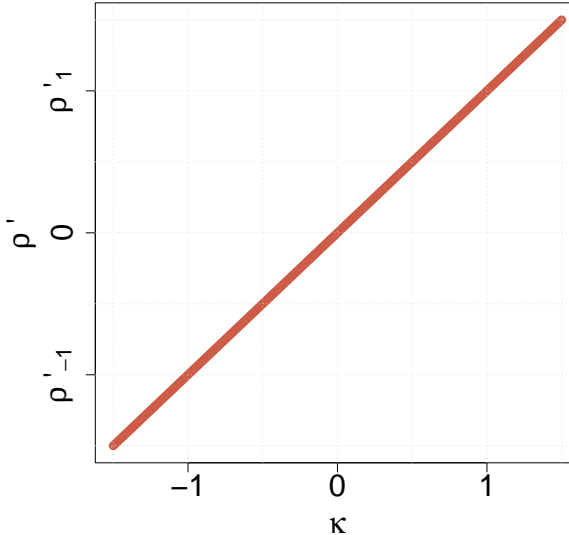


Figure S.10: Relationship between the alternative metric curvature ρ' and the Alexandrov curvature κ under the special case where the probability measure \mathcal{P} is fixed and the Fréchet mean is independent of κ , for $\kappa > 0$, $\kappa = 0$, and $\kappa < 0$.

References

Aamari, E., Berenfeld, C. & Levraud, C. (2023), ‘Optimal reach estimation and metric learning’, *The Annals of Statistics* **51**(3), 1086–1108.

Aaron, C. & Bodart, O. (2018), ‘Convergence rates for estimators of geodesic distances and Fréchet expectations’, *Journal of Applied Probability* **55**(4), 1001–1013.

Afsari, B. (2011), ‘Riemannian L^p center of mass: existence, uniqueness, and convexity’, *Proceedings of the American Mathematical Society* **139**(2), 655–673.

Aguech, M. & Carlier, G. (2011), ‘Barycenters in the Wasserstein space’, *SIAM Journal on Mathematical Analysis* **43**(2), 904–924.

Ahidar-Coutrix, A., Le Gouic, T. & Paris, Q. (2020), ‘Convergence rates for empirical barycenters in metric spaces: curvature, convexity and extendable geodesics’, *Probability Theory and Related Fields* **177**, 323–368.

Alberink, I. B. & Bentkus, V. (2001), ‘Berry-Esseen bounds for von Mises and U-statistics’, *Lithuanian Mathematical Journal* **41**(1), 1–16.

Aleksandrov, A. D. (1951), ‘A theorem on triangles in a metric space and some of its applications’, *Trudy Matematicheskogo Instituta imeni VA Steklova* **38**, 5–23.

Ambrosio, L., Gigli, N. & Savaré, G. (2008), *Gradient Flows: in Metric Spaces and in the Space of Probability Measures*, Springer Science & Business Media.

Arias-Castro, E., Javanmard, A. & Pelletier, B. (2020), ‘Perturbation bounds for procrustes, classical scaling, and trilateration, with applications to manifold learning’, *Journal of Machine Learning Research* **21**(15), 1–37.

Arsigny, V., Fillard, P., Pennec, X. & Ayache, N. (2007), ‘Geometric means in a novel vector space structure on symmetric positive-definite matrices’, *SIAM Journal on Matrix Analysis and Applications* **29**(1), 328–347.

Bacák, M. (2014), ‘Computing medians and means in Hadamard spaces’, *SIAM Journal on Optimization* **24**(3), 1542–1566.

Bachlin, M., Plotnik, M., Roggen, D., Maidan, I., Hausdorff, J. M., Giladi, N. & Troster, G. (2009), ‘Wearable assistant for parkinson’s disease patients with the freezing of gait symptom’, *IEEE Transactions on Information Technology in Biomedicine* **14**(2), 436–446.

Barrois, R., Oudre, L., Moreau, T., Truong, C., Vayatis, N., Buffat, S., Yelnik, A., de Waele, C., Gregory, T., Laporte, S. et al. (2015), ‘Quantify osteoarthritis gait at the doctor’s office: a simple pelvis accelerometer based method independent from footwear and aging’, *Computer Methods in Biomechanics and Biomedical Engineering* **18**(sup1), 1880–1881.

Belkin, M. & Niyogi, P. (2001), ‘Laplacian eigenmaps and spectral techniques for embedding and clustering’, *Advances in neural information processing systems* **14**.

Berk, R. H. (1966), ‘Limiting behavior of posterior distributions when the model is incorrect’, *The Annals of Mathematical Statistics* **37**(1), 51–58.

Bhatia, R. (2009), *Positive Definite Matrices*, Princeton University Press.

Bhatia, R., Jain, T. & Lim, Y. (2019), ‘On the Bures-Wasserstein distance between positive definite matrices’, *Expositiones Mathematicae* **37**(2), 165–191.

Billera, L. J., Holmes, S. P. & Vogtmann, K. (2001), ‘Geometry of the space of phylogenetic trees’, *Advances in Applied Mathematics* **27**(4), 733–767.

Boissonnat, J.-D. & Ghosh, A. (2014), ‘Manifold reconstruction using tangential delaunay complexes’, *Discrete & Computational Geometry* **51**(1), 221–267.

Bolstad, B. M., Irizarry, R., Åstrand, M. & Speed, T. (2003), ‘A comparison of normalization methods for high density oligonucleotide array data based on variance and bias’, *Bioinformatics* **19**, 185–193.

Bridson, M. R. & Haefliger, A. (2013), *Metric Spaces of Non-positive Curvature*, Vol. 319, Springer Science & Business Media.

Burago, D., Burago, Y. & Ivanov, S. (2001), *A Course in Metric Geometry*, American Mathematical Society.

Callaert, H. & Janssen, P. (1978), ‘The Berry-Esseen theorem for U-statistics’, *The Annals of Statistics* **6**(2), 417–421.

Chen, D. & Müller, H.-G. (2012), ‘Nonlinear manifold representations for functional data’, *The Annals of Statistics* **40**(1), 1–29.

Chen, Y., Lin, Z. & Müller, H.-G. (2023), ‘Wasserstein regression’, *Journal of the American Statistical Association* **118**(542), 869–882.

Chew, J., Steach, H., Viswanath, S., Wu, H.-T., Hirn, M., Needell, D., Vesely, M. D., Krishnaswamy, S. & Perlmutter, M. (2022), ‘The manifold scattering transform for high-dimensional point cloud data’, *Topological, Algebraic and Geometric Learning Workshops* **196**, 67–78.

Chewi, S., Maunu, T., Rigollet, P. & Stromme, A. J. (2020), Gradient descent algorithms for Bures-Wasserstein barycenters, in ‘Conference on Learning Theory’, PMLR, pp. 1276–1304.

Chu, L. & Dai, X. (2024), ‘Manifold energy two-sample test’, *Electronic Journal of Statistics* **18**(1), 145–166.

Cornea, E., Zhu, H., Kim, P., Ibrahim, J. G. & Initiative, A. D. N. (2017), ‘Regression models on Riemannian symmetric spaces’, *Journal of the Royal Statistical Society: Series B (Statistical Methodology)* **79**(2), 463–482.

Cuturi, M. (2013), ‘Sinkhorn distances: Lightspeed computation of optimal transport’, *Advances in neural information processing systems* **26**.

Dai, X. (2022), ‘Statistical inference on the Hilbert sphere with application to random densities’, *Electronic Journal of Statistics* **16**(1), 700–736.

Dharmadhikari, S., Fabian, V. & Jogdeo, K. (1968), ‘Bounds on the moments of martingales’, *The Annals of Mathematical Statistics* **39**(5), 1719–1723.

Dijkstra, E. W. (1959), ‘A note on two problems in connexion with graphs’, *Numerische Mathematik* **1**, 269–271.

Donadelli, M., Jüppner, M., Paradiso, A. & Schlag, C. (2021), ‘Computing macro-effects and welfare costs of temperature volatility: A structural approach’, *Computational Economics* **58**, 347–394.

Dryden, I. L., Bai, L., Brignell, C. J. & Shen, L. (2009), ‘Factored principal components analysis, with applications to face recognition’, *Statistics and Computing* **19**, 229–238.

Dryden, I. L., Koloydenko, A. & Zhou, D. (2009), ‘Non-Euclidean statistics for covariance matrices, with applications to diffusion tensor imaging’, *Annals of Applied Statistics* **3**(3), 1102–1123.

Dubey, P., Chen, Y. & Müller, H.-G. (2024), ‘Metric statistics: Exploration and inference for random objects with distance profiles’, *Annals of Statistics* **52**, 757–792.

Dubey, P. & Müller, H.-G. (2019), ‘Fréchet analysis of variance for random objects’, *Biometrika* **106**(4), 803–821.

Dubey, P. & Müller, H.-G. (2020), ‘Functional models for time-varying random objects’, *Journal of the Royal Statistical Society Series B: Statistical Methodology* **82**(2), 275–327.

Dubey, P. & Zheng, M. (2023), ‘Change point detection for random objects using distance profiles’, *arXiv preprint arXiv:2311.16025* .

Eltzner, B., Huckemann, S. & Mardia, K. V. (2018), ‘Torus principal component analysis with applications to RNA structure’, *The Annals of Applied Statistics* **12**(2), 1332–1359.

Feragen, A., Lauze, F. & Hauberg, S. (2015), ‘Geodesic exponential kernels: When curvature and linearity conflict’, *Proceedings of the IEEE Conference on Computer Vision and Pattern Recognition* pp. 3032–3042.

Fletcher, P. T., Lu, C., Pizer, S. M. & Joshi, S. (2004), ‘Principal geodesic analysis for the study of nonlinear statistics of shape’, *IEEE Transactions on Medical Imaging* **23**(8), 995–1005.

Fréchet, M. (1948), ‘Les éléments aléatoires de nature quelconque dans un espace distancié’, *Annales de l'institut Henri Poincaré* **10**(4), 215–310.

Friedrich, K. O. (1989), ‘A Berry-Esseen bound for functions of independent random variables’, *The Annals of Statistics* **17**(1), 170–183.

Han, A., Mishra, B., Jawanpuria, P. K. & Gao, J. (2021), ‘On Riemannian optimization over positive definite matrices with the Bures-Wasserstein geometry’, *Advances in Neural Information Processing Systems* **34**, 8940–8953.

Hoeffding, W. (1948), ‘A class of statistics with asymptotically normal distribution’, *The Annals of Mathematical Statistics* **19**(3), 293–325.

Hoeffding, W. (1961), The strong law of large numbers for u-statistics., Technical report, North Carolina State University. Dept. of Statistics.

Huckemann, S. & Eltzner, B. (2021), ‘Data analysis on nonstandard spaces’, *Wiley Interdisciplinary Reviews: Computational Statistics* **13**(3), e1526.

Hundrieser, S., Eltzner, B. & Huckemann, S. (2024), ‘Finite sample smeariness of Fréchet means with application to climate’, *Electronic Journal of Statistics* **18**(2), 3274–3309.

Jiang, F., Zhu, C. & Shao, X. (2024), ‘Two-sample and change-point inference for non-Euclidean valued time series’, *Electronic Journal of Statistics* **18**(1), 848–894.

Kantorovich, L. V. (2006), ‘On the translocation of masses’, *Journal of Mathematical Sciences* **133**(4), 1381–1382.

Kelley, J. L. (1959), ‘Measures on boolean algebras’, *Measures on Boolean algebras* **9**, 1165–1177.

Lang, S. (2012), *Differential and Riemannian manifolds*, Vol. 160, Springer Science & Business Media.

Le Gouic, T. & Loubes, J.-M. (2017), ‘Existence and consistency of Wasserstein barycenters’, *Probability Theory and Related Fields* **168**, 901–917.

Lee, A. J. (2019), *U-statistics: Theory and Practice*, Routledge.

Lee, Y., Kim, S., Choi, J. & Park, F. (2022), A statistical manifold framework for point cloud data, in ‘International Conference on Machine Learning’, PMLR, pp. 12378–12402.

Lin, Z. (2019), ‘Riemannian geometry of symmetric positive definite matrices via Cholesky decomposition’, *SIAM Journal on Matrix Analysis and Applications* **40**(4), 1353–1370.

Lin, Z. & Müller, H.-G. (2021), ‘Total variation regularized Fréchet regression for metric-space valued data’, *The Annals of Statistics* **49**(6), 3510–3533.

Marron, J. S. & Dryden, I. L. (2021), *Object Oriented Data Analysis*, Chapman and Hall/CRC.

McInnes, L., Healy, J. & Melville, J. (2018), ‘Umap: Uniform manifold approximation and projection for dimension reduction’, *arXiv preprint arXiv:1802.03426* .

Otto, F. (2001), ‘The geometry of dissipative evolution equations: the porous medium equation’, *Comm. Partial Differential Equations* **26**, 101–174.

Panaretos, V. M. & Zemel, Y. (2019), ‘Statistical aspects of Wasserstein distances’, *Annual Review of Statistics and its Application* **6**, 405–431.

Pennec, X. (2019), ‘Curvature effects on the empirical mean in Riemannian and affine manifolds: a non-asymptotic high concentration expansion in the small-sample regime’, *arXiv preprint arXiv:1906.07418* .

Petersen, A. & Müller, H.-G. (2019), ‘Fréchet regression for random objects with Euclidean predictors’, *The Annals of Statistics* **47**(2), 691–719.

Pigoli, D., Aston, J. A., Dryden, I. L. & Secchi, P. (2014), ‘Distances and inference for covariance operators’, *Biometrika* **101**(2), 409–422.

Scealy, J. & Welsh, A. (2014), ‘Colours and cocktails: Compositional data analysis’, *Australian & New Zealand Journal of Statistics* **56**(2), 145–169.

Serfling, R. J. (2009), *Approximation Theorems of Mathematical Statistics*, John Wiley & Sons.

Shorack, G. R. & Wellner, J. A. (2009), *Empirical Processes with Applications to Statistics*, Society for Industrial and Applied Mathematics.

Song, H. & Chen, H. (2022), ‘New graph-based multi-sample tests for high-dimensional and non-Euclidean data’, *arXiv preprint arXiv:2205.13787* .

Sturm, K.-T. (2003), ‘Probability measures on metric spaces of nonpositive curvature’, *Heat Kernels and Analysis on Manifolds, Graphs, and Metric Spaces (Paris, 2002)*. *Contemp. Math.*, 338. Amer. Math. Soc., Providence, RI **338**, 357–390.

Takatsu, A. (2011), ‘Wasserstein geometry of Gaussian measures’, *Osaka Journal of Mathematics* **48**(4), 1005–1026.

Tenenbaum, J. B., Silva, V. d. & Langford, J. C. (2000), ‘A global geometric framework for nonlinear dimensionality reduction’, *Science* **290**(5500), 2319–2323.

Truong, C., Barrois-Müller, R., Moreau, T., Provost, C., Vienne-Jumeau, A., Moreau, A., Vidal, P.-P., Vayatis, N., Buffat, S., Yelnik, A. et al. (2019), ‘A data set for the study of human locomotion with inertial measurements units’, *Image Processing On Line* **9**, 381–390.

van der Vaart, A. & Wellner, J. A. (2023), *Weak Convergence and Empirical Processes: With Applications to Statistics*, Springer Nature.

van Zwet, W. R. (1984), ‘A Berry-Esseen bound for symmetric statistics’, *Zeitschrift für Wahrscheinlichkeitstheorie und verwandte Gebiete* **66**, 425–440.

Villani, C. (2003), *Topics in Optimal Transportation*, American Mathematical Society.

Wang, J.-L., Chiou, J.-M. & Müller, H.-G. (2016), ‘Functional data analysis’, *Annual Review of Statistics and its application* **3**, 257–295.

Wang, X., Zhu, J., Pan, W., Zhu, J. & Zhang, H. (2024), ‘Nonparametric statistical inference via metric distribution function in metric spaces’, *Journal of the American Statistical Association* **119**(548), 2772–2784.

Zheng, Y. (2015), ‘Trajectory data mining: an overview’, *ACM Transactions on Intelligent Systems and Technology (TIST)* **6**(3), 1–41.

Zhu, C. & Müller, H.-G. (2024), ‘Spherical autoregressive models, with application to distributional and compositional time series’, *Journal of Econometrics* **239**(2), 105389.